Title
Characterization of in situ Deformation Texture in Superelastic Nitinol

Author
Xu, David

Publication Date
2012

Characterization of *in situ* Deformation Texture in Superelastic Nitinol

By

David Xu

A dissertation submitted in partial satisfaction of the

requirements for the degree of

Doctor of Philosophy

in

Engineering – Materials Science and Engineering

in the

Graduate Division

of the

University of California, Berkeley

Committee in charge:

Professor Robert O. Ritchie, Chair
Professor Ronald Gronsky
Professor Panayiotis Papadopoulos

Fall 2012

Abstract

Characterization of *in situ* Deformation Texture in Superelastic Nitinol

by

David Xu

Doctor of Philosophy in Materials Science and Engineering

University of California, Berkeley

Professor Robert Ritchie, Chair

This dissertation is motivated by the increasing usage of Nitinol in biomedical implant devices as well as the disturbing numbers of failures as reported in the literature. Given the recent awareness of the complex *in vivo* loading conditions experience by the devices, combined with the lack of reliable commercial finite element analysis program capable of lifetime prediction for such devices, it is imperative to understand the fundamental mechanism of the underlying phase transformation behind the superelastic mechanical properties of Nitinol. In this research, both macroscopic as well microscopic mechanical responses are examined for Nitinol. It is determined that normalization of the dissimilar mechanical behaviors under different modes of loading is possible through Coffin-Manson approaches. The influence of austenitic texture by *in situ* multi-mode fatigue loading is explored with micro-X-ray Diffraction. It appears that the phase transformation propagation is a competition between the grain boundary and the orientational effect of grains. Changing the modes of loading appear to favor different propagation mechanism with varying effects on the austenitic texture of Nitinol. The results determined through this research will be used to derive a better constitutive relation as well as better fatigue lifetime prediction. Both of which will be used by the biomedical communities to improve material performance and device lifetimes.

To the love of my life, my dearest wife,
Luling Sun. For without her support
throughout this endeavor, I would be lost
and helpless.

Table of Contents

List of Figures

List of Tables

ACKNOWLEDGMENT

This dissertation is made possible from the wondrous support and help from families and friends. From my parents who believed in me and offered comfort when needed, to my wife who is beyond patient and provided much needed warmth when it comes to the entire process, I would like to thank you for putting up with me for the past years. But especially to Professor Robert Ritchie, it is only because of you that I decided to go to graduate school and to have the honor of being your student. Your guidance, advice and mentorship guided me through the process and helped me developed academically and professionally. Thank you all very, very much.

I would also like to acknowledge Dr. Scott Robertson, for his helpful discussions, technical advices as well as proving material samples, and without him I would not have accomplished this much. Thank you also goes out to Dr. Hrishikesh Bale as well, for his help on running a successful beamline experiment through many sleepless nights. In addition, thank you to the beamline scientists Drs. Nobumichi Tamura and Martin Kunz, whom were instrumental in obtain useful results at the beamline.

I would also like thank Nitinol Devices and Component, Inc. which provided funding for me as a struggling undergraduate student, and opened my eyes to the world of Nitinol, and continued to fund parts of my doctoral program. I am also grateful for the fantastic people at NDC, like Drs. Scott Robertson and Alan Pelton, who provided much needed technical advice during times of need.

Finally, I would like to thank Cordis Inc., which provided funding for part of my doctoral program. I am in debt to Ramesh Marrey, who assisted with many technical problems and helped out with the FDA workshop.

I. Introduction

Nitinol is a near equiatomic alloy of Nickel and Titanium. It is a relatively new engineering material, having only been discovered in 1962 at Naval Ordnance Laboratory (disestablished in 1993) in White Oak, Maryland [1]. The two elemental symbols (Ni, Ti) along with the place of discovery gives Nitinol its name (NiTiNOL = Nickel Titanium Naval Ordnance Laboratory). The co-discoverers William J. Buehler [2] and Frederick Wang [3] were quick to recognize the special properties possessed by Nitinol, namely its shape-memory effect. However difficulties that involved melting, processing and machining delayed mass commercialization of devices utilizing the alloy until after the 1990s (30 years after its discovery) [4]. It would also be pertinent to note that while Nitinol is one of most well-known shape memory alloy, it is most certainly not the first to be discovered. The first known mention of shape memory effect is found in 1932 in gold-cadmium (Au-Cd) alloys by Arne Olander [5]. In 1950s, shape memory copper-zinc (Cu-Zn) alloys were also discovered [6]. In recent years, numerous other alloys are known to have shape memory properties in various operational environments, including numerous three-phase systems based on nickel and titanium. It is the goal of Materials Science & Engineering to understand as well as create and optimize the behavior of shape memory alloys to create better and novel devices. Thus the following experiments are designed in attempt to gain better understanding of mechanical behaviors of Nitinol with the hopes of devising methods for improving future Nitinol devices.

From the numerous choices of shape memory alloys, Nitinol stands out as the material of choice for biological implants. Specialized devices such as stents that prop open blood-vessels and lung passageways as well as novel devices like cholesterol-filters are saving and improving lives for millions of patients every year [7]. One of the beneficial characteristics of Nitinol is its very high biocompatibility [8-10]. Its performance is very similar to that of stainless steel (the alternative material of choice for biological implants). It also has extremely good imaging opacity under magnetic resonance as well as X-ray radiation [11, 12]. This allows for easy tracking of the implanted materials without invasive biopsy procedures. Perhaps the most important feature is mechanical behavior of Nitinol can be tuned into superelasticity instead of shape memory effect (described in Section I.ii.2). Superelasticity offers the ability for the alloy to completely recover extremely large applied deformations upon removal of the load. This superelastic behavior is exploited in nearly all of the biological implantation devices and a key property in engineering Nitinol alloys [7].

Beyond biomedical implant devices, Nitinol alloys have been utilized in various diverse applications such as bra underwires, eyeglass frames, mobile cellular phone antennas, pipe couplings, earthquake dampeners, orthodontic wires, micro-actuators, as well as potential explosives-protection armor materials for the military [11, 13-15]. However the recent trends of and the biggest market for Nitinol is still in biomedical implant devices [11, 13, 16].

I.i. Microstructural and thermodynamic aspect of Nitinol

In Figure I.1, the thermodynamic equilibrium phase diagram of titanium and nickel binary system is shown. Since both nickel and titanium are 3d transition metals, it means NiTi alloys are actually intermetallic. A typical biomedical grade Nitinol alloy is around $50.8\ at\%$ nickel and balanced titanium (also known as SE508, see Chapter II), and this is the material of choice for the experiments described in this text. In Figure I.1, the abscissa varies from pure titanium (left) to pure nickel (right), and ordinate varies from $600°C$ to $1800°C$. All of the thermodynamic stable phases as well as the respective two-phase regions are shown. A red line is drawn at constant composition of $50.8\ at\%$ showing the phases encountered upon cooling the SE508 alloy from its molten state. Note that at this composition, the alloy is actually anti-eutectic with melting-point maximum as well as solidification of single phase instead of two-phases found in eutectic systems. This has important implications such that if the original alloy is slightly more titanium-rich then the solidification process will result in a significantly more titanium-rich zone ahead of solidification front. The titanium-rich zone will eventually result in precipitation of eutectic βTi and Ti_2Ni phases and upon further cooling, followed by partial eutectic decomposition of near pure Ti and Ti_2Ni phases. The presence of titanium-rich precipitates significantly decreases shape memory alloy performances of the alloy and is generally avoided in processing of the material [17]. However, if the alloy is slightly more nickel-rich, the solidification process will result in eutectic precipitation of $NiTi$ and as well as $TiNi_3$ phases, which generally do not significantly degrade shape memory effect performances [17]. As such, the typical biomedical grade Nitinol composition is slightly more nickel-rich to optimize superelastic characteristics (hence the $50.8\ at\%$ nickel composition) [18].

Upon cooling from liquid phase, the first solid $TiNi$ phase to form actually has very wide solubility limit, however it very quickly narrows down to a line phase (with no solubility) at below $620°C$. As mentioned above, a slightly more nickel-rich composition will ensure precipitation of $TiNi_3$ phase in equilibrium. However due to kinetics, metastable phases such as Ti_3Ni_4 and Ti_2Ni_3 may form depending upon cooling rates [7]. These phases are very important in controlling several aspects of shape memory as well as superelasticity effects. Most thermal treatments target the formation of such precipitates to control the desirable qualities of the alloy [7].

The equilibrium NiTi phase near room temperature has the $B2$ structure [7]. This structure is two interlocking simple cubic lattice composed of nickel and titanium atoms (also referred to as the $CsCl$ structure). The space group of the equilibrium phase is $Pm\overline{3}m$, which has very high symmetry (cubic). While the $B2$ phase (usually called austenite phase) is thermodynamically stable, can be made unstable with respect to applied external work depending on the temperature. Once rendered unstable, the $B2$ phase will begin a phase transformation into a different meta-stable phase to accommodate the applied work. In shape memory effect, the addition of thermal heat is the source of work; while in superelasticity the external applied mechanical deformation is the work. There are also other ways to apply work, such as electrical (through Joule heating) or magnetic field (via magnetostriction), these alternative modes are almost never used in engineering devices but are currently in active research [19]. It is beyond the scope of this works to go into all of these modes except for the one predominantly used in biomedical device, where the source of applied work is mechanical deformation, also known as superelastic effects.

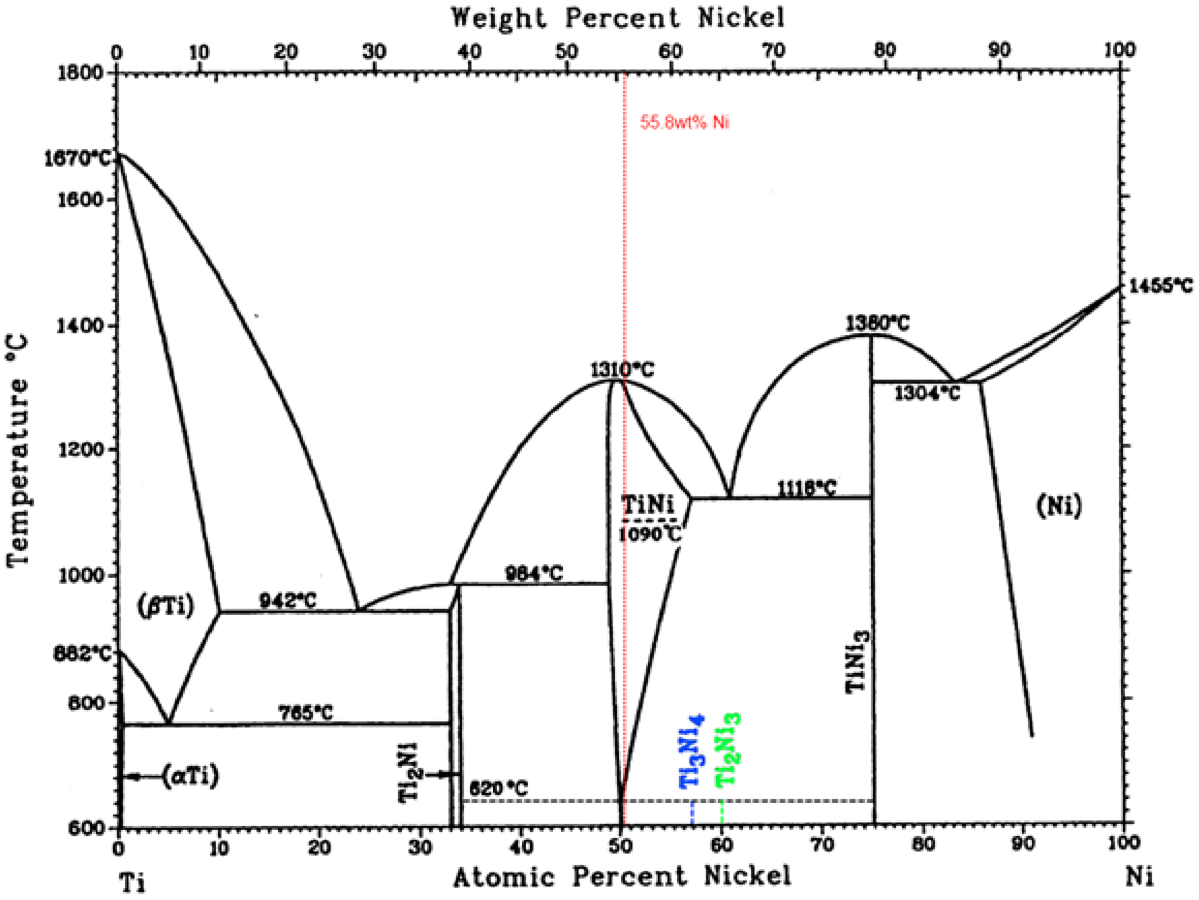

Figure I.1: Thermodynamic Equilibrium Phase diagram of titanium and nickel binary system [17]. Red line denotes the typical SE508 biomedical grade Nitinol alloy. Important meta-stable precipitates of NiTi phase are labeled for illustration purpose.

The newly formed meta-stable phase after transformation is typically termed martensite and has the structure of $B19'$ [20]. This structure is very complex and has much lowered symmetry than $B2$ parent phase. The space group is $P2/m$ and is based off of monoclinic lattice. The phase transformation itself is rather interesting as it is athermal and diffusionless, which means there is no breaking and reformation of bonds or any diffusion of atoms. The phase change itself occurs via coordinated displacement of atomic planes (with associated lattice invariant shear and Bain strain). Due to the athermal nature, the phase transformation is considered to be second-order and occurs very rapidly [7].

The martensitic phase transformation has very high temperature dependence (see Figure I.3). At above M_s (Martensite start temperature), martensite is thermodynamically unstable and will not exist. However if the alloy is acted upon by mechanical deformation, the stable austenite phase will then become unstable, and transformation into martensite will occur. This process is termed stress-induced martensite (SIM). M_f (Martensite finish temperature) is below M_s which signifies the beginning of complete thermodynamic stability of martensite phase. At such point austenite phase is completely unstable and will readily transform into martensite given any small perturbation. When the temperature is brought back above A_s (Austenite start temperature), the existing martensitic phases will begin to reverse transform back into austenite phase. This is because austenite is now thermodynamically stable instead. This process of temperature-induced phase change is the basis of shape memory effect. Upon further heating, at above A_f (Austenite finish temperature), the alloy will be completely austenitic and will require application of non-heat work to trigger the phase transformation [7].

Another key temperature to consider is M_d (Martensite deformation temperature) where the energetics of martensite transformation is so unfavorable that austenite is completely stable with respect to all applied mechanical deformation [7]. At such temperature, the martensite phase is completely thermodynamically unstable and will rapidly reverse transform back into austenite, resulting in the presence of the austenite phase in the alloy. In biomedical devices, since superelastic behavior is desired [7], this imposes a requirement of the operating environment to be kept below M_d but above A_f to ensure full austenite phase stability but still allow for possibility of phase transformation via SIM (see Section I.ii.2 and Chapter II).

However, recall the presence of Ti_3Ni_4 phases in the phase diagram from earlier (Figure I.1), its presence can trigger another alternative "martensitic-like" transformation. It has since been termed "R-phase" for its rhombohedral symmetry [21-23]. This alternative transformation path typically interrupts the direct austenite-to-martensite transformation as an intermediary phase (such as austenite-R-martensite). This transformation results in a small recoverable strain and is typically undesired in biomedical implant devices [24]. Recent advancements in heat treatments and processing have resulted in the ability to produce alloy that have a suppressed R-phase [25]. The materials used in the experiments described in this text will take full advantage of R-phase suppression treatments to reduce or completely eliminate R-phase interference. However it should be recognized that R-phase may still be present. But given the relative low strain ($< 0.2\%$) induced by transformation of R-phase [23], and that most of the experiments in this text will be operating at strains at nearly an order magnitude higher, its effects can be ignored. Thus any outstanding R-phase will be considered martensitic for analytic purposes.

Similar to the phase transformation in steel, the martensitic transformation in Nitinol is also associated with volume change. However, unlike in steel, this volume change is slightly negative, which results in "negative dilation." [26] The value varies from -0.33% to -0.54% as reported in literature [26-28]. The implications of negative dilation is not completely understood currently, however it has been theorized that it has a negative impact on the fracture and fatigue resistance of Nitinol [26, 27]. Other phase transforming materials, such as cubic zirconia with its positive dilation will locally reduce stress via shielding effect of compressive strain from volume expansion (dilation) [29]. It is possible that Nitinol will experience a raised local stress via positive expansion strain induced by the volumetric contraction of transformation [25, 26]. However, the volume change is relatively small and the net effect on stress increase is not currently well understood. The characterization techniques used in this text are less than adequate to determine the role of negative dilation, and thus its effects will not be addressed in this text.

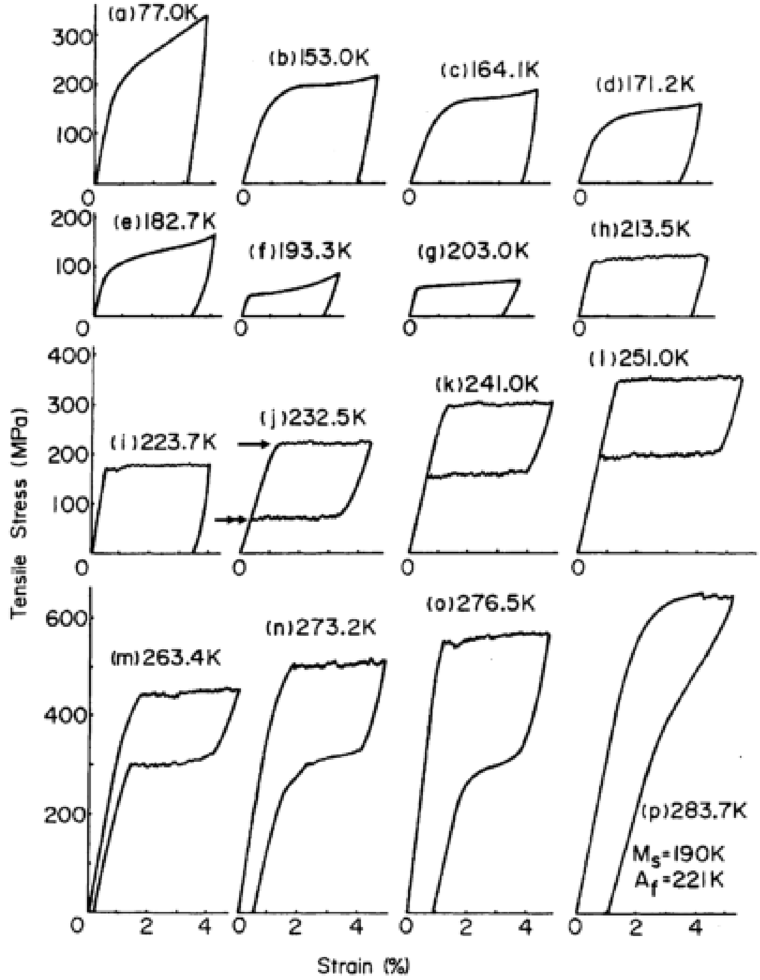

Figure I.2: Uniaxial stress-strain curve for Nitinol at various temperatures [17]. Note at below $223.7K$, the material behaves almost conventionally (shape memory), whereas above $223.7K$ and below $276.5K$, the material can recover very large strains (superelasticity). Thus the $A_f \approx 223.7K$ and $M_d \approx 276.5K$.

I.ii. Mechanical Behavior of Nitinol

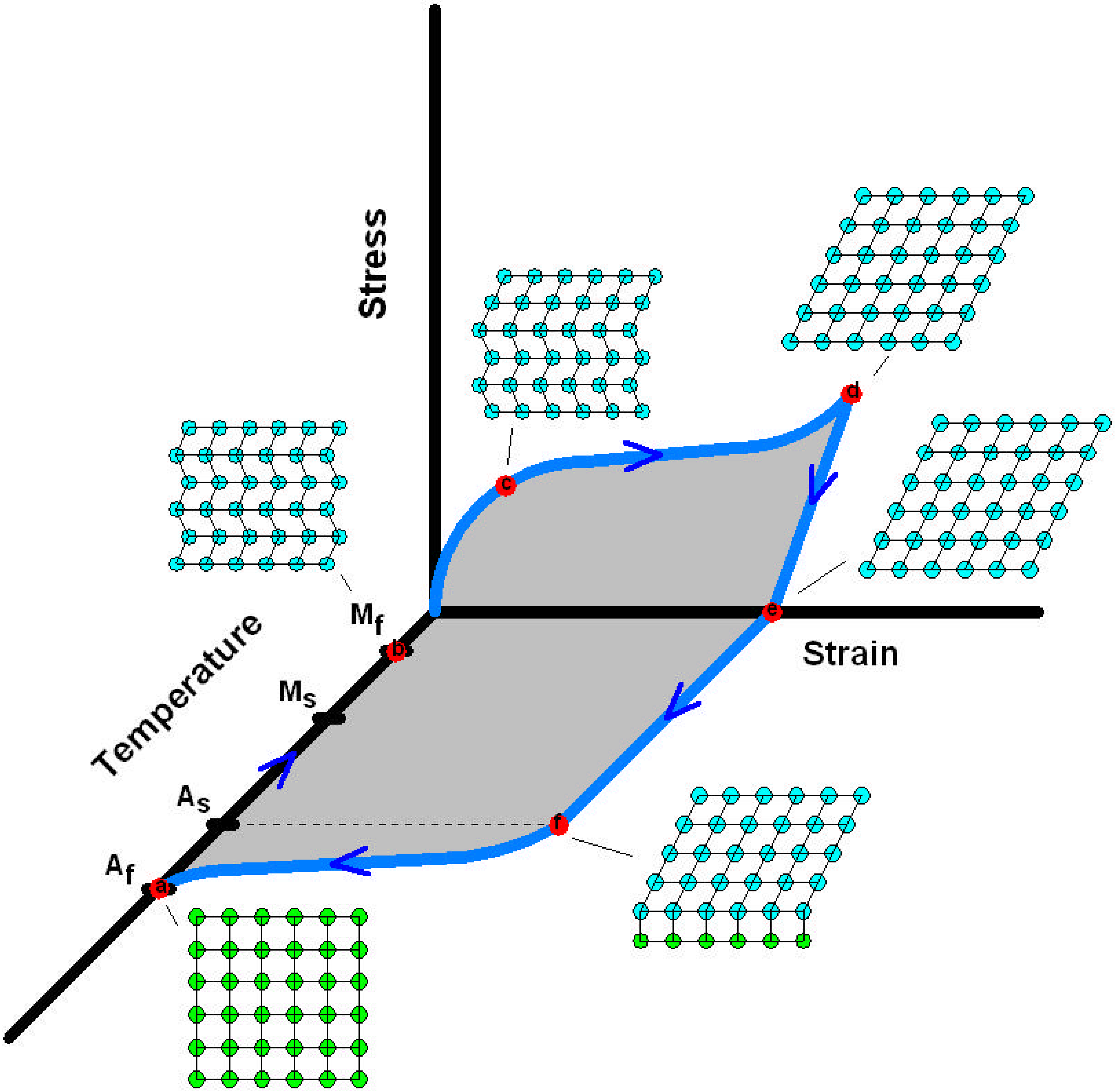

Figure I.3: Schematics showing the role stress, strain and temperature in shape memory effect. (a) Material is at A_f, which means it is fully austenitic. (b) Lowering to M_f at zero stress causes a phase transformation to twinned martensite. (c) Initial elastic loading of martensite phase. (d) Larger deformation causes detwinning of the martensite twins, which causes permanent deformation. (e) Elastic unloading of the now detwinned martensite phase, note the residual strain. (f) Heating back above A_s causes reverse transformation from martensite to austenite phase.[30]

Nitinol, like most other Shape Memory Alloys (SMA), exhibits drastically different mechanical behaviors at different temperature domains. The main difference lies within the identity of stabilized phase at the temperature range of testing. In Figure I.2, the same alloy is tested at increasing temperatures and the resulting stress-strain curves are shown. Note that below $232.5K$, the material behaves conventionally, and the material is in the shape memory effect regime. Whereas at above $232.5K$ (but below $276.5K$), the material exhibits completely different mechanical behavior, where unloading results in near full recovery of very large strains. This is the superelastic mode, and is the main deformation characteristics of biomedical implant devices.

I.ii.1. Shape Memory Effects

At below M_f the stabilized phase is martensite. Upon mechanical deformation, the martensite phase does not reverse transform into austenite. At such point the material behaves conventionally, the martensite would deform elastically followed by plasticity (see Figure I.2 below $232.5K$ stress-strain curves). It should be noted that plastic deformation mechanism in shape memory effect is actually the detwinning of martensite twins, which is very different from dislocation induced plasticity in traditional metals (Figure I.3) [7]. The detwinning process, unlike plasticity in conventional materials, can be reversed and is not permanent. When unloaded, the elastic strain relaxes and residual plastic strain appears to persist. The “permanent” deformation can be recovered through application of heat. This occurs when temperatures is increased ($T \geq A_f$) such that the stabilized phase is austenite and the detwinned martensite phase will begin a reverse transformation back into austenite phase. Because the permanent deformation comes about mostly through the twinning and detwinning process, the grain and dislocation structure are mostly preserved and therefore will be recovered through the reverse transformation [7]. The definition of the shape memory effect is that the plastic strain will recover after heating, resulting in a completely same shape as before. In other words, the alloy has effectively remembered its shape. See Figure I.3 for a complete cycle of deformation of shape memory alloy at low temperature followed by high temperature recovery.

There have been many interesting engineering uses of the shape memory effects. Couplings made from Nitinol would be used to join two pipes in cryogenic temperature (below M_f) [7, 31]. Upon application of heat, the austenite phase recovers and “remembers” its originally slightly smaller diameter shape and couple will shrink. This would create a very high interference fit resulting in excellent coupling of two pipes. There are other miscellaneous uses of shape memory effect; however it is not presently widely used in biomedical implant devices, and will not be the focus of this text.

I.ii.2. Superelasticity

Superelastic behavior occurs at temperature range between A_f and M_d. In this regime, austenite phase is stable and will deform readily. However, because the temperature range is below M_d, martensite transformation is favored over austenitic plastic deformation [7]. As such, upon reaching the limits of austenitic elasticity (typically $1 \sim 1.2\%$, see Chapter V), martensitic transformation will occur. This results in a flat plateau where the loading is constant but the material deforms continuously via SIM process. The end of the plateau marks the fully transformed martensitic Nitinol, and then the loading of fully martensitic Nitinol takes over. In Figure I.4, the loading portion is marked in red. After the material is fully martensitic, it behaves conventionally again, where further loading will result in elastic and plastic deformation of martensite phase. This is always avoided in biomedical implant devices because plastic deformation of martensite phase can actually induce permanent unrecoverable strain and damages in the sample.

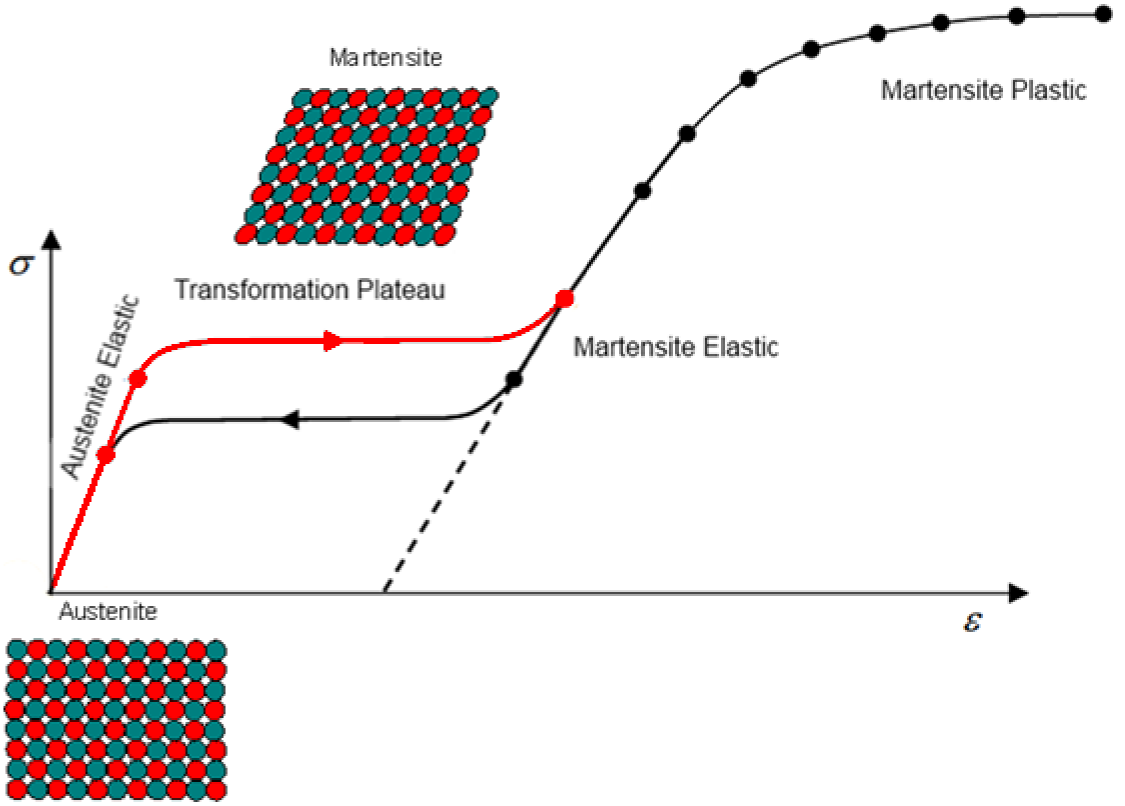

Figure I.4: Uniaxial deformation of superelastic Nitinol. Temperature must be above A_f but below M_d. Upon loading, the austenite parent phase will be elastically deformed but soon becomes unstable. It will then transform into martensite via SIM process. During this process, the material is still deforming but at a constant load. The process ends when the material becomes fully martensitic, this region of the stress-strain curve is called the "transformation plateau" (red line). Further loading will result in elastic and plastic deformation of the martensite phase. This is generally avoided. Unloading prior to permanent deformation of martensite phase will result in reverse transformation back to austenite phase and complete recovery of strain.

Because of the SIM and transformation plateau, the recoverable strain is tremendous in Nitinol with figures as high as 12% are reported [11, 12]. Such high reversibility in deformation as well as relatively constant stress is exploited by many biomedical implant devices. Large deformations which traditionally would have required much more conservative designs can be easily accommodated by Nitinol devices without too much special considerations [7]. Devices such as stents and implants typically use superelastic Nitinol with great success. Furthermore the nonlinear elastic nature of the superelastic Nitinol is similar to actual biological tissues such as bones, which results in a better biomechanical compatibility fit [7].

I.iii. Objectives and motivations

Nitinol has been the focus of active researches since its inception from NOL, in various aspects such as its unique mechanical deformation behaviors, fatigue properties, fracture toughness as well as the fundamentals of transformation itself [7, 30]. Given how ubiquitous Nitinol biomedical implant devices have become in the recent years, there is an urgent need to completely understand the fundamental constitutive laws for Nitinol. However presently, the typical constitutive law for Nitinol in commercial Finite Element Analysis (FEA) program assumes that the uniaxial tensile behavior holds true for multiaxial and multimode loading conditions [24]. Even with such conservative FEA as well as the brilliant mechanical performance of superelastic Nitinol, there are concerns with the long-term reliability of biological Nitinol devices [32-42], concerns that are so pressing that the FDA has hosted a workshop calling for the development of methods for predicting the *in vivo* lifetimes of implanted medical devices [43]. One of the major problems in predicting the life of Nitinol devices is the uncertainty involved in numerically computing the *in vivo* stresses [44-46]. The problem arises from the nature and magnitude of the complex mixed-mode loading that such devices see in biological environments. To this end it is imperative to understand the nature of superelastic deformation in Nitinol under stress-states other than simple uniaxial tension or compression [47]. Beyond the necessity to understand the monotonic mix-mode loading behaviors of superelastic Nitinol, there are pressing need to understand the multimode cyclic behavior of the material as well [24].

It is through the understanding of multiaxial monotonic behaviors that the constitutive law for mechanical behaviors of superelastic Nitinol could be derived. This knowledge will result in ability to better simulate and design biomedical implant devices. Understanding of the cyclic or fatigue behavior of the material requires the fundamental understanding of how the phase transformation and its recoverability degrade over time. The loss of phase transformation related mechanical properties has been termed functional fatigue and is one of main reasons for the relatively short lifespan of the Nitinol biomedical implant devices [7, 32-42]. By the studying of fatigue behaviors of the multiaxial loading, better understanding of micromechanics of the phase transformation will lead to better processing and controls of the devices that will hopefully improve lifetime for the devices as well as the patients that receive them.

The reminder of this text will be organized as follows. Chapter II reviews the materials used for each of the following experiments as well as experimental procedures utilized to achieve the research goals. Chapter III is devoted to understanding the fatigue of superelastic Nitinol tubes with approaches from classical mechanics such as S/N and Goodman diagrams. Chapter IV begins the section of the text on characterization of superelastic Nitinol under various loading configurations. Chapter IV features monotonic uniaxial tensile loading of dogbone samples with detailed studies of orientation effect as well as geometry of martensitic growth. Chapter V details a possible alternative deformation path in superelastic Nitinol, where plastic deformation austenite may run concurrent with SIM. Chapter VI discusses a novel approach to achieve planar shear for *in situ* loading and characterization of superelastic Nitinol cruciform samples. Chapter VII is about the fatigue of uniaxial tensile dogbone, and wires, as well as fatigue shear loading of the cruciform samples from Chapter VI. Finally some concluding remarks are seen in Chapter VIII. References used throughout the text will be in the reference section. There will be several Appendices. Appendix A is about the normalization shear and tensile strain. Appendix B is about the conversion between normalized miller indices to inverse pole figure projection. Appendix C describes the modified Taylor factor for superelastic Nitinol. Appendix D describes the Orientation Density Function. Appendix E shows the colorcoding used by the spatial mapping of the characterization results as well as MATLAB code used for the computation of the colors.

II. Experimental setup and material considerations

Nitinol materials were selected to be as close as possible to the actual stock for biomedical implant devices. Care is taken during the experiment to ensure the difference between experiment temperature and austenite finish temperature is similar to *in vivo* devices (typically $9°C$). This ensures the performance of experimental specimen will closely mimic the real performance of devices.

II.i. Torsional fatigue

Nitinol tubing samples, with a composition of Ti, $50.8\ at\%\ Ni$ ($Ni_{50.8}Ti_{49.2}$), identical to that used to manufacture endovascular stents (SE508[1]), were received from Nitinol Devices & Components, Inc. (Fremont, CA). The Nitinol tubing had an outer diameter of $3.18\ mm$ and an inner diameter of $2.52\ mm$. Samples were cut to a length of $70\ mm$, with a gauge section precision machined to a reduced outer diameter of $3.0\ mm$, and then honed using abrasive flow machining to polish the outer surface of the tubing samples and remove defects caused by drawing and machining.

Samples were then heat treated to obtain an austenite finish temperature, A_{f}, consistent with that of commercial stents; specifically, an annealing time and temperature were used to obtain a final A_f of $16°C$. The samples were tested in fatigue (in the superelastic austenitic condition) in room-temperature air, resulting in a $\Delta T = T - A_f$ of $9°C$, representing a difference, between the testing or service temperature, T, and A_f equivalent to that with the *in vivo* operation of commercial stents [11].

Prior to testing, the samples were further polished with an $HF - HNO_3 - H_2O$ etch to remove remaining oxide on both the inner and outer surfaces of the tubing. Lastly, a chemical polishing solution was introduced to the inner diameter of the tubing to ensure a smooth inner surface finish as well.

Additionally, to provide a comparison to the torsional fatigue results, very high mean strain ($R_\varepsilon \to 0.9$) tension-tension data were collected on “strut” specimens, which are test devices laser machined and processed from Nitinol SE508 tubing, with an outer diameter of $1.07\ mm$ and a wall thickness of $0.15\ mm$. These samples had an A_f temperature of $\sim 22°C$ but were tested at $37°C$, *i.e.*, with a ΔT of $15°C$, comparable with that of the torsion tests. Fifteen test specimens were tested, with gauge dimensions of $6\ mm$ long, $0.30\ mm$ wide and $0.15\ mm$ thick.

All single cycle and torsional fatigue tests were performed using a Bose ElectroForce 3200 desktop mechanical testing system (Bose, Eden Prairie, MN) with torsional and axial test-

---

[1] http://www.Nitinol.com/Nitinol-university/material-properties/

ing capabilities. Samples were cycled in room temperature air in displacement-control under various torsional loading conditions using custom-designed collet grips, with collets that had a tungsten carbide coating on the inner diameter to prevent specimen slippage during torsional cyclic loading.

Fully reversed single-cycle torsional loading data were obtained at various strain levels to determine the loading and unloading hysteresis curves for the superelastic Nitinol tubing material used for the fatigue testing. With respect to the fatigue, fully-reversed torsional fatigue samples were tested at a cyclic frequency of 5 Hz at equivalent strain amplitudes ranging from 1 to 4%, *i.e.*, at $R_\varepsilon = -1$. Samples were tested either (i) to outright failure when the sample fully fractured into multiple pieces, (ii) when a crack formed that was sufficient to decrease the torque by $0.05\ Nm$, or (iii) to a maximum of 10^7 cycles (run-outs). In addition to determining the torsional strain-life curve at $R_\varepsilon = -1$ with zero mean strain, the corresponding curve with a small positive mean strain, *i.e.*, at $R_\varepsilon = 0.2$, was also obtained with applied equivalent mean strains and strain amplitudes ranging from 0.5 to 2% and 0.25 to 1.3%, respectively. Additional tests were also performed on a more limited basis at R_ε values of 0 and 0.6.

High R_ε tension-tension specimens were cycled out to fracture or to a maximum of 10^6 cycles and the results indicate that the data are consistent with existing Nitinol fatigue data. Fifteen specimens were fatigue tested at 9% mean strain, with alternating strain of between 0.05 and 0.6%. Uniaxial tensile tests of the struts provided relationships between displacement (mm) and strain (%). These tests were conducted in a water bath at 37ºC, *i.e.*, with a ΔT of $15°C$, on a Bose ElectroForce 3330 mechanical testing system.

II.ii. Texture analysis of *in situ* tensile loading

Superelastic, nickel-rich Nitinol tubing ($Ni_{50.8}Ti_{49.2}$), comparable to that used in the production of medical devices, was laser machined longitudinally and shape-set into an unrolled configuration. Micro-dogbone-shaped tensile specimens, with the gauge section of $800 \times 200 \times 200\ \mu m$, were then laser machined at three different orientations to the Nitinol tube drawing axis: 0°, (longitudinal), 45° (transverse), and 90° (circumferential) Figure II.1. The dimensions of the gauge section of these samples were specifically designed to be comparable to struts from commercially available Nitinol stents. The dogbone specimens were heat-treated at $500°C$ for $10\ minutes$ in accordance with standard procedures for the processing of Nitinol medical devices [48], though an additional heat treatment of $700°C$ for $5\ minutes$ was required to obtain a nominal austenite grain size of about $10\sim 20\ \mu m$. These thermal treatments resulted in an austenite finish temperature of $15°C$. The larger grain size was necessary to permit the $\sim 1\ \mu m$ X-ray spot size to resolve the grain-by-grain transformation. Apart from this, the tube-based product form and subsequent processing steps were chosen to closely mirror that of stent manufacturing and give the same initial crystallographic texture.

Global stress-strain curves were obtained from tensile dogbone specimens, machined in the three different orientations, using a $2.3\ kg_f$ maximum load capacity displacement-controlled rig. The measurements were performed at room temperature and the samples were deformed at the displacement rate of $0.1\ \mu m/sec$. The direction of loading was reversed after a slow rising stress-plateau stress began to increase steeply (traditionally considered the sign of complete transformation to martensite). The measurement was completed when the load returned to zero. Measurements repeated for several specimens of the same orientation demonstrated consistent sample-to-sample stress-strain curves.

The specimens were subjected to progressively larger uniaxial deformation in the rig described above in an *in situ* experiment, whereby white-beam Laue diffraction patterns were obtained at each levels of deformation. A $\sim 1\mu m$ diameter X-ray beam was used to scan the entire gauge section of the samples $(800 \times\ 200\ \mu m)$ using a $6\sim10\ \mu m$ step size, yielding between $4800 \sim 6400$ diffraction patterns per specimen per strain condition. White-beam Laue diffraction [49] yielded the full three-dimensional deviatoric strain tensor as well as the local orientation of the crystal lattice (grain orientation). Martensite nanocrystalline laths are too small for the micrometer-sized white beam to probe [50]; consequently, the absence of a Laue diffraction pattern indicated the presence of martensite. The fraction of the gauge length that transformed was determined by counting the number of martensite pixels in a phase map and dividing it by the total number of pixels in the gauge length. Simultaneous uniaxial force-displacements were also obtained.

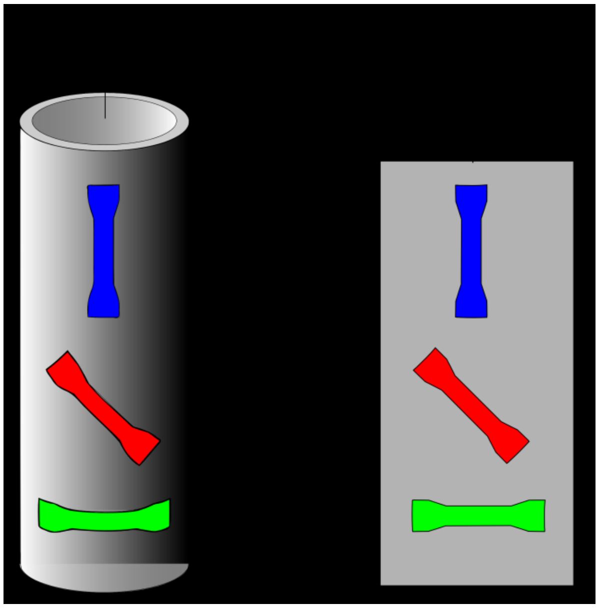

Figure II.1: Sample geometry showing the varying orientation of the tensile "dogbone" test specimens with respect to the drawing direction of the Nitinol tube.

II.iii. Texture analysis of *in situ* shearing loading

Nitinol ($50.8\ at\%\ Ni$, balanced Ti) from a cross-rolled sheet was received from Nitinol Devices & Components, Inc. (NDC, Fremont, CA). The sheet is nominally $0.3\ mm$ thick. The longer direction of the sheet is designated as RD (Rolling Direction), shorter direction, TD (Transverse Direction), and finally through thickness as ND (Normal Direction).

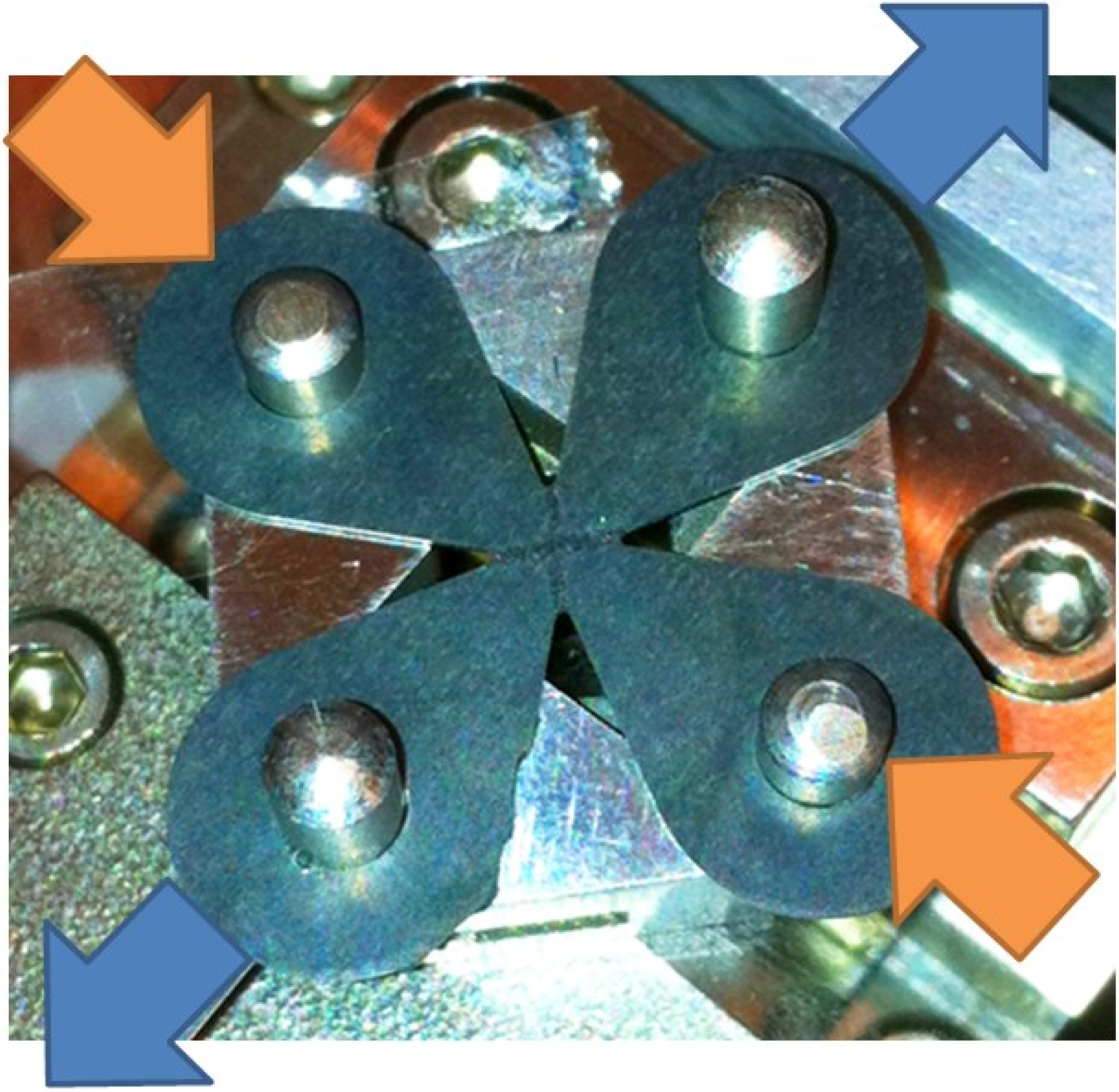

Figure II.2: Cruciform shaped sample that generates biaxial tension/compression to simulate planar shear in the center of gauge section. Blue arrow denotes the tensile axis, and the cross arms below the samples induce compression denoted by orange arrows. Note the formation of Lüders bands (black lines) in the gauge section. This is the zone of transformed martensite.

The sample in the shape of cruciform (Figure II.2) with a gauge section of $\sim 3\ mm \times \sim 3\ mm$ is laser cut from the sheet. It is then heat treated at $750°C$ for $30\ minutes$, followed by electropolish to mirror-like finish for µXRD characterization. The A_f temperature is chosen to be at $\sim 15°C$. This ensures the samples are fully austenitic before the transformation. Prior to the scanning, the sample is submerged in hot water to completely eliminate all pre-existing martensite. The heat treatment ensures the grains in the sample to be around $20\sim 50\ \mu m$ and suppresses transformation into R-phase. The grain coarsening is necessary to allow for characterization of multiple points of each grain to be taken during the sample.

The experiment uses a custom designed and built load frame from Deben (Deben Ltd. West Sussex, United Kingdom). It is capable of generating up to $2000\ N$ of load uniaxially. The characterization portion of the experiment is performed at Advanced Light Source at Lawrence Berkeley National Lab on beam line 12.3.2. The experiment uses the micro-X-ray diffraction capability to collect diffraction pattern from a spot ($\sim 1 \times \sim 1\ \mu m$). Due to time constraint, a mapping of $500\ \mu m$ by $500\ \mu m$ from the center of the gauge section with a stepping of $5\ \mu m$ is performed per scan. The *in situ* loading under micro-X-ray-diffraction allows for characterization of austenite phase under shear loading. With the raw diffraction patterns collected, further analysis allows the ability to compute spatially indexed grain map, pole figure, inverse pole figure, and stress/strain map at varying loads.

Near uniform shear loading is achieved at the center of specimen. Offline test reveals transformation zone forming a cross (Lüders bands) and expands to fill the gauge section (Figure II.2), as predicted from simple Finite Element Analysis of isotropic uniaxial Nitinol model (Abaqus). However non-uniform gauge cross-section with respect to the shear loading direction means non-uniform stress development. Constitutive shear behavior is difficult to analyze from force-displacement curve. However with the Nitinol model from Abaqus, the load-displacement curve is computed to be close to the measured curves.

Scans are taken at 0, 200 and $213N$. At $200N$, the gauge section is about 50% transformed. At $213N$, it is about 75% transformed. Higher loads were attempted, however due to the completely transformed gauge section, and the inability to interpret X-ray diffraction pattern of martensitic grains, the data collection is stopped after loading up to $213N$. Upon unloading, it is found that the shear loading has permanently deformed some of the martensite phase which precludes some reverse transformation to austenite phase. The cruciform was permanently deformed due to relatively high strain imposed by the experiment.

II.iv. Texture analysis of *in situ* multi-mode fatigue loading

Earlier experiments were conducted on monotonic loading of tensile and shear loading of Nitinol. This experiment is performed by cycling the same dogbone samples (in all three orientation, 0°, 45°, 90°) from Section II.ii under *in situ* µXRD characterization. Shear samples from Section II.iii were cycled and characterized accordingly. Due to time constraints and motor speed limitations ($50\ \mu m/sec$) only up to $100\ cycles$ of loading could be conducted for each set of samples. The characterization parameters are same as what is described in Section II.iii.

In addition to the dogbone, cruciform samples, and wire samples obtained from Nitinol Devices & Components, Inc. (NDC, Fremont, CA) are studied as well. Wire diameters about $1.2\ mm$ with same superelastic Nitinol $Ni_{50.8}Ti_{49.2}$ composition are selected. It is also heat treated to allow for grain coarsening to $20 \sim 50\ \mu m$ by annealing at $750°C$ at $30\ minutes$. The wires are then electropolished to a mirror-like finish. The A_f is finalized to be $16°C$, same as the other samples. The wires are clamped between two plates with dimples with set screws. This ensures stability during experiment. The same Deben rig is used, with load capacity up to $2000\ N$. Similarly only $100\ cycles$ are performed.

Collecting X-ray diffraction on wire is challenging due to the nature of curved surface of the wire. By aligning the incoming beam with the longitudinal axis of the wire and carefully aligning the machines, the curved surface errors are minimized. In this orientation, only line scans are possible for collection, therefore 4 500 μm long lines with 5 μm stepping in between are scanned. Given the beam spot size of roughly 1 $\mu m \times 1\ \mu m$, this covers nearly the entire bulk of the sample.

III. Torsional Fatigue of Nitinol

An increasing number of medical implant devices are manufactured from Nitinol, a near-equiatomic intermetallic nickel-titanium alloy, due to its unique characteristics of superelasticity and shape memory coupled with biocompatibility, large strain recovery and corrosion resistance [11]. Many of these medical devices, particularly endovascular stents, undergo tens to hundreds of millions of loading cycles in a corrosive physiological environment during their lifetime. Accordingly, to ensure their structural integrity during patient lifetimes, *in vitro* stress-life (S/N), or appropriately strain-life (ε/N), fatigue data are routinely determined for the alloy and combined with full component testing to develop design and life-prediction strategies for the safe use of the device.

The vast majority of stress- or strain-life fatigue data on Nitinol to support such life-prediction procedures is based on cyclic testing under uniaxial loading [47]. However, many medical devices, for example endovascular stents, are subjected to far more complex modes of loading in the body which have the potential to result in premature fractures. Recent studies have shown that arteries, particularly the superficial femoral artery (SFA), experience a dynamic combination of axial compression and extension, radial compression, bending, and torsion [44-47, 51-53]. In particular, three-dimensional magnetic resonance imaging (MRI) of the SFA has revealed that this artery undergoes significant twisting of 60° (±34°) when the hip and knee are flexed under simulated walking conditions [44, 51]. Despite these observations, current fatigue lifetime prediction analyses are based solely on uniaxial loading and thus may fall far short of accurately predicting the safe life of stents under these physiological multiaxial loading conditions. Specifically, ignoring modes of loading other than the regular pulsatile loads within the artery, as has been the general practice for stents up to now, has the potential for severe underestimates of safe lifetimes. Indeed, stents located in the SFA have been reported to fracture *in vivo* through the propagation of spiral cracks (termed "spiral dissection") [45, 54]. Furthermore, studies have shown a correlation between stent fracture and patency whereby stented vessels re-occlude due *in vivo* fatigue fractures [55]. This latter phenomenon suggests that the torsional loading experienced by stents is significant and thus must be incorporated in any design and life-prediction analyses of these components.

Under uniaxial conditions, the stress- or strain-life fatigue behavior of Nitinol has been investigated for many different types of loading, including rotary bending [56, 57], uniaxial fully reversed loading [58, 59], and bending [60]; for a recent comprehensive review, see ref. [47]. Data are generally collected in terms of the number of cycles to failure as a function of the applied alternating and mean stresses. However, because of its superelastic behavior, where significant (superelastic) global strain can occur at essentially constant stress, as shown by the plateau in the monotonic tensile stress-strain curve (Figure III.1), expressing lifetimes for Nitinol in terms of the applied strains, rather than stresses, is far more appropriate. Additionally, it is apparent that unlike most conventional metallic materials, the amplitude of the alternating strain in Nitinol has a much more significant effect on the fatigue life than the applied mean strain, at least for mean strains below ~1.5% [60-65].

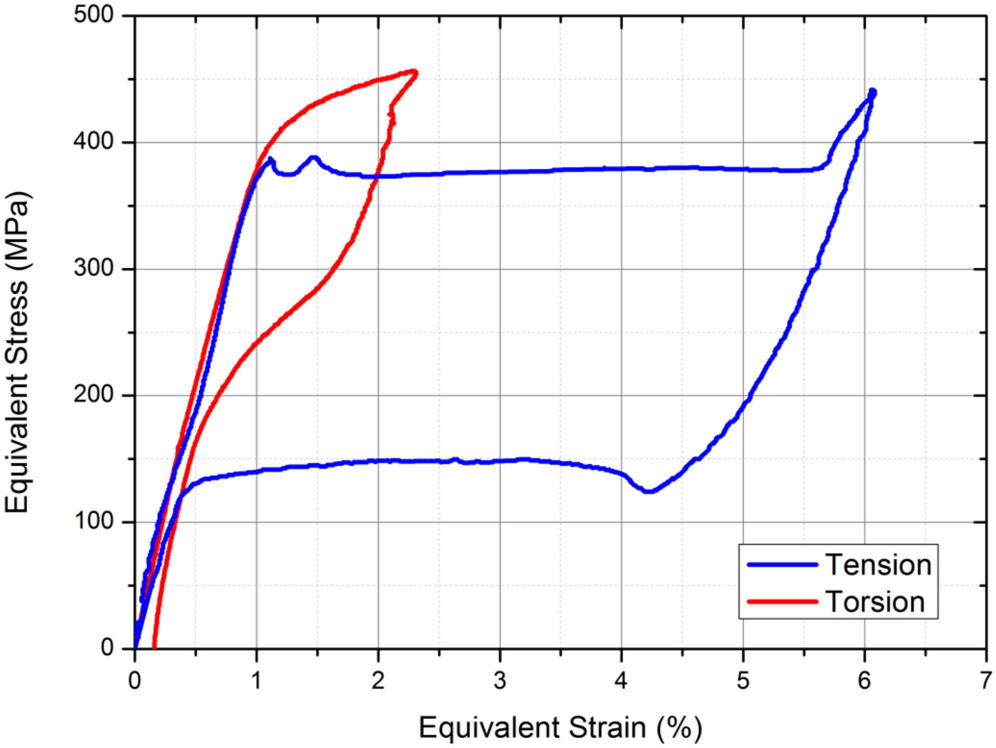

Figure III.1: Plot of the constitutive stress-strain and hysteresis behavior of superelastic austenitic Nitinol tubing loaded in axial tension vs. torsion. Although compared on the basis of the equivalent true (Cauchy) stress, $\bar{\sigma}$, as a function of the equivalent referential (Lagrangian) strain, $\bar{\varepsilon}$, there is nevertheless no normalization of the torsion and tension stress-strain curves under monotonic loading. Data from ref. [66].

The most complete study on the (uniaxial) strain-life fatigue of Nitinol is due to Pelton and co-workers [60, 61] who investigated diamond-shaped Nitinol samples, processed to emulate the commercial processing of Nitinol stents, which could be cycled in tension/compression by bending the diamond arms. Specifically, using finite element analysis to calibrate the stresses and strains in these test samples, where the highest strain conditions occurred on the arms of the diamond shape where the tensile and compressive stresses alternated between the bottom and the top of the arms, these authors generated a comprehensive data set for the strain-life fatigue of Nitinol under uniaxial conditions, specifically in tension/compression loading by bending.

Unlike tension/compression/bending loading, there are no corresponding comprehensive fatigue data available in the literature for the torsional fatigue loading of Nitinol, although a few studies pertain to torsional behavior under non-cyclic loads [67-71]. McNaney, Imbeni, *et al.* [68, 69] examined both the axial tension/compression and torsional stress-strain hysteresis behavior of the Nitinol tubing typically used to make commercial stents. These authors measured the (non-cyclic) stress/strain behavior in tension *vs*. torsion and compared the resulting stress/strain/hysteresis curves on the basis of the equivalent stress and equivalent strain; unlike traditional metallic materials, they found that no universal constitutive relationship in terms of the equivalent stress as a function of equivalent plastic strain existed.

In light of the MRI observations of the twisting of arteries and the current lack of information on the behavior of Nitinol alloys under torsional loads, especially the absence of S/N or ε/N fatigue data for torsion and/or mixed-mode loading, the current work is focused on determining the torsional strain-life fatigue curve for the superelastic Nitinol tubing used for stents, at several strain ratios of ($R_\varepsilon = \varepsilon_{min}/\varepsilon_{max}$) between -1 and 0.6, and comparing such data with existing strain-life data for a similar Nitinol alloy under tension/tension and tension/compression loading in bending. We further provide an approach for normalizing tension / compression / bending and torsional fatigue data in terms of the equivalent strain as a preliminary approach to developing a multiaxial design and lifetime-prediction methodology based on the equivalent alternating strain for Nitinol medical devices subjected to mixed-mode fatigue loading. Based on this methodology, we propose a modified Coffin-Manson relationship for the multiaxial fatigue of superelastic Nitinol which relates the number of cycles to failure to the alternating equivalent transformation strain.

III.i. Data analysis

Displacement and load data was collected for the single-cycle torsional tests to determine the hysteresis and constitutive behavior of the Nitinol tubes. Corresponding displacements and number of cycles to failure were measured for the fully reversed and mean strain amplitude fatigue torsional tests to create the ε/N curves for these conditions. Along with the sample geometry, the displacement and load data were respectively used to determine the shear stresses and shear strains applied to the samples during testing.

In order to compare the torsional hysteresis and fatigue data with previous results obtained under axial tension and compression [60, 61, 68, 69], the shear strain values were converted to equivalent strains. The results were expressed as the equivalent true (Cauchy) stress, $\bar{\sigma}$, and the equivalent referential (Lagrangian) strain, $\bar{\varepsilon}$. The data were converted by using $\bar{\sigma} = \sqrt{\sigma_t^2 + 3\sigma_s^2}$ and $\bar{\varepsilon} = \sqrt{\varepsilon_t^2 + 4/3\, \varepsilon_s^2}$, where σ_t and ε_t are, respectively, the tensile stress and strain and σ_s and ε_s are, respectively, the shear stress and strain. For the deformation range of interest in this work, *i.e.*, strains less than 5%, the transformation strains, ε_{tr}, are defined as the total strain minus the (purely) elastic strain.

III.ii. Torsional constitutive/hysteresis behavior

Single-cycle torsional tests were conducted to determine the constitutive and hysteresis behavior of the Nitinol tubing samples to various strain levels. Such data were then compared to our previous tension *vs*. torsional studies on a similar composition of Nitinol tested at a similar ΔT [60, 61, 68, 69]. Figure III.1 shows the uniaxial tension and torsional hysteresis loops plotted in terms of the equivalent stress and strain, the tensile data out to a tensile strain of 0.06, the torsional data out to a shear strain of 0.02.

III.iii. Torsional fatigue strain-life behavior

The strain-life torsional ε/N curve for superelastic Nitinol, based in samples tested with fully reversed loading out to 10^6 cycles at zero mean strain ($R_\varepsilon = -1$) is shown in Figure III.2 in the form of the lifetime (N_f) as a function of the applied shear strain amplitude $\Delta\varepsilon_s/2$; also plotted is the corresponding torsional data with a positive mean strain, *i.e.*, at $R_\varepsilon = 0.2$. Although there is only limited overlap of data, the positive mean strain ($R_\varepsilon = 0, 0.2, 0.6$) results do appear to merge reasonably well with the larger number of $R_\varepsilon = -1$ data points.

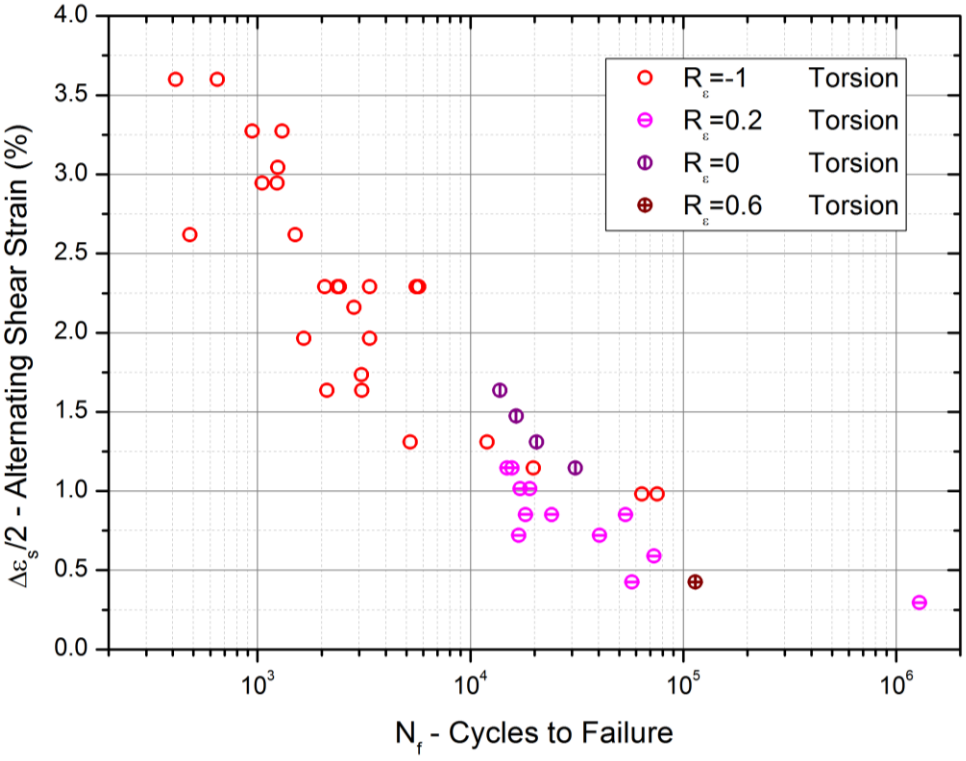

Figure III.2: Torsional fatigue ε/N diagram for superelastic austenitic Nitinol tubes, plotted in terms of the alternating shear strain, $\Delta\varepsilon_s/2$, as a function of the number of cycles, N_f, for tests under fully reversed (R_ε = -1) and applied mean strain (R_ε = 0, 0.2 and 0.6) conditions.

III.iv. Discussion

The comparison in Figure III.1 of the single-cycle constitutive/hysteresis behavior of superelastic austenitic Nitinol tubing under torsion as compared to axial tension/compression loading [68, 69] indicates that even when expressed in terms of the equivalent stress *vs*. equivalent strain, there is little to no normalization of behavior in the superelastic alloy (except in the purely elastic range); this is in contrast to what would be expected for classical (flow theory) plasticity in a traditional (non-superelastic) metal.

Despite this lack of correlation under non-cyclic loading in superelastic Nitinol, from the perspective of providing a basis for multiaxial fatigue, the equivalent stress approach is one of two classes of multiaxial fatigue models that have been successfully used to predict lifetimes or allowable stresses under complex states of stress, *e.g.,* [72, 73]; the other class of models is based on the so-called critical plane approach, *e.g.,* [74, 75]. Equivalent stress models are an extension of the J_2 flow theory of plasticity to cyclic loading; they are essentially the cyclic version of the von Mises initial yield criterion where the normal and shear stresses associated with the fatigue loading, both alternating and mean, are expressed as an equivalent stress. These models suffer from difficulties in defining the mean stress; moreover, from physical mechanism perspective they are fundamentally questionable as unlike continuum plasticity which is non-directional, damage in fatigue is crack formation which is highly directional and thus quite different in, for example, tension *vs*. shear. Despite these distractions, various versions of such equivalent stress models are in current widespread use for multiaxial fatigue. The other class of models, critical plane models *e.g.,* [74, 75], are loosely based on physical phenomena in that fatigue cracks are assumed to form on critical planes that are a function of the normal and shear stresses and strains on that plane; normal stresses/strains are assumed to open these cracks thereby reducing any crack-surface interference whereas shear stresses/strains cause dislocation motion along slip planes leading to crack initiation and growth.

As an initial strategy for multiaxial fatigue design and life prediction in superelastic Nitinol, we propose here a relatively simple strain-based approach based on the equivalent alternating strain.[2] The basis for this is two-fold. First, a comparison of the current torsional ε/N curves for the several R_ε ratios of -1, 0, 0.2 and 0.6, replotted in Figure III.3 in terms of the equivalent referential (Lagrangian) strain as the equivalent strain amplitude, $\Delta\bar{\varepsilon}/2$, as a function of the number of cycles, N_f, suggests a dominant effect of the cyclic, as opposed to mean, strain. Although there are only limited data at two of the four R_ε ratios, what is perhaps initially surprising about this comparison is how the data for the various strain ratios overlap, implying that the

---

[2] Aside from the fact that the "damage" in the form of cracks is directional (as alluded to above), from a fundamental perspective, the use of an equivalent strain approach for multiaxial loading of Nitinol could also be considered questionable from the fact that the progress of the *in situ* phase transformation, which is the basis of the superelastic deformation, is also directional.

effect of mean strain on the torsional fatigue life of Nitinol may be relatively small. We must presume here that the large superelastic strains associated with the deformation of Nitinol make it difficult to sustain a mean strain in fatigue, akin to the relaxation of mean stresses during low-cycle (Coffin-Manson [76, 77]) fatigue of a traditional cyclically plastically deforming metal.

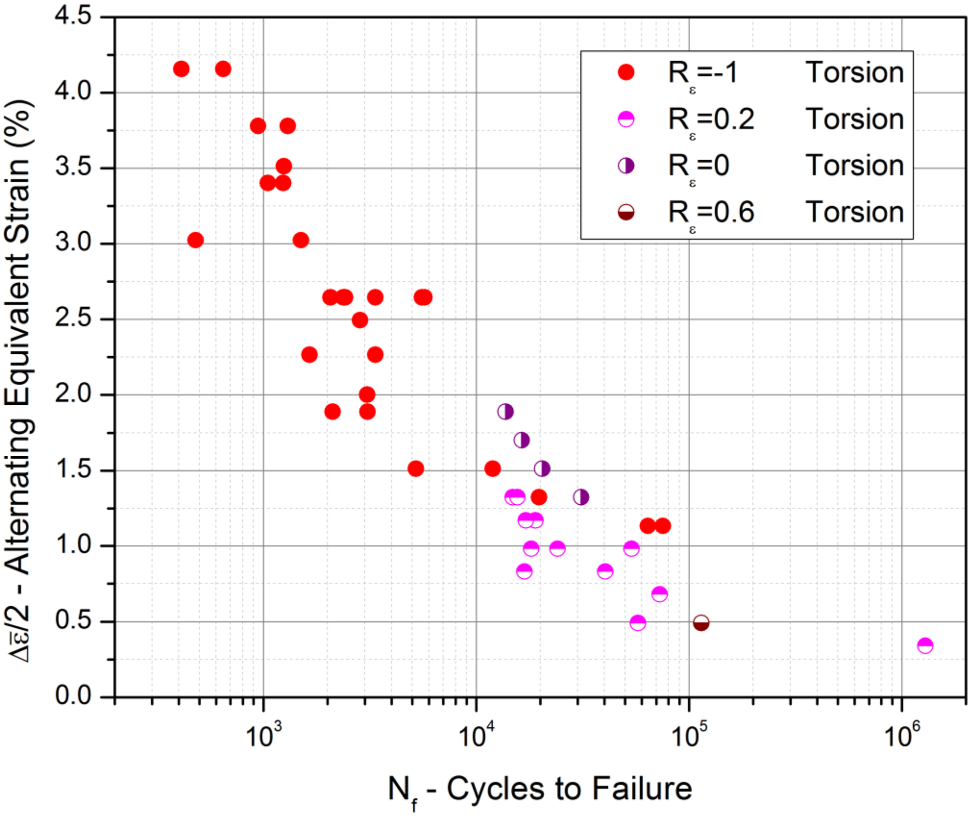

Figure III.3: Torsional fatigue ε/N diagram, plotted in terms of the alternating equivalent strain, $\Delta\bar{\varepsilon}/2$, as a function of the number of cycles, N_f, for superelastic austenitic Nitinol tubing tested under fully reversed (R_ε = -1) and applied mean strain ($R_\varepsilon = 0, 0.2$ and 0.6) conditions.

Second, if we compare our equivalent strain amplitude *vs*. number of cycles data for cyclic torsion at $R_\varepsilon = -1, 1, 0.2$ and 0.6 with the comprehensive strain-life data of Pelton, and co-workers [60, 61] for tension/compression loading ($-1 \leq R_\varepsilon \leq 0.6$) by bending of a Nitinol with an identical composition tested at the same ΔT, the resulting alternating equivalent strain, $\Delta\bar{\varepsilon}/2$ *vs*. N_f, curves display an excellent normalization (within experimental scatter) of the torsion and bending data on a single ε/N curve, for both zero (Figure III.4a) and non-zero (Figure III.4b) mean strain ($R_\varepsilon \leq 0.6$).

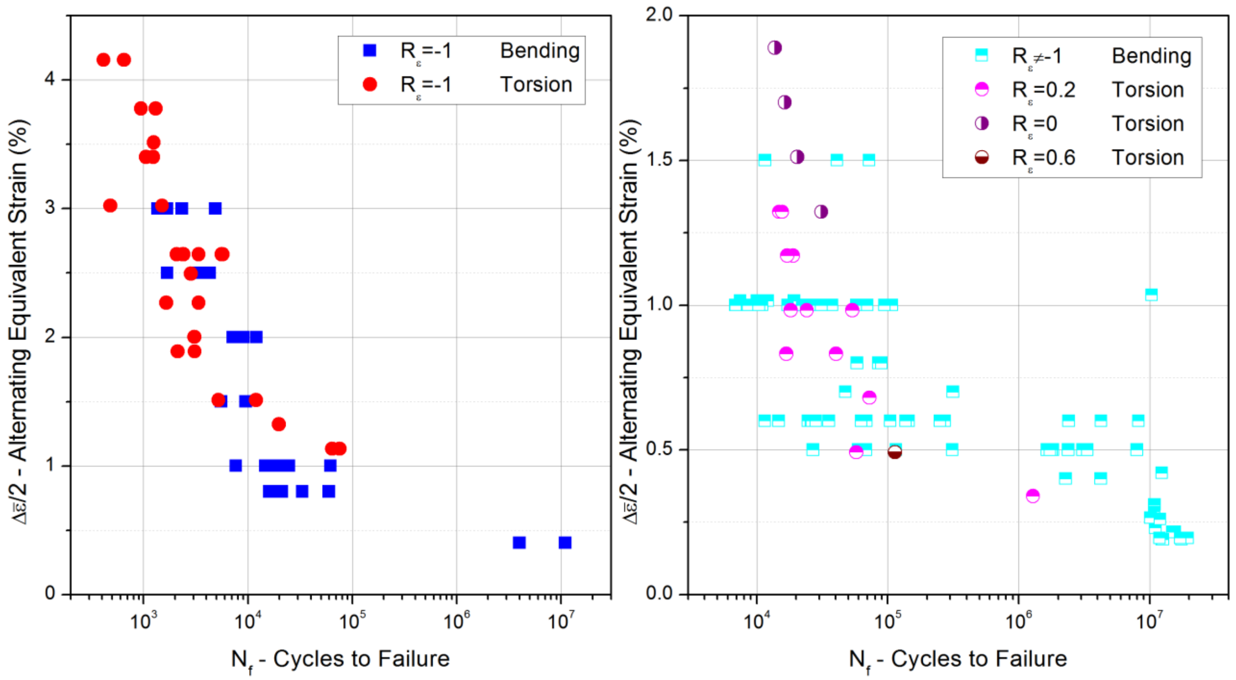

(a) (b)

Figure III.4: Multiaxial fatigue ε/N diagrams plotted in terms of the alternating equivalent strain, $\Delta\bar{\varepsilon}/2$, as a function of the number of cycles, N_f, for superelastic austenitic Nitinol tubing showing a comparison at lower mean strains ($-1 \leq R_\varepsilon \leq 0.6$) of torsion and axial tension/compression results (a) under fully reversed ($R_\varepsilon = -1$) loading and (b) with an applied mean strains ($R_\varepsilon = 0, 0.2$ and 0.6).

Indeed, replotting these data on a single alternating equivalent strain *vs.* number of cycles, $\Delta\bar{\varepsilon}/2$ *vs.* N_f, strain-life diagram for Nitinol tubing displays a remarkable normalization of superelastic Nitinol fatigue data in both tension/compression/bending and torsion tested *at lower mean strains* with R_ε ratios less than 0.6 (Figure III.5). However, as is apparent in the Figure III.5, the normalization breaks down at the highest mean strains, as shown by the tension-tension results where the R_e values approach 0.99.

An alternative and improved approach to displaying these data which can accommodate the high mean strain results is to incorporate a modified Coffin-Manson type equation [76, 77] for the multiaxial fatigue of Nitinol utilizing the number of cycles N_f as a function of the alternating equivalent transformation strain, $\Delta\bar{\varepsilon}_{tr}/2$.[3] Applying this notion to the current data for the torsion, bending and tension-tension fatigue of superelastic Nitinol over a wide range of strain ratios from R_e values of -1 out to 0.99 now reveals a “universal” fit (Figure III.6), which can be expressed in terms of the following relationship:

$$\Delta\bar{\varepsilon}_{tr}/2 = 61.7\, N_f^{-1/2} \ , \qquad (1)$$

---

[3] The equivalent transformation strain, $\bar{\varepsilon}_{tr}$, is defined as the total equivalent strain, $\bar{\varepsilon}$, minus the elastic equivalent strain, $\bar{\varepsilon}_{el}$, where $\bar{\varepsilon} = \bar{\varepsilon}_{el} + \bar{\varepsilon}_{tr}$.

with strains expressed in %. This expression is physically appealing in mechanistic terms and is purely analogous to the traditional Coffin-Manson relationship [76, 77], with essentially little to no effect of mean strain and no indication of an apparent "fatigue limit", but with the alternating plastic strain being replaced by the alternating equivalent transformation strain; in both cases, the relevant strain is the half-width of the fatigue (equivalent stress-strain) hysteresis loop.

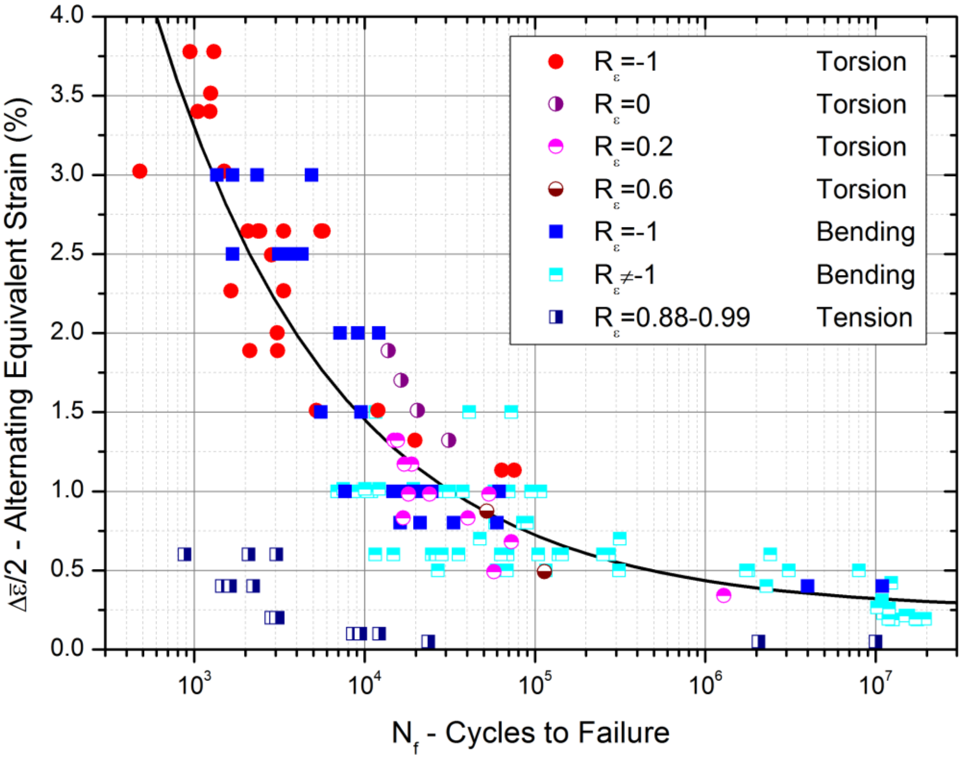

Figure III.5: Combined ε/N diagram for the multiaxial fatigue of superelastic Nitinol tubes plotted in terms of alternating equivalent strain, $\Delta\bar{\varepsilon}/2$, as a function of the number of cycles, N_f, showing normalization of multiple data sets of torsion, bending (tension/compression) and tension-tension fatigue results at multiple R_ε ratios. A curve fit is shown for the lower R_ε ratio results ($-1 \leq R_\varepsilon \leq 0.6$) as a possible simple constitutive equation: $\Delta\bar{\varepsilon}/2 = 0.25 + 49.6N_f^{-0.4}$ for multiaxial fatigue of Nitinol at lower mean strains. This formulation does not appear to work so well for very high mean strain ($R_\varepsilon \sim 0.99$) ε/N fatigue results.

Clearly both these proposed approaches for the characterization of multiaxial fatigue in superelastic Nitinol presented in Figure III.5 and Figure III.6 must be further validated with significantly more fatigue-life data, specifically over a wider range of mean *vs.* alternating strains, out to longer lifetimes approaching 10^8 cycles or more, and ideally with other loading modes (such as internal pressure, tension plus torsion both in and out of phase, *etc.*). However, both approaches are relatively simple and strongly suggest that as an initial description of multiaxial fatigue in biomedical Nitinol tubing, an alternating equivalent strain-based normalization (whether computed from the total or transformation strains), with a minimal role of mean strain, may offer a practical and workable solution. It should be noted though that the total equivalent strain formulation does not do a satisfactory job in normalizing the very high mean strain ($R_\varepsilon \sim 0.99$) data, and should only be used at low mean strains ($R_\varepsilon \le 0.6$). Constitutive relationships that more fully encompass the multiaxial deformations experienced *in vivo* will also lead to higher resolution predictive finite element models, such as those used for design and analysis of Nitinol implants. Indeed, the incorporation of such multiaxial constitutive and lifetime models is essential in these numerical models for the design of safer prostheses. As nearly all Nitinol medical devices experience complex multiaxial loading conditions *in vivo* with the potential of premature fatigue failure, such equivalent strain amplitude approaches clearly show excellent promise as relatively straightforward means of predicting allowable in-service loading conditions and safe lives for implant devices subjected to mixed-mode physiological loads.

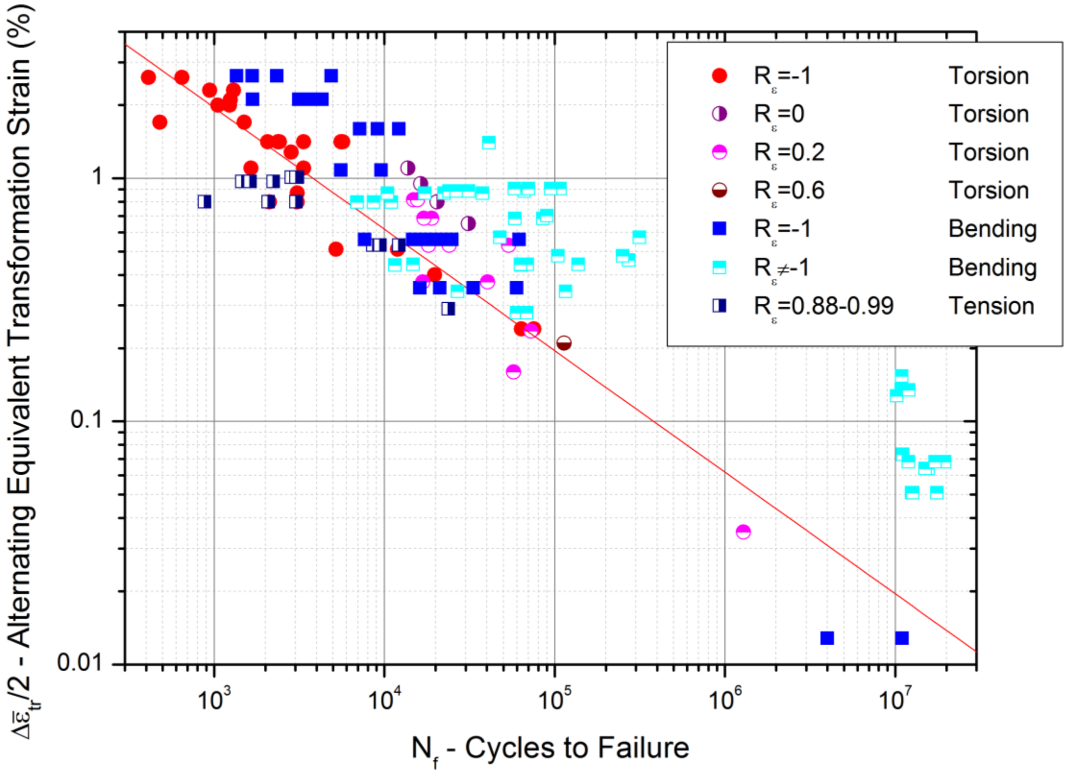

Figure III.6: A modified Coffin-Mason relationship for the multiaxial fatigue ($-1 \le R_\varepsilon \le 0.6$) of superelastic Nitinol involving the alternating equivalent transformation strain, $\Delta\bar{\varepsilon}_{tr}$, as a function of the number of cycles to failure, N_f, where $(\Delta\bar{\varepsilon}_{tr}/2)N_f^{-1/2} = 61.7$. Note how this approach normalizes the ε/N data even for the highest mean strain ($R_\varepsilon \sim 0.99$) results.

III.v. Conclusions

Using the stress/strain life (S/N or ε/N) methodology, a study was made of the cyclic fatigue in torsion (with and without a mean strain) of superelastic Nitinol tubing, processed in a similar fashion to the material used in many biomedical devices such as endovascular stents. Based on this study, the following conclusions can be made:

1. Although the single-cycle constitutive/hysteresis (stress *vs*. strain) behavior of Nitinol under torsion and axial tension loading are quite distinct and cannot be well correlated by plotting in terms of the equivalent true (Cauchy) stress, $\bar{\sigma}$, *vs*. the equivalent referential (Lagrangian) strain, $\bar{\varepsilon}$, this approach may hold promise for normalizing cyclic fatigue data using a strain-based methodology.
2. Experimentally-measured torsional fatigue ε/N diagrams for Nitinol, plotted either as the shear strain amplitude, $\Delta\varepsilon_s/2$, or the equivalent strain amplitude, $\Delta\bar{\varepsilon}/2$, as a function of the number of cycles to failure, N_f, were found to show increased lives at lower strain amplitudes but with a minimal effect of the mean strain. Accordingly, results at a zero mean strain ($R_\varepsilon = -1$) appear to fall on the same torsional ε/N curve as results at a positive mean stress ($i.e.,$ at $R_\varepsilon = 0$ to 0.6), where R_ε is defined as the ratio of minimum to maximum strain.
3. When compared with a comprehensive set of ε/N fatigue data, for Nitinol of similar composition and processes, tested in bending, excellent correlation between the torsional fatigue and tension/compression (bending) fatigue was found for both zero mean strain loading ($R_\varepsilon = -1$) and positive mean strain loading ($R_\varepsilon =$ 0, 0.2 and 0.6) when results were expressed in terms of the alternating equivalent strain, $\Delta\bar{\varepsilon}/2$, as a function of the number of cycles to failure, N_f. Although working well with lower mean strain ($-1 \leq R_\varepsilon \leq$ 0.6) ε/N data, this approach did not do a satisfactory job of normalizing higher mean strain ($R_\varepsilon \sim$ 0.9) data from tension/tension tests.
4. An improved approach for a multiaxial fatigue-life relationship for superelastic Nitinol can be expressed in terms of a Coffin-Manson type formulation where the alternating equivalent transformation strain (or half-width of the equivalent stress-strain hysteresis loop) is related to the minus one-half power of the number of cycles to failure, $\Delta\bar{\varepsilon}_{tr}/2 \propto N_f^{-1/2}$. This approach provides a satisfactory normalization for all testing modes studied (torsion, tension/tension and bending) over the entire range of strain ratios from R_ε values of -1 out to 0.99.
5. Accordingly, for the design and the prediction of allowable stresses and safe lifetimes for medical devices manufactured from superelastic Nitinol tubing and subjected to complex loading involving mixed-mode, *i.e*., tension/compression/bending plus torsion conditions, we are advocating simple equivalent strain amplitude based approaches for multiaxial fatigue. We find that either approach involving alternating equivalent strain *vs*. lifetime ε/N diagrams does an excellent job in normalizing results from different loading config-

urations, specifically tension, bending and torsion, at lower mean strains (*i.e.*, R_ε-ratios below 0.6), the modified Coffin-Manson approach utilizing the alternating equivalent transformation strain provides a superior basis for a multiaxial fatigue law for superelastic Nitinol over a very wide range of mean strains ($-1 \leq R_\varepsilon \leq 0.99$) in torsion, tension and bending, with the alternating strain playing a dominant role compared to the mean strain.

III.vi. Nomenclature

- *Alternating shear strain,* $\Delta\varepsilon_s/2$: the half amplitude of shear strain in a torsional fatigue test
- *Applied shear strain*, $\Delta\varepsilon_s$: the shear strain range associated with fatigue test in torsion
- *Applied shear stress*, $\Delta\sigma_s$: the shear stress range associated with fatigue test in torsion
- *Applied tensile strain,* $\Delta\varepsilon_t$: the tensile strain range associated with a fatigue test in tension
- *Applied tensile stress,* $\Delta\sigma_t$: the tensile stress range associated with a fatigue test in tension
- *Cycles to failure,* N_f: The lifetime of a fatigue sample under an applied cyclic load in cycles
- *Elastic strain,* $\boldsymbol{\varepsilon_{el}}$: the range of the strain associated with only the linear elastic deformation of austenite phase in a fatigue test, as defined by total stress over the elastic modulus, $\boldsymbol{\varepsilon_{el} = \sigma/E}$
- *Equivalent alternating strain,* $\Delta\bar{\varepsilon}/2$: the equivalent strain half amplitude of a torsional fatigue test
- *Equivalent alternating transformation strain,* $\Delta\bar{\varepsilon}_{tr}/2$: the half amplitude of transformation strain associated with a fatigue test
- Equivalent elastic strain, $\bar{\varepsilon}_{el}$: the equivalent strain of elastic strain, where $\bar{\varepsilon} = \bar{\varepsilon}_{el} + \bar{\varepsilon}_{tr}$
- Equivalent transformation strain, $\bar{\varepsilon}_{tr}$: the equivalent strain of transformation strain, where $\bar{\varepsilon} = \bar{\varepsilon}_{el} + \bar{\varepsilon}_{tr}$
- Equivalent strain, $\bar{\varepsilon}$: referential (Lagrangian) strain, where $\bar{\varepsilon} = \sqrt{\varepsilon_t^2 + 4/3\ \varepsilon_s^2}$
- Equivalent stress, $\bar{\sigma}$: true (Cauchy) stress, where $\bar{\sigma} = \sqrt{\sigma_t^2 + 3\sigma_s^2}$
- *Strain ratio,* R_ε: The ratio between minimum and maximum strain in a fatigue test
- *Temperature differential,* $\Delta T = T - A_f$: representing a difference, between the testing/service temperature, *T,* and A_f
- *Transformation strain,* $\boldsymbol{\varepsilon_{tr}}$: the range of strain associated with the transformation between austenite to martensite in a fatigue test, as defined by the total strain subtracting elastic unloading: $\boldsymbol{\varepsilon_{tr} = \varepsilon - \varepsilon_{el} = \varepsilon - \sigma/E}$

IV. In-situ Texture Study of Uniaxial Deformation

Deployment of self-expanding stents, manufactured from the near-equiatomic Nitinol alloy Nitinol is an effective, lower risk therapy alternative to surgery and represents a major advance in fight against cardiovascular disease [78]. Due to the first-order thermo-mechanical phase transition from cubic austenite to monoclinic martensite phase, Nitinol can undergo several times larger reversible deformation than conventional biomaterials such as stainless steel or titanium. This feature makes Nitinol optimally compliant to withstand large crimp and deployment strains (up to 10%) as well as cyclic deformations experienced by the peripheral vessels, while maintaining vessel patency. Indeed, such superelasticity in Nitinol has been exploited in many other biomedical applications, from endodontic files to spinal prostheses [79].

Nitinol biomedical devices are manufactured from wires, thin rods, sheet, strip or thin-walled tubes, all of which are formed by a series of hot and cold working operations from cast ingots to final shape. The multistage thermomechanical processes impart deformations that significantly affect the microstructure (grain size, defect density, and crystallographic orientation). For example, there is a million fold reduction in the cross sectional area in fabricating a $0.5\,mm$ diameter wire, commonly used for many biomedical applications, from the original ($500\,mm$ diameter) as-cast ingot. As such, the grain refinement and crystallographic texture formation resulting from these manufacturing processes can be considerable.

Figure IV.1 shows two versions of a generic stent pattern[4] (laser cut from thin-walled tubes. The as-cut pattern (a) is from a $2\,mm$ diameter tube (so-called "closed configuration"), whereas the pattern in (b) is from an $8\,mm$ diameter tube ("open configuration")[5]. After thermal expansion of both stents to $10\,mm$ diameter, the stent that was laser machined in the closed configuration (c) is macroscopically identical to that of open configuration stent (d). Note, however, that the orientation of the tube axis, and hence the drawing direction (indicated by the arrow) relative to the major axis of the struts in the open and the closed configuration of stents, are significantly different. Though still poorly understood, the influence of microstructural orientation on the superelastic response of Nitinol is known to be significant [80]. As demonstrated [48], the radial pressure exerted by a Nitinol stent is proportional to the mechanical properties of a "V" section of the final stent geometry. Consequently, differences in crystallographic texture for macroscopically identical stents may result in stents experiencing markedly different cumulative radial forces.

---

[4] http://Nitinoluniversity.com/open-stent-design/

[5] The terms "open" and "closed" configuration refer to the manner in which the stents are manufactured and should not be confused with "open" and "closed" cell geometry verbiage used in stent design.

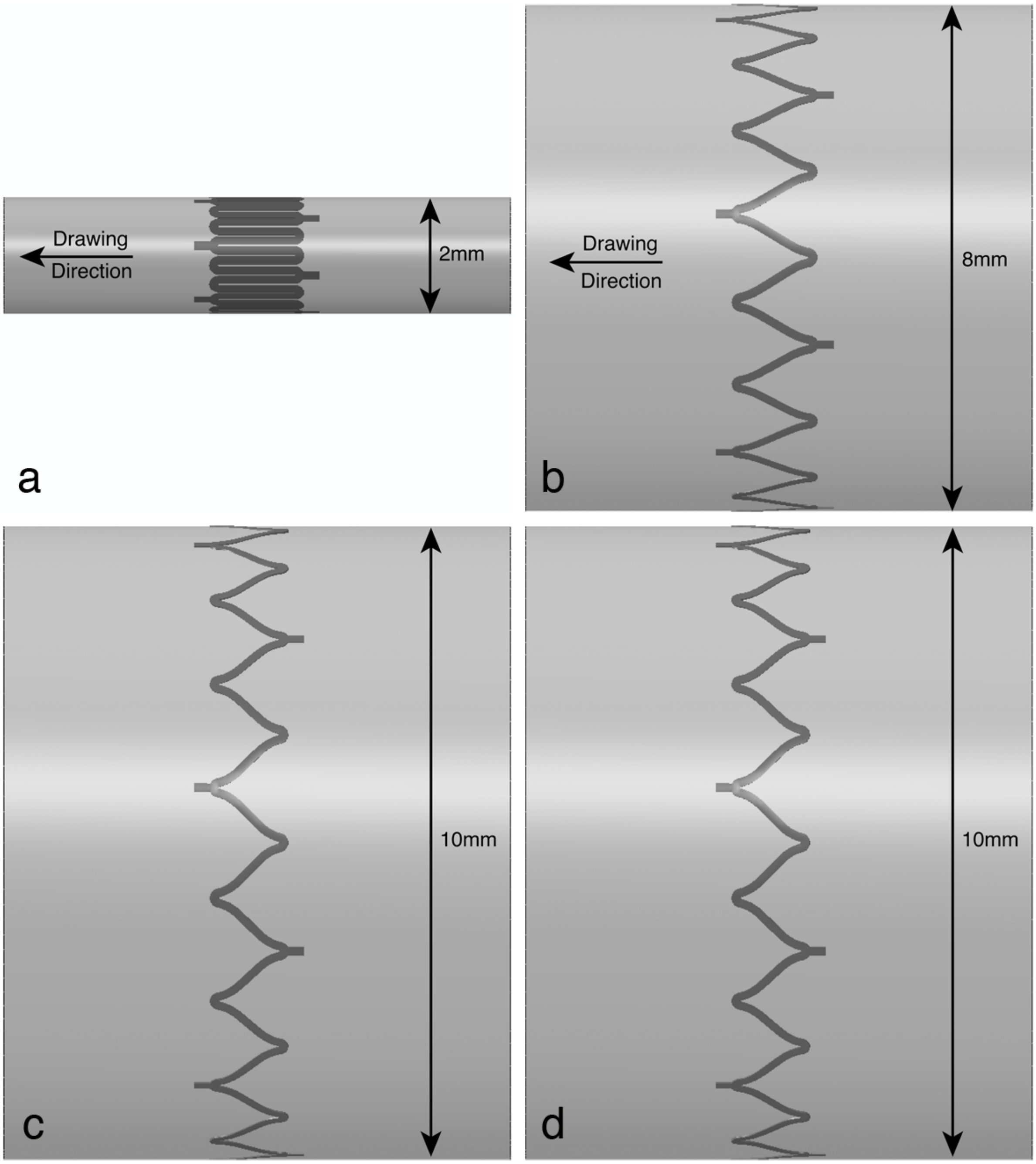

Figure IV.1: Illustration of the effects of starting tube diameter to produce a $10mm$ diameter Nitinol stent. Figure IV.1a shows the as-cut layout of a row of a generic stent from a $2\ mm$ tube ("closed configuration"). Note that the struts align with the tube drawing direction. Figure IV.1b shows the same stent laid out on an $8\ mm$ tube ("open configuration"). In this case, the struts are aligned at an angle to the tube drawing direction. Figure IV.1c and d show the stents when expanded to their final $10\ mm$ dimension.

Cardiac cycles and musculoskeletal motions subject biomedical devices to millions of complex deformations. For example, a stent deployed in the superficial femoral artery (SFA) undergoes severe multiaxial displacements from pulsatile motion (ca. 4×10^7 cycles annually) plus up to 60% rotation and up to 20% contraction (at a rate of ca. 1×10^6 cycles annually) as the leg is bent during a walking cycle [81, 82]. To design a device to withstand these frequent and severe deformations, finite element analytical (FEA) models of complex structures such as endovascular stents are generated by creating a fine elemental mesh of the geometry [83]. The models attempt to incorporate the highly non-linear mechanical response of Nitinol from global monotonic stress-strain relationships. But as the microstructural and textural effects alluded above are still poorly understood, they are ignored in current commercially available computational design models; this leads to predictions that are only qualitative and deviate significantly from the actual response at large deformation, as demonstrated previously [84]. Occasionally, therefore, an implant unexpectedly fractures *in vivo*, resulting in loss of vessel patency, and requires a major invasive surgery [48].

X-ray micro-diffraction from a synchrotron radiation source was the primary tool used to characterize the microstructural features, including grain size and grain orientation. This technique is the only method with sufficient spatial resolution ($< 10\ \mu m$) to allow detailed analysis of a 'bulk' specimen on the order of a stent strut. Furthermore, this technique provides the highest resolution strain gauge that can distinguish among different modes of strain accommodation, *i.e.,* elastic, plastic, or phase transformational strain.

The goal of the investigation reported here is to develop a deeper understanding of the role of microstructure and texture on the martensite phase transformation and superelastic response. This understanding will lead to a more accurate simulation of the mechanical response of Nitinol device.

IV.i. Results and Discussion

IV.i.1. Global Mechanical Anisotropy

Figure IV.2 shows the global "superelastic" stress-strain curve consisting of two linear elastic regions separated by a "stress plateau" for the 0°, 45°, and, 90° specimen orientations. Whereas the 0° and 90° samples were nominally identical and match the predictions of martensitic theories of single crystals [85], every characteristic of the 45° specimens, including the stress at the onset, slope, and length of the superelastic "plateau", displayed a significantly different behavior and differ considerably from the theoretical predictions.

Orientation-dependent behavior, as shown here, suggests that the two macroscopically identical stents shown in Figure IV.1 will have significantly different mechanical response. These data additionally explain why past attempts to estimate the superelastic mechanical response by codifying phenomenological bulk stress-strain curves [83, 86] have not been very successful. Similar differences in the stress-strain response were also seen when the mode of deformation (*i.e.*, tension, compression, bending, and torsion) was varied [66, 87].

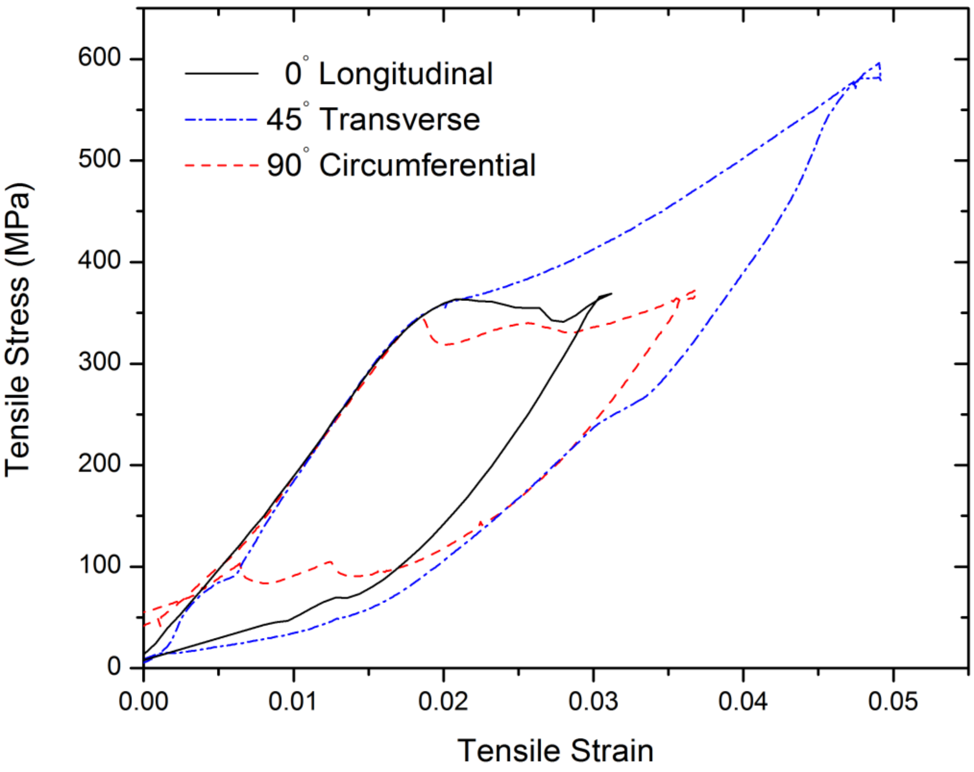

Figure IV.2: Global uniaxial tensile stress-strain curves for Nitinol machined in the Longitudinal, Transverse, and Circumferential directions, *i.e.*, respectively, 0°, 45°, and 90° to the drawing direction.

Orientation-dependent behavior, as shown here, suggest that the two macroscopically identical stents shown in Figure IV.1 will have a significantly different mechanical response and why past attempts to estimate the superelastic mechanical response by codifying a generic uniaxial tensile stress-strain curve [83, 86] have not been very successful. The highly textured microstructure of a thermomechanically processed Nitinol is thought to be the cause of the large variation in the stress-strain behavior observed in Figure IV.2. Thus, to understand the global mechanical response of a superelastic material, a microstructural understanding of the relationship among the grain orientation, phase transformation pattern, and local stress distribution is essential.

IV.i.2. Martensitic Transformation and Global Mechanical Behavior

The impact of the pattern of martensitic transformation on the global mechanical behavior[6] is most clearly seen in a plot of the externally applied stress *vs*. the fraction of the gauge length transformed to martensite. Figure IV.3 shows such relationship for 0°, 90°, and 45° specimens obtained from our *in situ* μXRD measurements. Comparison among curves with different orientations mimics the differences seen in Figure IV.2 in the features of the superelastic plateau. The 45° specimens differ from the 0° (and the 90°)[7] specimen in three distinct ways: (i) stress at which transformation plateau begins, (ii) the slope of the plateau, and (iii) the percentage of martensite at the end of the macroscopic stress plateau.

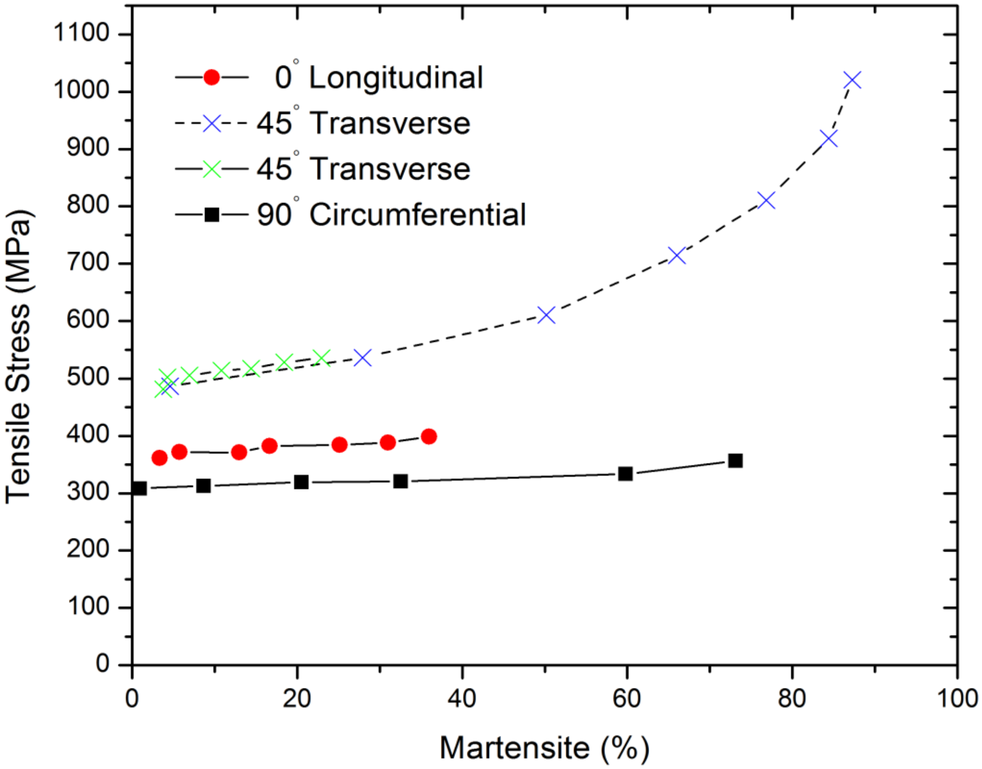

Figure IV.3: The variation in % martensite transformed as a function of the tensile stress, as measured during the *in situ* deformation of Nitinol dogbone samples, machined in the Longitudinal, Transverse, and Circumferential directions, *i.e.*, respectively, 0°, 45°, and 90° to the drawing direction.

---

[6] Here we define the global behavior as the cumulative stress-strain response of the entire collective of grains that comprise the gauge section. As such the macroscopic tensile stress is equal to the applied load divided by the gauge cross sectional area and the global strain is the change in gauge length divided by the original length.

[7] The 0° and 90° orientations have comparable global mechanical response, texture, and strain distribution and therefore, for the purposes of this paper, they will henceforth be collectively called 0° specimens.

The 0° specimens begin to transform when the macroscopic tensile stress is nominally 350 MPa, whereas the macroscopic plateau does not appear in the 45° sample until the macroscopic tensile stress reaches approximately 500 MPa, showing a 40∼60% higher stress required for the onset of stress-induced martensite. Initial progression of transformation in the 0° (or the 90°) specimens requires very little additional stress, resulting in a fairly flat plateau in the stress-strain response. On the other hand, even after the onset of transformation in the 45° specimens, further transformation requires a significant additional stress, leading to a plateau with a distinctly upward slope. Finally, contrary to common belief, the end of the plateau region does not coincide with complete transformation to martensite. Even for the easily transformable 0° specimen, when the applied stress begins to increase, effectively ending the global stress-strain plateau, as much as 20% of the gauge length has remained untransformed. For the 45° specimen the transformation plateau is even shorter with as much as 50% of the gauge untransformed before the stress begins to increase steeply again. These three distinct differences in the way the gauge length transforms to martensite between the various orientations of specimens, summarized in Table IV-1, can explain the majority of the variations seen in the superelastic stress-strain curves (Figure IV.2). For instance, significantly higher stress to initiate nucleation in the 45° samples manifests as a much higher stress plateau, whereas the difficult propagation of martensite for the 45° samples manifests as a steeper and shorter stress plateau[8].

Table IV-1: Characteristics of the uniaxial stress/strain behavior of the 45° and 0° Nitinol specimens

	Initial transformation plateau stress (MPa)	Plateau slope (MPa)[9]	Percent martensite at plateau termination	Dominant grain orientation
45° specimen	500	∼2000	∼50%	$\langle 100\rangle$
0° specimen	350	∼400	∼80%	$\langle 111\rangle$
90° specimen	300	∼400	∼80%	$\langle 110\rangle$

IV.i.3. Local Transformation Pattern and Elastic Strain Map

As presented above, the austenite in the 0° and 45° specimens appears to transform in a markedly different manner, leading to different superelastic responses. In an attempt to understand these differences at the microstructural level, we probed the transformation at the scale of individual grains. Figure IV.4 shows a map of the local grain orientation (along the load axis) with the global texture shown on an inverse pole figure for the 0° and 45° specimens. Naturally, as these samples were cut from tubes that routinely undergo several thermomechanical drawing process-

---

[8] There are noticeable differences in the slope of the austenite linear elastic region (*i.e.*, modulus) as well. These arise from the elastic anisotropy of the austenite phase that is discussed in detail elsewhere (Barney, et al. *unpublished results)*

[9] The slopes of the plateau for the 0° and 90° specimens are difficult to determine because of large non-monotonic variations.

es, they are not only heavily textured but have dramatically different crystallographic textures from each other. The 45° specimens have predominantly ⟨100⟩ type grain orientations, whereas the 0° specimens have predominantly ⟨111⟩ type grains along the deformation axis. Notably, there are clusters of grains in both orientations that are significantly misoriented with respect to their neighbors and the average grain orientation (*i.e.*, global texture). This is most easily noticeable for ⟨100⟩ orientated grains, seen to form narrow bands spaced along the length of the specimen.

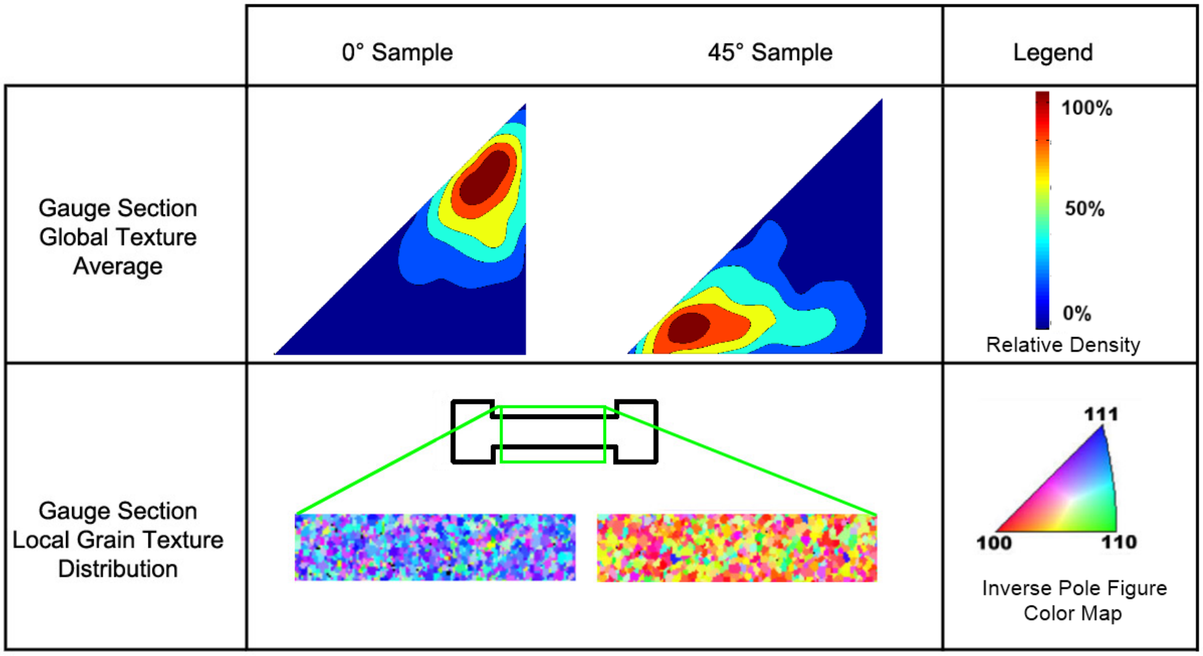

Figure IV.4: The local texture variations versus the global averaged textures. 0° samples have an averaged texture of ⟨111⟩, whereas 45° samples have an averaged texture of ⟨100⟩. The local distributions show the existence grains that are highly misoriented from the global average.

Figure IV.5 shows the austenite elastic strain maps for both orientations with progressively increasing tensile deformations. (Larger deformations are lower on the map “column”.) The blackened pixels, increasing in population going down a column, are regions that have transformed to martensite. The figure shows the way the austenite transforms to martensite and the way elastic strain distributes along the gauge are significantly different between the 0° and 45° orientations, although there are many characteristics of the transformation that are common to all orientations.

For every orientation that we studied, the gauge length transformed through multiple nucleation events that appear to occur frequently at grain boundaries (often at high-angle grain boundaries) near ⟨111⟩ and ⟨110⟩ type grains [88]. The growth of martensite from this nucleation point is irregular; the transformation front occasionally “leap-frogs”, leaving behind islands of untransformed austenite. The resulting transformed region is almost never contiguous. In many macroscopic measurements, especially on nanocrystalline material deformed at high strain rates, superelastic transformation appears to form a uniform—Lüders-like—band, but even in some optical measurements of larger grain material and at low deformation rate transformation region appears to be far from homogeneous [89]. Furthermore, most of the austenite grains in the specimens bear no more than 1.2% elastic strain, even when the average macroscopic strain is several times greater. A separate study [61] shows that the elastic strain in transformed martensite is even less than in austenite; therefore, transformational strain accounts for a large fraction of strain with increasing deformation. The islands of trapped and untransformed material, on the other hand, are the exception to this observation. They sustain progressively larger elastic strain, often significantly greater than 1.2%, as the specimen is further deformed, giving rise to an increasing slope to the plateau.

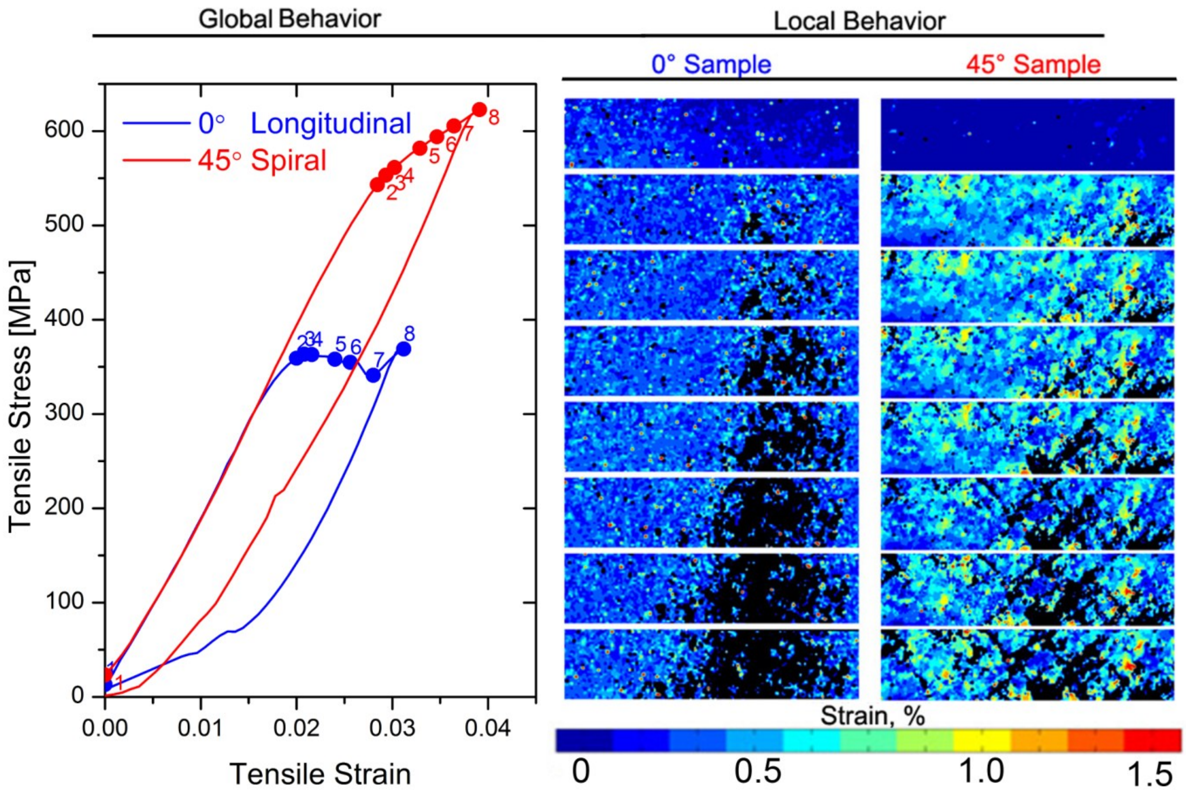

Figure IV.5: The strain evolution of 0° and 45° samples as a function of increasing deformation. Both samples develop region of transformed martensite (black), however the morphology of transformed region is different. 0° samples have flat, nearly uniform region, whereas 45° samples develops highly heterogeneous diagonal bands that cuts across the samples. Furthermore, both sets of samples feature regions of austenite that are highly strained, beyond the typical 1.2% threshold for martensite transformation.

The most difficult grains to transform appear to be those with ⟨100⟩ orientation, in agreement with observations of shape memory transformations in single crystals [90]. In contrast, the transformational stress for ⟨111⟩ and ⟨110⟩ orientations is quite similar and significantly lower than the ⟨100⟩ orientation. These observations can be partially explained by considering the Taylor factor for the shape strain among the various grain orientation variants under the influence of applied stress [18, 80, 85, 91]. Furthermore, our observations indicate that when a grain transforms, it frequently reduces the elastic strain, and hence the stress, on adjacent grains. A similar stress reduction is also observed in macroscopic measurements [92]. Often this local stress redistribution results in a redirection of the transformation front that, in some cases, encircles a region of untransformed austenite. Grains entrapped in an island in this manner have no dominant orientation and often transform subsequently. However, trapped islands of predominantly ⟨100⟩ type grains bear progressively larger strains and often require significantly greater applied stress for transformation, resulting in the plateau ending before the entire gauge length transforms to martensite. Robertson, *et al*. [50] also observed a similar redirection of the transformation front around a ⟨100⟩ grain as part of an *in situ* µXRD investigation of an advancing crack in fatigued Nitinol.

IV.i.4. Origin of the Large Variation in Global Mechanical Behavior

The difference between the nature of the deformation of the two types orientations is captured entirely in the difference the martensite transformation takes through the two microstructures. The path of the transformation in both types of orientations is influenced by the local grain orientation and the redistribution of the local elastic stress field in adjacent grains once a grain transforms. For the 0° specimens, martensite transformations nucleate at multiple nearby sites, which often coalesce into a single front, propagating across the width of the sample gauge in a macroscopic Lüders-like band. When the almost contiguous transformation band in the 0° specimens encounters a transverse band of ⟨100⟩ grains, transformation halts, and the subsequent elongation increases the elastic strain (and hence the elastic stress) mostly in these ⟨100⟩ grains. Often, new martensite tends to nucleate on the other side of the ⟨100⟩ band, leaving behind trapped ⟨100⟩ islands with elevated elastic strain in the wake of the transformation. In contrast, as soon as the first grains transform, the gauge length of the 45° specimen becomes decorated with higher-strain 45° crisscross patterns that appear to be predictive of the progressive transformation; these cross-hatch patterns are predominantly composed of ⟨100⟩ grains. Martensite nucleates in between one of these 45° crisscross bands and propagates until it reaches another highly strained cross band. When this occurs, transformation halts until the stress increases to nucleate martensite in another valley in-between a set of cross-hatched highly strained bands. Eventually a 45° crisscross pattern of transformation emerges, the boundaries decorated by highly strained ⟨100⟩ grains. The torturous, start-stop pathway of martensite transformation leads to higher, steeper, and shorter macroscopic stress-strain plateau.

The location and the orientation of these difficult to transform ⟨100⟩ grains, therefore, appear to dictate the path martensite transformation takes in textured superelastic Nitinol and consequently affects the character of the stress-strain plateau and the superelastic response. Although some researchers have evaluated macroscopic, texture-dependent transformations [93] and others have studied grain-dependent fracture paths [50], it is believe that this study is the first to report the critical influence of the orientation of individual grains, and the type of grain boundaries between them, on mechanical behavior of polycrystalline superelastic Nitinol.

IV.ii. Conclusions

The insights gained here on the role of local grain orientation on the nature of the martensitic phase transformation in Nitinol give a much fuller understanding of the factors that influence superelastic response in Nitinol. Specifically, this study indicates microstructural level processes by which stresses can redistribute upon phase transformation, leading to stress hot spots in conventionally unexpected locations. Uneven stress distribution, and especially the stress hot spots, may trigger unforeseen fractures and strongly impact fatigue life. The microstructural driven effects observed here, especially incomplete transformation at the end of the transformation plateau, can explain the reported deviation of mechanical response of Nitinol components at high deformation from the prediction of FEA [84].

The results also indicate that for more reliable predictions of mechanical response and hence more robust stent designs, FEA models cannot depend on universal monotonic stress-strain relationships, but must use relationships that are specific to crystallographic texture of the stent struts. For example, if the "open" and "closed" configuration stents shown in Figure 1 are fabricated from tubes which have undergone traditional tube-drawing thermomechanical processes, then the crystallographic texture along the struts for the two types of stents will be markedly different from each other. The results suggest that the mechanical response of these macroscopically identical stents will be significantly different from each other, and cannot be modeled with a common global stress-strain relationship. The struts of stents in the "closed" configuration are along the drawing direction, and hence, as a first approximation, they will respond in accordance with the parameters listed in Table IV-1 for the 0° specimen; whereas the struts in the "open" configuration are cut along a steeply oblique direction to the tube axis, and hence the parameters listed for the 45° specimen will most likely result in more failed predictions. The improvement in predictions for the mechanical response of superelastic Nitinol devices will, therefore, begin to occur as the large crystallographic transformation anisotropy, explored here, and still poorly understood crystallographic elastic anisotropy is gradually incorporated in the commercial numerical simulation models.

In conclusion, the observations of microstructural level effects on the global mechanical response investigated here is the beginning of a deeper understanding of the performance and the origin of some of the unpredicted failures of real world, superelastic Nitinol devices. We believe that our approach of relating global mechanical response to the local deformation physics will eventually lead to an increase in the fidelity of computational predictions of performance and fatigue life and ultimately to more reliable Nitinol endovascular stents and medical devices.

IV.iii. Summaries

- Nitinol tubing is used for self-expanding stents and other medical device implants.
- Processing imparts a strong texture in the tubing.
- Synchrotron μXRD is used to characterize tube specimens at 0°, 45° and 90°.
- A direct correspondence between orientation and mechanical properties is observed.
- $\langle 100\rangle$ direction is the most resistant to transformation.
- Path of martensite transformation through microstructure dictates global response.

V. Austenite Plasticity in the Deformation of Superelastic Nitinol

Nitinol is a near-equiatomic intermetallic alloy of nickel and titanium that is widely used as a medical implant material as it can display reversible strains approaching ~10%. This is a result of an *in situ* phase transformation from its austenite to martensite phases that can occur when the alloy is loaded; this phenomenon results in the property of shape memory and more importantly superelasticity. The typical reversible deformation of superelastic Nitinol used in medical grade stents can be described by linear elastic loading of austenite phase followed by martensitic phase transformation which occurs along the "plateau" in the stress/strain curve, prior to linear elastic loading of the resultant martensite (Figure V.1). The transformation stress is generally taken to be more or less constant, which results in this plateau region [14]; on further loading, the resultant martensitic phase first elastically and then plastically deforms. The austenite phase is assumed to be involved in the transformation and elastic deformation only.

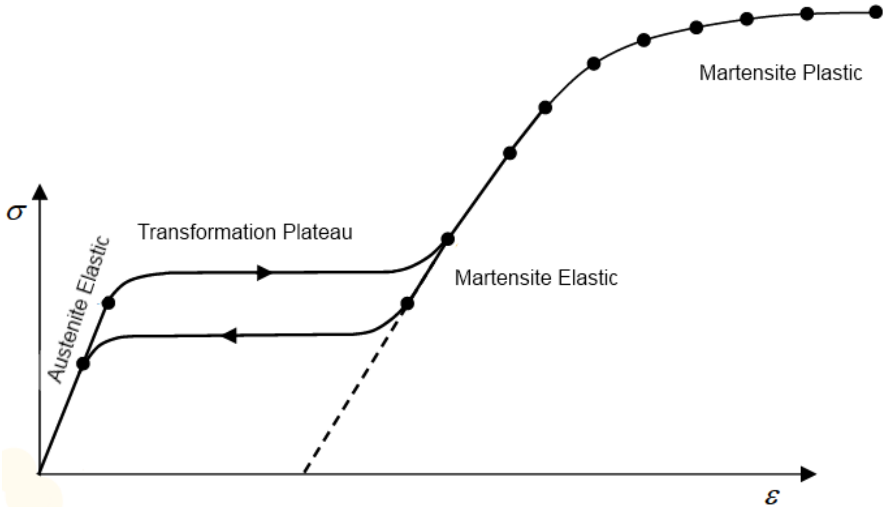

Figure V.1: An idealized stress-strain relationship for Nitinol showing loading and unloading transformation plateau as well as martensitic deformation regime.[10]

Theoretically, martensitic transformations rely on the twinning and reorientation of the martensite phase from austenite parent phase. Conventionally, it is assumed that 100% of austenite phase is transformed at the end of transformation plateau [93], implying that the austenitic phase will never experience any strain beyond the conventional elastic limit. Typically, the critical transformation strain required to form the martensitic phase is considered to be 1.2% [14]. As much larger deformation results from martensitic transformation, there have been few at-

---

[10] Modified from ABAQUS Nitinol UMAT manual.

tempts at understanding the role of plastic deformation in the austenite. It is this aspect of the deformation of Nitinol that we examine in this work.

V.i. Results and Discussion

Figure V.2 shows the displacement-stress graph of spiral (45°) samples; when compared to Figure VI.1, the idealized stress-strain curve fails to account for the sloped plateau as well as nonlinear relationship of martensite fraction with respect to strain along the transformation plateau. For these data, the tensile test was stopped just on the inflection point where the transformation plateau ends and martensitic elastic deformation begins. At this point, the martensite fraction is just slightly above 90%, contrary to the conventional notion that the sample should be fully martensitic at end of transformation plateau; clearly, a significant fraction of the sample still remain austenitic.

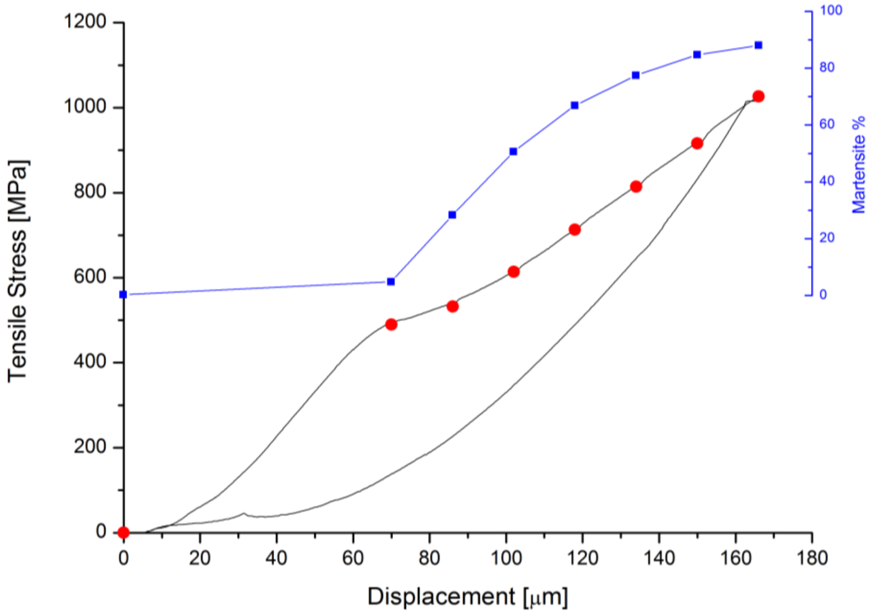

Figure V.2: The displacement-stress plot for the spiral sample (see Figure II.1). The blue plot near the top shows the martensite fraction as displacement increases. The dots on the curves represent where the micro-XRD scan was taken.

From the micro-XRD, a deviatoric strain tensor was obtained at each scan spot. This permits the analysis of the local strain distribution across the entire gauge section. The strain tensors were normalized using the von Mises criterion and analyzed using the OriginPro software (Figure V.3). It is found that as the displacement increases, the average local equivalent strain for austenite phase does not increase as strongly as the global displacement. The average equivalent strain of austenite phase flattens out instead of increasing with the displacement level. This indicates that, as expected, the major portion of the macroscopic strain is a result of martensitic transformation.

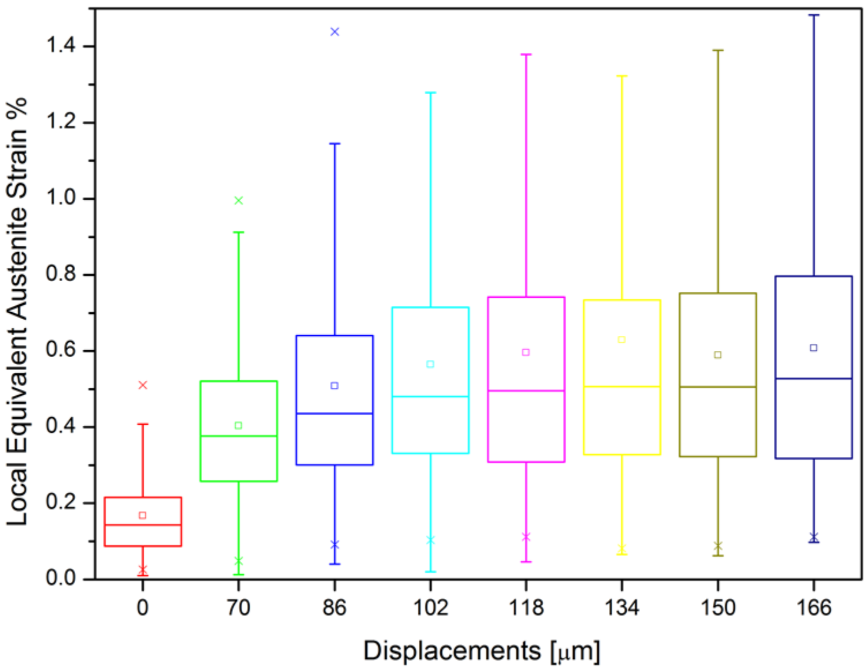

Figure V.3: A box-and-whisker plot showing the distribution of the local equivalent strain across the gauge section at increasing displacement levels. Note that since martensitic regions are not detected, these strains are from the remaining austenitic phase.

However, the strain distribution is unusual in that the upper bound of the strain increases dramatically, even though the box (which represents middle 50% of the data) is more or less constant. This implies that some austenite regions are increasing in strain. In fact, at a larger displacement (*i.e.*, from 102 μm and onwards), some austenite grains become over-strained to strain levels beyond the 1.2% strain required for transformation. This challenges the conventional assumption of critical 1.2% strain for the onset of the transformation from the austenite to martensite phase.

To better understand how some austenitic regions can exceed the critical transformation strain without forming martensite, a series of strain maps are plotted in Figure V.4. The local equivalent austenite strain is plotted along the gauge section at increasing displacement levels. Note that the white region is considered to be martensitic due to lack of beam resolution to analyze the diffraction patterns. This figure shows that even at the end of the transformation plateau, there are still some (~10%) austenite regions in the sample that did not transform yet experienced local strains in excess of 1.2%. The salient question is why these austenite regions were able to bypass the transformation and by so doing become overstrained. In this work, we examined this phenomenon during loading; however, due to time constraints, the unloading curve could not be sampled, and so the unloading effect of these overstrained regions cannot be evaluated.

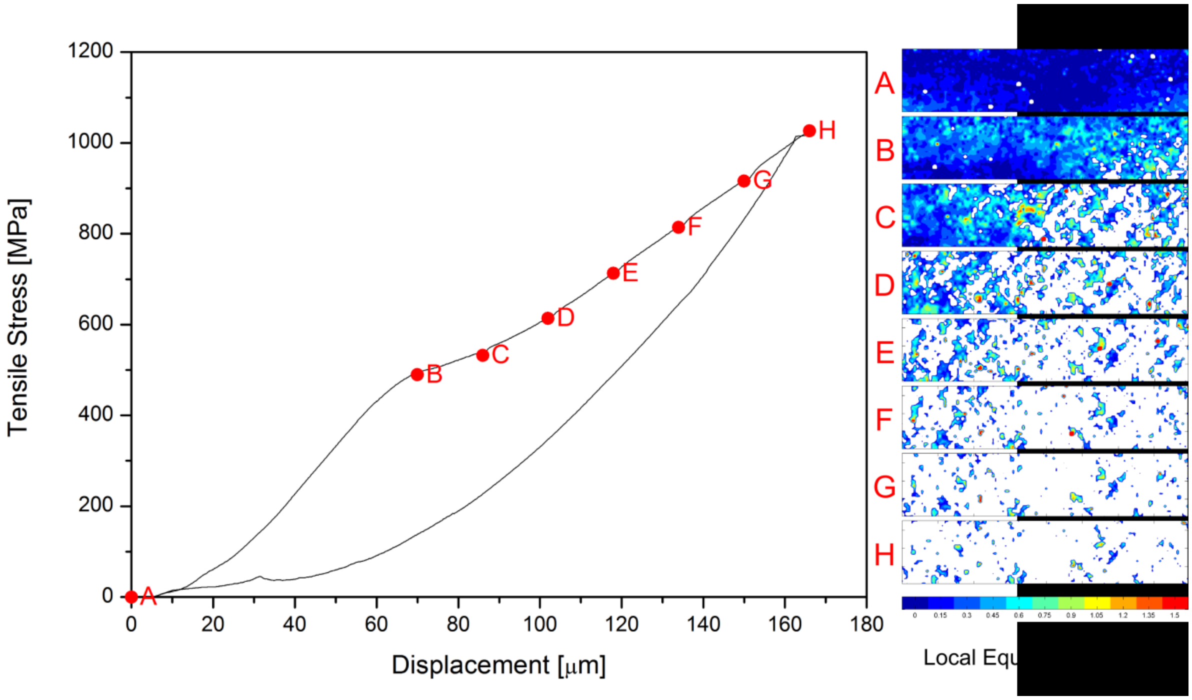

Figure V.4: A local equivalent strain map with corresponding displacement-strain curve for the spiral sample (see Figure II.1). Orange and red colored spots signify overstraining of $> 1.2\%$ equivalent strain and shades of blue shows the varying low level of local strain along the gauge section.

Figure V.5 shows accumulation maps for martensite as well as overly strained austenite maps. These maps were constructed by summing up the locations of martensite or overstrained austenite across the micro-XRD scans. They give a sense of time and direction of martensite growth and overstraining of austenite. Arrows point to the same location showing where the over-strained austenite region (red and orange colored) is almost never transformed into martensite (light blue to blue colored). This indicates that the over-strained austenite areas are able to remain austenitic at strains well beyond the typical transformation strain associated with austenite to martensite transformation. Given that these strains are relatively large and the micro-XRD can only measure deviatoric strain, it is likely that these austenitic regions are plastically deformed.

However, the observation of untransformed austenite has not been reported for Nitinol medical devices. To reconcile the difference between this micro-XRD study and actual implant devices, it is pertinent to compare the difference in the material and processing between the samples. One of the most significant differences is that to study the diffraction patterns from individual grains, it was necessary to fully anneal our samples to give a grain size of ~20 μm; in contrast, medical-grade Nitinol has a much finer grain size with subgrains on the order of nanometers [14].

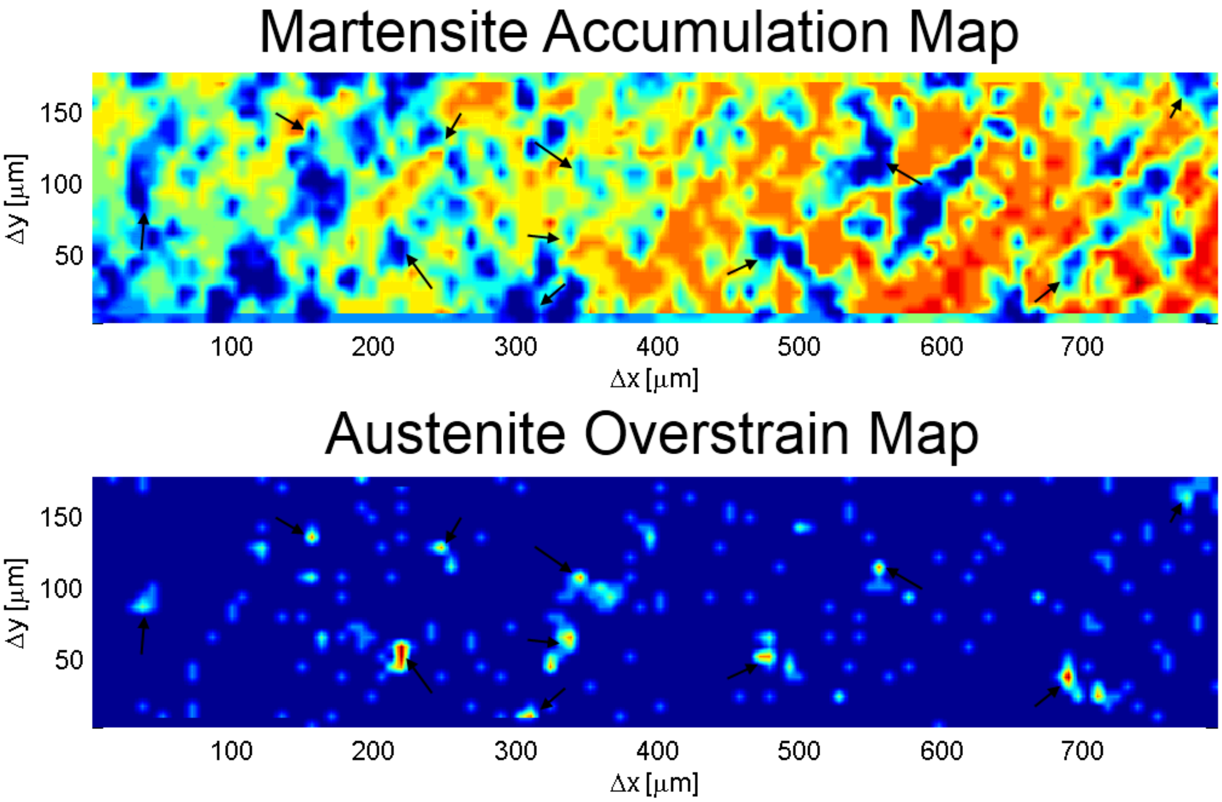
Martensite Accumulation Map

Austenite Overstrain Map

Figure V.5: Accumulation maps of martensite (upper), and austenite overstrain $> 1.2\%$ (lower). Red here signifies an "older" or earlier occurring event; blue signifies later or events that have yet to occur.

The relationship which best describes the dependence of grain size on yield strength, the Hall-Petch relationship, gives an inverse square root dependence of grain size on the strength. Although the yield stress is reduced with increasing grain size, the transformation stress is generally not a strong function of grain size [14]. These two grain-size dependencies are plotted schematically in Figure V.6; both incidentally would additionally show a dependence on texture. As the two curves cross, one can envision a small grain-size regime (the blue region) where the nanocrystalline grains require a higher stress to yield than to transform such that 100% transformation to martensite might be expected, and a coarser grain-size regime (the yellow region) where the possibility of plastic deformation, rather than transformation, of the austenite grains becomes a distinct possibility. Therefore, in some grains where the transformation stress is low, the austenite grain might be expected to be plastically deformed first.

It should be noted that the model representation in Figure V.6 only applies to specific areas on the samples because the transformation stress is highly dependent upon local texture and grain orientation. Consequently, not all grains will undergo plastic deformation, only ones that have higher transformation stress due to textural effects. The complex interplay between these two curves will dictate how the some regions of austenite phase will behave under imposed deformation. The plastically yielded austenite phase at this point may be unable to fully transform and result in "dead" region where it does not contribute to the reversibility of the superelastic deformation. Over time, these regions may accumulate and correspondingly may reduce the inherent superelastic range of the material; the resulting lower recoverable strains may well contribute to premature failures.

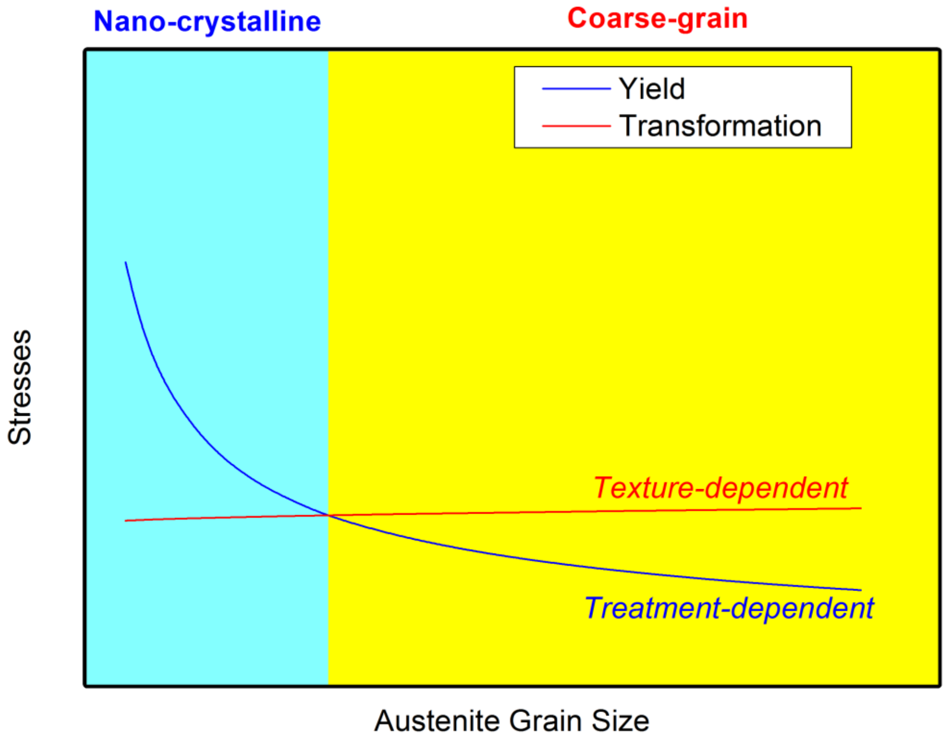

Figure V.6: Proposed model for the observed overstraining of austenitic regions in coarse-grained micro-XRD samples, as compared with behavior in medical-grade (nanocrystalline) Nitinol. This simple approach shows that as the grain size increases, the required stress to cause yielding decreases (*i.e.*, consistent with the Hall-Petch relationship), whereas the transformation stress has a much less dependence on the grain size. Whereas in the fine-grained regime (blue region), complete transformation of all austenite grains to martensite will likely occur, in the coarser-grain regime (yellow region) there is a distinct likelihood that specific austenite grains will become plastically deformed first.

VI. In-situ texture study of Shear loaded Nitinol

Most engineering materials are designed up to the limit of yielding, the point where the material begins to have unrecoverable deformation when loads are removed. Nitinol, an equiatomic alloy of nickel and titanium, through phase transformation, can sustain deformation that is nearly an order of magnitude higher than conventional engineering metals, such as steel. While the elastic recoverable deformation of Nitinol is identical with other metals, upon further loading, the parent phase, austenite, undergoes a diffusionless transformation to its daughter phase, martensite. Because the transformation is a coordinated movement of atoms, the microscopic rearrangements can lead to accommodation of much larger macroscopic deformations than conventional materials. Upon unloading, the martensite phase becomes unstable and will reverse transform back into the parent phase. It is this stress-induced transformation and its associated heat-induced memory effect of its original shape that endows Nitinol its two important properties, superelasticity and shape memory effect. Superelasticity is used by biomedical implant devices such as stents for improved mechanical performance. In this study superelastic Nitinol similar to the implant devices are used.

Because phase transformation that involves coordinated atomic arrangements, any large scale pre-existing orientation of the crystal structure with respect to the applied load will invariably affect the transformation. This has been many studies in how the single crystalline Nitinol transformation behaviors changes with respect to crystallographic directions [61, 94]. These results have been generalized to Modified Taylor Factor (MTF) (Appendix C) for polycrystalline Nitinol materials. Invariably the thermomechanical manufacturing process of Nitinol can impart a dominant orientation on these polycrystals [30, 47]. The emergency of large scale orientation on the granular level is often referred to as texture. In Chapter IV, the different orientation of dogbone samples from a tubular Nitinol stock were found to have drastically different tensile stress-strain behaviors. It is clear given exactly same thermomechanical heat treatment and identical composition, only the relative texture orientation change with respect to loading can explain the changes in bulk mechanical response.

In Chapter III, the unique response of Nitinol to tensile and shear deformation is explored. Previously studies have been conducted on flatted tubes which show similar difference in behavior between shear and tensile performance of Nitinol [30]. While Chapter III offers a rudimentary macroscopic measurement based approach to lifetime prediction of multi-mode fatigue in Nitinol, nonetheless the exact constitutive law that governs the mechanical behavior of Nitinol in both tensile and shear remains elusive. Given that identical thermomechanical processing and composition, different modes of loading obviously leads to different mechanical response. This non-isotropic behavior renders any numerical simulation that disregards such effect ineffective in predicting stress which in turns failure to predict life. At the time of writing, there has been no extensive microscopic characterization of Nitinol under direct shear loading. Thus this experiment will represent a first step at attempting to answer the key question, how does a material anticipate different modes of loading and react accordingly.

Shear loading test is typically conducted via torsional experiments. Given that torsion is a state of pure shear, it has lent itself well to many research experiments. However for most characterization techniques for texture studies, a flat plane is required. For symmetric reasons, torsional specimens tend to be tubular. The curved surface is different to analyze and error-prone even when attempted. Previous attempts [30, 80] at studying textures involved first loading the sample under torsion, then flattening out the specimen prior to texture study. This has many consequences such as inducing additional deformations that is unrelated to shear and the complications of mechanically flattening out surfaces. A state of pure shear could also be accomplished through the use of biaxial loading frames. Shearing load can be decomposed into two perpendicular equal tension and compression loads (at 45° away from the shear direction). Thus a biaxial rig that can induce equal tension and compression can generate a planar shearing load. However such rigs are complicated to design and expensive to obtain. Furthermore, for *in situ* studies, weight and space constraints may completely rule out the usage of such biaxial rigs.

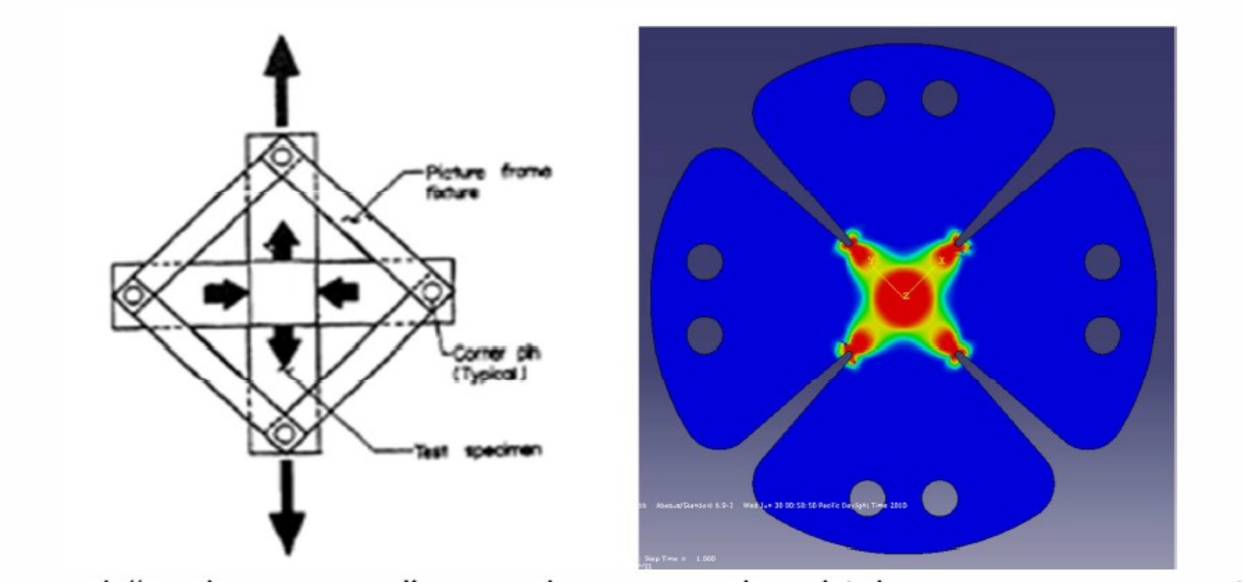

Figure VI.1: Left schematic of the cross-arm with sample in the middle [95], right, FEA contour result showing the planar shear of conventional material. Red is magnitude of shear, the center portion of gauge section suggests cruciform loading can indeed induce uniform planar shear.

In this study, we devised a novel design that makes use of the biaxial loading to generate pure shear without the use of biaxial rigs (Figure VI.1). A cruciform shaped sample is used to ensure symmetry in the two axes. However the compressive loading is accomplished through the use of cross-arm members that link up the perpendicular axis. Upon elongation of the tensile axes, the cross-arm being made from hardened steel would contract perpendicularly. This would naturally induce a compressive load that is equal to the tensile load initially. This allows the generation of pure shear through the use of a single axis, which means that it is easily adaptable to any uniaxial load frames. The added weight and space from the cruciform sample and cross-arms can be easily designed to fit into almost any space and weight constraints. The author can envision this to be a standard technique in future texture studies which can further bring new ways to examine shear in many types of materials.

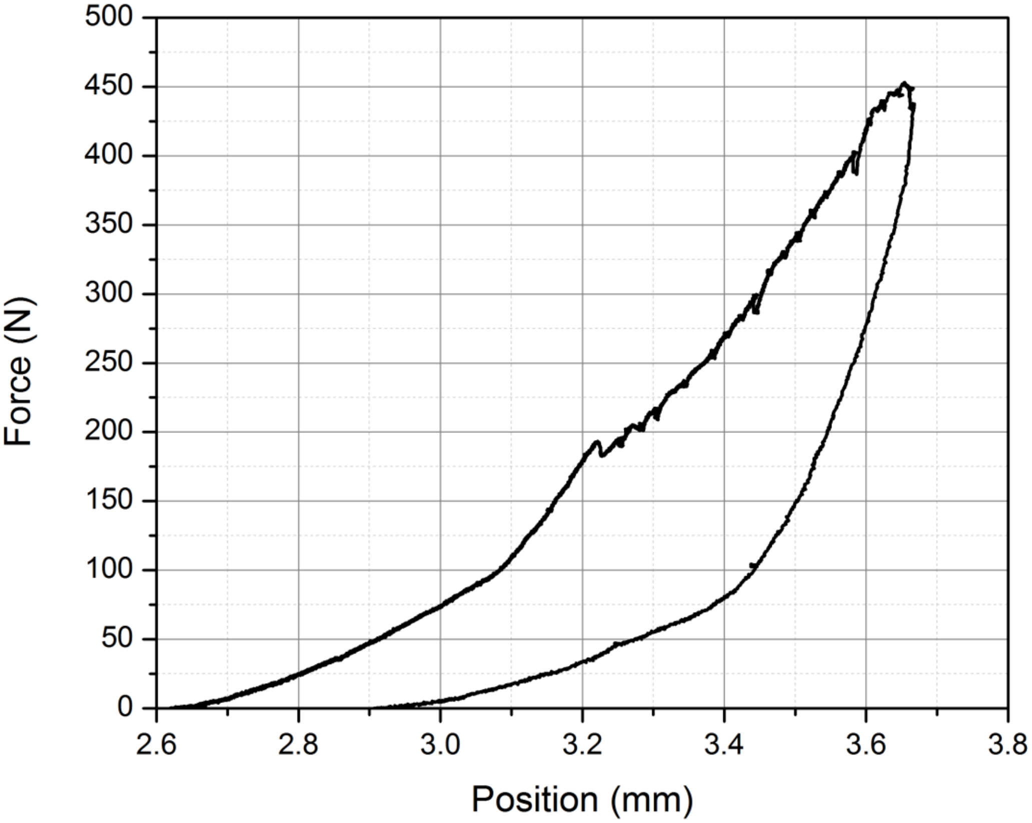

Figure VI.2: Force-displacement of the cruciform sample obtained during the experiment. Note the presence of rising plateau that is indicative of torsional or shear loading (compared to Figure III.1). The presence of two slopes on the elastic range is a result of machine slack and some asymmetry between the sample and machine.

VI.i. Characterization

Under shear, the sample symmetry is treated as monoclinic. This is because tensile axis is aligned along the RD axis, whereas the compressive axis is aligned to the TD. The sample symmetry accounts both for the shape of the sample as well as the loading configuration, and is used to simplify the visualization of Pole Figures (PF). This is in contrast to the crystal symmetry, which is based solely on the crystallographic symmetry of the sample. For this analysis, the austenite phase will be assumed to be cubic. Martensitic symmetry is monoclinic. However due to limitations of the X-ray beam, it is not possible currently to completely characterize the Martensite phase. The lack of data will shows up as white spots on the spatial map.

Analysis of the collected synchrotron micro-XRD is performed on XMAS (software package by Nobumichi Tamura) on a computing cluster. XMAS analyzes and computes a lattice orientation that fits the diffraction pattern off of the analysis spot. The subsequent lattice orientations are loaded into MTEX [96] in MATLAB as a pseudo–EBSD file through custom written script. All analysis and graphic are obtained through MTEX routines.

Texture of the sheet (Figure VI.4) shows a very strong preference for $(111) \parallel ND$. This is typically known as γ fiber (See Appendix D). To a lesser extent, there are some $(110) \parallel RD$ (α-fiber) and $(110) \parallel TD$ (ε-fiber). These textures are common in rolled BCC-type materials. It should be repeated again that the pole figure shown in Figure VI.4 is only the austenite phase. This is because after transformation, martensite phase forms nanoscale lathes that causes peak broadening in the diffraction spots. This is very difficult for the analysis algorithm to deconvolute, and thus will be discarded for the purpose of the analysis. Note that this texture has been characterized by Robertson before [30, 80]. The pole figure obtained here is identical with their results with the notable difference of rotation of 45° about the ND (due to sample orientation with respect to the X-ray beam).

From the Figure VI.4, there are several shifts in the pole figures as load increases and more austenite phases transform into martensite (and removed from the pole figure). Most noticeable is the strengthening of the γ-fiber, where the $(111) \parallel ND$ noticeably became much more intensive (darker shades of red). This can be inferred that γ-fiber is not conductive to shear induced transformation of martensite. Beyond the relative intensities changes, there does not appear to be major rotation of the poles. This is to be expected as the bulk of the microscopic strain should be accommodated by the transformation as opposed to reorientation of austenite phase (typically involves plasticity). However the change in distribution of the poles does suggest some preferential texture that are not conductive to transformation.

MTEX software package allows for computation of Orientation Density Function (ODF) [97], which contains all of the texture information in a three-dimensional object (Appendix D). By using sectional plots, it is possible to display ODF and see some characteristics of the distribution of orientations. In Figure VI.3, the ODF for the initial texture of cruciform sample is shown. The sections are at constant φ_2, which is an ideal way to display texture for BCC-type materials. In the $\varphi_2 = 45°$ plot, the contours near $\phi_1 = 54.7°$ confirms the presence of strong γ-fiber. There are partial fibers such as α-fiber and ε-fiber, however it is much weaker and not easily visible in the ODF plot.

With the ODF computed for each loading, it is possible to do quantitative calculations on the texture. One of metric used to measure the texture is the texture index (Appendix D). It measures the sharpness of the texture by effectively computing the root-mean-square of the texture ODF. Thus an idealized perfectly uniform texture would have texture index of 1, whereas sharper textures would have higher values.

Table VI-1: Texture Index of the remaining austenite phase of cruciform sample at different loads. Note the increase in the index as load increases.

Load	0N	200N	213N
Texture Index	4.0034	4.2198	4.2208

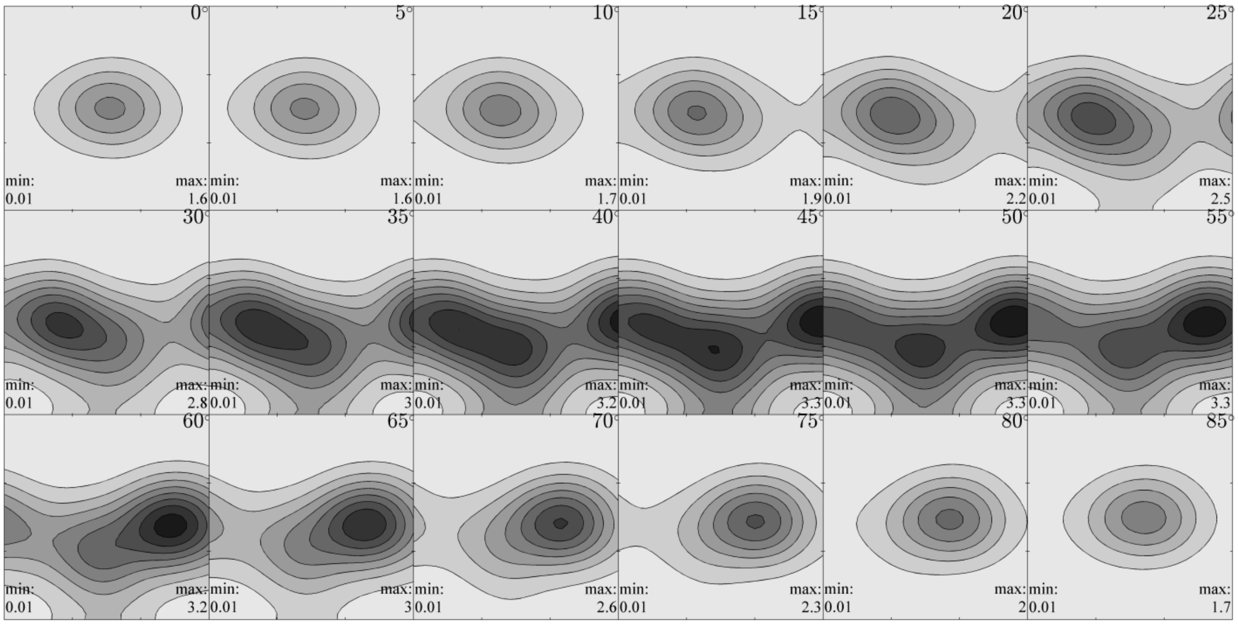

Figure VI.3: ODF sectional plot of the initial austenite texture of the cruciform sample. The subplots are at constant ϕ_2 section, the abscissa is Φ and ordinate is ϕ_1 axis. Ranges of all coordinates are $0-90°$ due to cubic symmetry. Note the high density of orientations through the $\phi_1 = 54.7°$ in $\phi_2 = 45°$ plot, this is the γ-fiber.

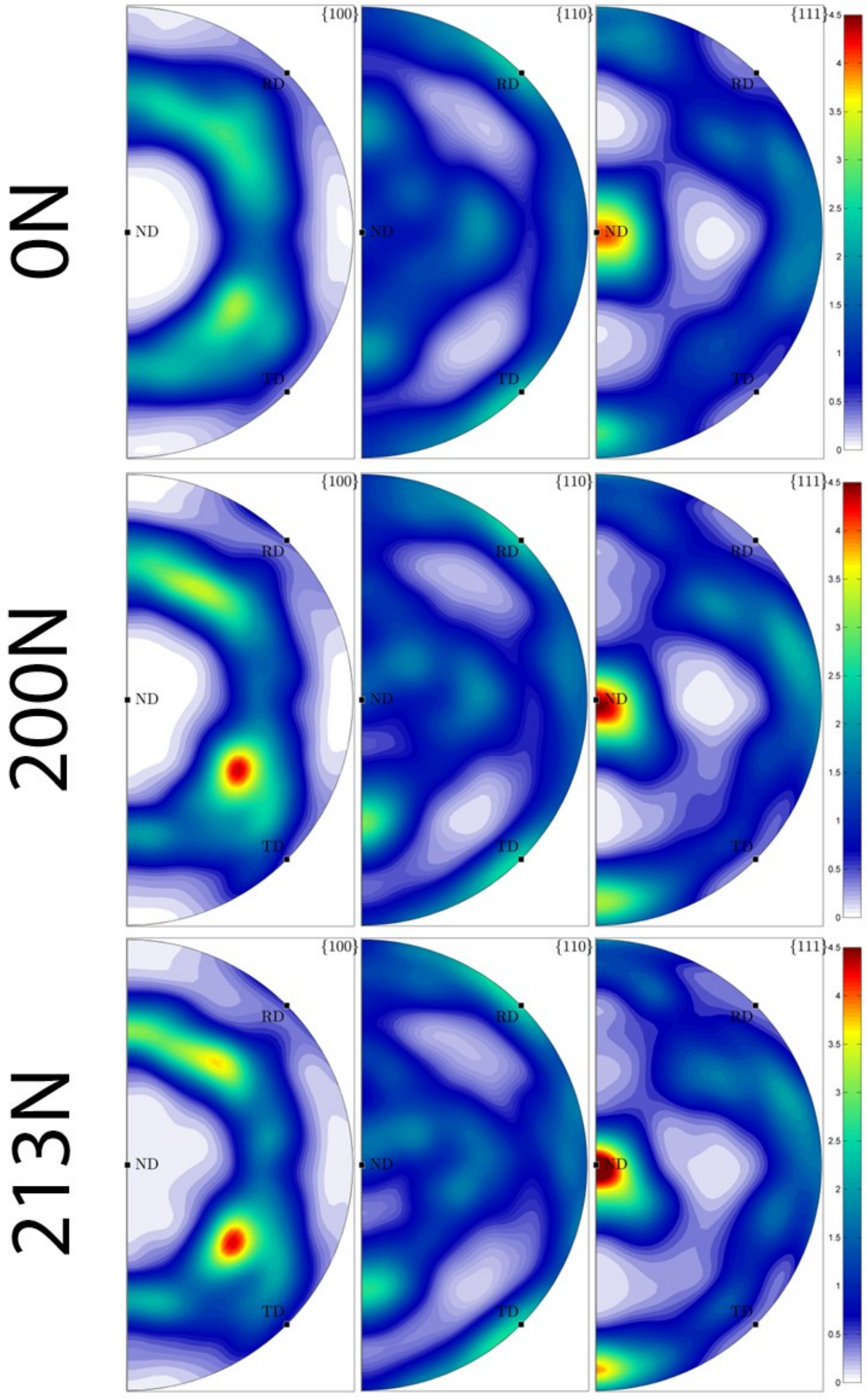

Figure VI.4: $\{100\}$, $\{110\}$ and $\{111\}$ Austenitic Pole figures showing the relative intensities of texture of cruciform sample at $0N$, $200N$, $213N$. The identical scales for all figures are shown on the right as reference. Note that RD and TD are $45°$ away from the abscissa and ordinate (sample X, Y axis). This is because the sample is physically mounted in such orientation with respect to the incoming beam. This means the shear direction coincides with the horizontal (X) as well as vertical (Y) axis. At $200N$, roughly 50% of gauge section has transformed. At $213N$, roughly 75% has transformed.

In Table VI-1, texture index for the three different loads are shown. There is a slight increase in the texture after the material has begun to transform at $200N$. It shows that the texture is strengthening as loading increases. This is not unexpected given that the γ-fiber does not appear to be the preferred orientation for shear transformation but is already the dominate texture. This would mean the rest of the texture would transform first, thus leaving relatively more γ-fiber than before, the end result is that the texture strengthens.

Pole figure coordinates in real specimen space and allows for easy visualization of reorientation of grains due to deformation. Inverse pole figure (IPF) coordinates are in crystal space, and allows for visualization of crystallographic changes with respect to specimen directions. In Figure VI.5, the IPF for the initial texture as well as the final texture are shown. The lack of discernible difference suggests that transformation does not favor any special orientation along any one specimen directions. This is confirmed by looking at the XY subfigure, which is parallel to the RD, as well as the X, Y subfigures, which are parallel to the shear loading. In the Z subfigure, it can be seen that the γ-fiber is indeed very strong in the texture. There does appear to be strengthening from $0N$ Z-direction to $213N$ Z-direction, however it is not too easily visualized.

It can be inferred that the shear transformation for Nitinol does not appear to vary strongly with orientation. It does, however seem to dislike the $(111) \parallel ND$, γ-fiber texture. Upon closer exmaination, it can be determined that are also some strengthening of the $(111) \parallel RD$ and weakening of $(111) \parallel TD$, however the effect is quite small and is considered statistically insignficant.

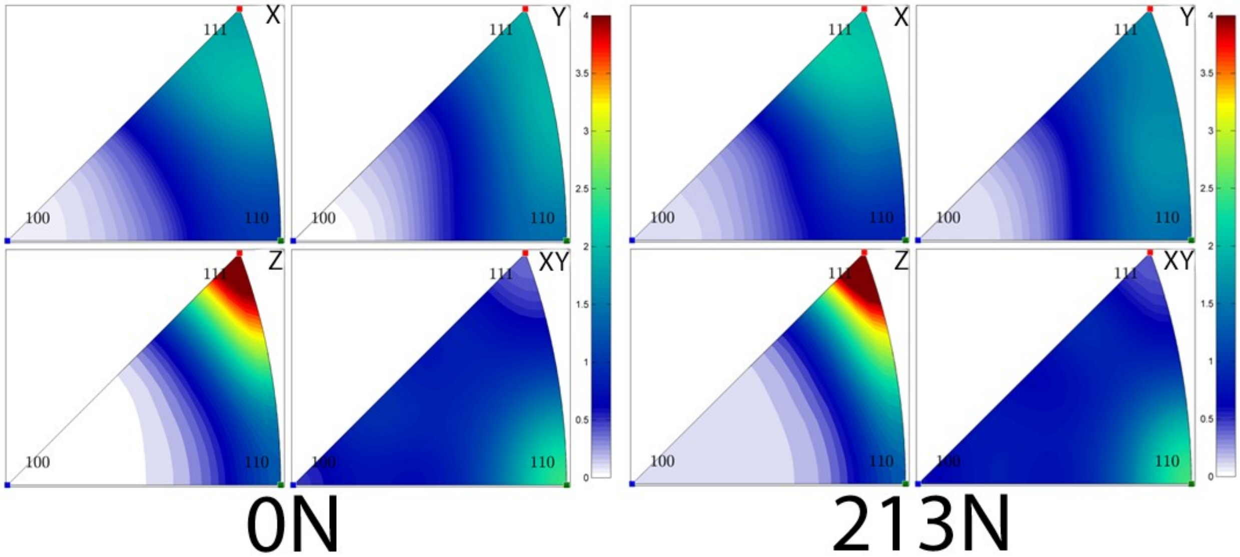

Figure VI.5: Inverse Pole Figures of the cruciform sample. X, Y, Z & XY (diagonal, parallel to RD) in sample space directions. 100 and 110 and 111 are the crystal directions (at the vertex of the IPF triangle). Note the color schemes are normalized between the $0N$ (initial) and $213N$ loading texture. The lack of visible change suggests a lack of significant crystallographic orientational influence on phase transformation.

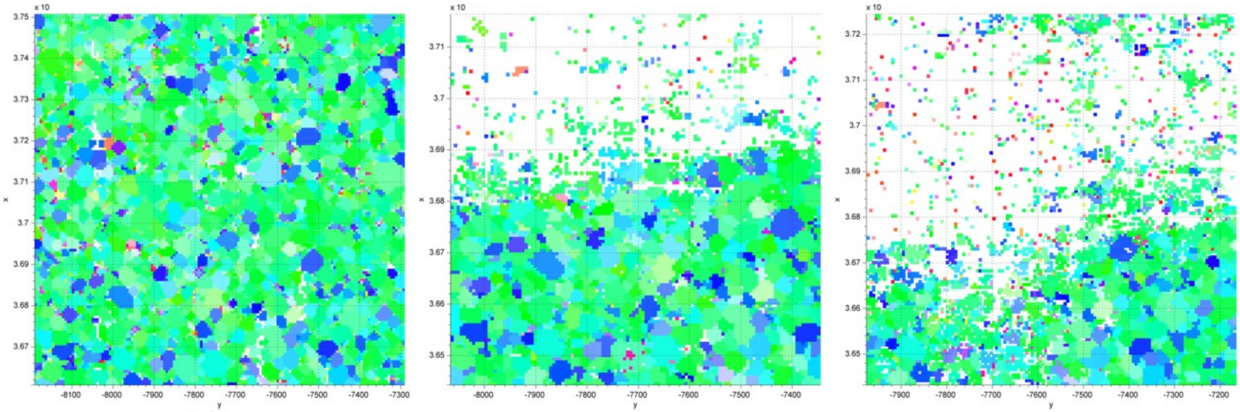

0N 200N 213N

Figure VI.6: Indexed spatial mapping of the ND (Z axis) of the cruciform sample. Color coded according to miller index (See Appendix E). The green (111) grains tends to be remain well behind of the Lüders bands (white), which correlates well with observation from ODF, PF and IPF.

The advantage of μXRD over traditional texture characterization techniques such as plain XRD is that it allows for spatial mapping of the grains. In Figure VI.6, the spatial map of cruciform sample that is color coded to miller index along the ND is shown. In this view, the γ-fiber shows up as green. Recall that lack of resolution prevents indexation of martensite phase, which shows up as white in the plot. It can be seen that the γ-fibers appears to have a tendency to remain behind the Lüders bands. This is reflective of the strengthening of the texture when considering γ-fiber was already the dominant texture initially. The $(111) \parallel ND$ fiber appears to be very strong in the initial texture (green in Figure VI.6). Upon loading, it appears that transformation zone more-or-less consume all texture without regard for any orientational preferences. Closer examination shows that there are plenty of $(111) \parallel ND$ left in the transformed zone. These residual austenite grain are precluded from transformation which indicates that it is precluded from transformation to martensite phase. There are also some $(100) \parallel ND$ grains that remain behind Lüders bands however the area is minimal as it does not show up on PF or IPF observations.

However because spatial mapping colorcoding requires a predefined specimen direction, one single map cannot represent completely the texture, thus in Figure VI.7, an alternative direction of X axis is chosen. In this direction, the lack of pattern in the grains that remain behind the Lüders Band shows lack of preference for alternative orientations other than the γ-fiber for the transformation hindrance. The texture is also much more varied, and so is the residual austenite phase as well. There does not appear to be a strong preference in any particular orientional effects as seen before. Similarly checking orientation mapping in other direction (RD, TD, 45°) failed to find any significant orientational behaviors.

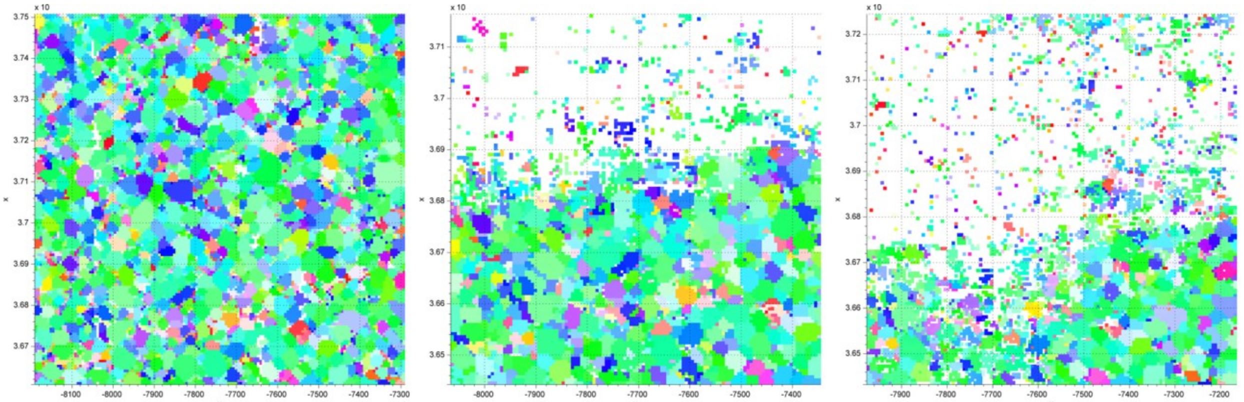

0N 200N 213N

Figure VI.7: Indexed spatial mapping of the X axis of the cruciform sample. Color coded according to miller index (See Appendix E). There does not appear to be a very strong pattern of orientation in the remaining grains behind the Lüders Band, this implies γ-fibers is indeed the main texture that shows some preference for not transformating.

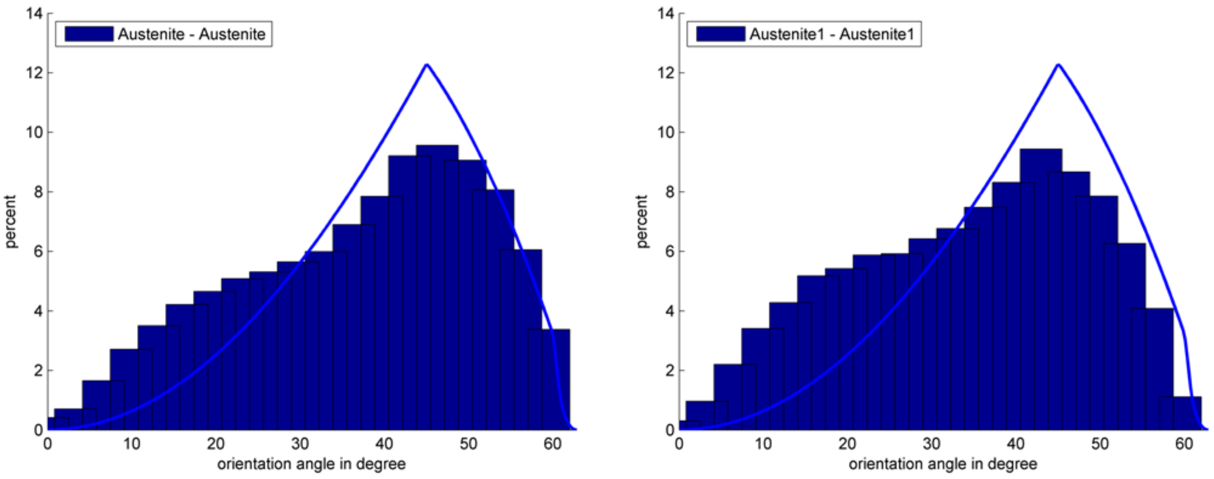

0N 213N

Figure VI.8: Correlated grain boundary misorientation angle distribution of initial texture and final texture of cruciform sample. Superimposed blue line is the idealized random distribution of cubic material. Note the reduction in high angle grain boundaries and the increase in low angle grain boundaries.

With the spatial mapping and orientation indexation capabilities of μXRD, it is possible to perform more advanced characterizations. After computation of the ODF, it is possible to derive a Misorientation Density Function (MDF) from the sptial information combined with the ODF. Correlated (between neighboring grains) misorietation angle and axis distribution can be obtained through the MDF [96, 97]. In Figure V.6, grain boundary misorientation analysis shows initial texture has a predominance of lower grain boundary angle than uniform random texture (blue line). Upon loading, a decrease of higher angle grain boundary is observed. Thus as the texture sharpens upon loading, the non γ-fiber texture begins to transform and become martensite. This means a reduction of high-angle grain boundary (non γ-fiber textures are more like to be at higher angle with respect to γ-fibers, than between γ-fibers).

The grain boundary analysis reveals another detail behind the γ-fiber transformation hindrance. It is possible that the predominate texture will always be the least favored to transform. This is due to the grain boundary transformation, where high-angle grain-boundary with its higher free energy decreases the activation energy for transformation. This causes transformation to occur more frequently on the high-angle grain-boundaries. The transformation can then consume the grain or propagate further via the high-angle grain-boundary. This dynamic between the competiting process of orientation effect and grain-boundary effect drastically complicates the martensiti transformation process of superelastic Nitinol. In the cruciform sample, it does appear that the high-angle grain-boundary propagation of transformation is more dominant and tends to prevent γ-fiber grains from transformastion. In effect, the grain-boundaries have shielded the cluster of γ-fiber grains from transformation, thus giving appearance of γ -fiber as is orientationally unfavorable for martensitic phase transformation.

VI.ii. Conclusions

Fundamental characterization of stress induced phase transformation in Nitinol is important to gain understanding of its constitutive law which may help improve fatigue life and design of future devices. Due to the nature of transformation, arrangement of atomic orientation influences both microscopic transformation properties as well as bulk properties. Advanced characterization of *in situ* tensile experiments has been performed on Nitinol before, however shear experiment has never been done. Texture analysis of *in situ* shear loading is difficult due to the typical shape of torsional samples. This poses numerous problems for planar geometry required by numerous analyses. Other solutions such as biaxial loading are generally too complicated and costly for typical experiment. Here, this experiment demonstrated an ingenious solution by using cross-arm that link up a cruciform sample that induces biaxial conditions of shear from a single uniaxial loading rig. Nitinol sheet sample is then loaded *in situ* under shear. Texture evolution suggests that dominant texture does not play a major role in the transformation from austenite to martensite. The observation of decrease in the high-angle grain-boundary suggests that there are two competing processes for transformation propagation, grain boundary and grain orientation. In *in situ* shear loading of cruciform sample, it appears that the texture sharpens as the dominant γ-fiber is precluded from transformation due to tendency for transformation to propagate via high-angle grain-boundaries.

VII. Texture study of In-situ fatigue loading

Given the prominence of Nitinol biomedical devices that are commercially available and actually implanted into patients, there is an urgent need to understand not only the constitutive behavior of Nitinol alloy in monotonic mechanical loadings but also fatigue or cyclic behaviors [43, 94, 98]. As seen in earlier chapters (Chapter III), the *in vivo* loading configuration experienced by stents is complex and often time multiaxial. However due to the complexity to properly analyze and quantify multiaxial fatigue loading, it is much more effective to first parse down and then analyze the behavior of multimode fatigue loading in superelastic Nitinol. By understanding how each individual mode contributes to the overall fatigue lifetime, it paves a way forward to towards the understanding of combined multiaxial fatigue loading lifetime prediction in Nitinol. From earlier chapters (Chapter III) it is obvious that shear or torsional loading in single loading stress-strain curves appear different than uniaxial tension loading. Fatigue loading in torsion has is then analyzed using classical mechanics of S/N approach in Chapter III, and it was found that the equivalent transformation strain is a much better life prediction parameter than shear strain. Tensile fatigue has been studied extensively in literature [60, 67, 68] and in Chapter, it has been determined that these two modes of fatigue loading can be normalized by using equivalent transformation strain. However by treating fatigue as a black box via S/N approach only empirical relationships can be gained but not fundamental understanding of mechanism behind the fatigue behaviors. In this study, the μXRD characterization technique from previous chapter is used to continue the austenitic texture analysis of *in situ* deformation of Nitinol samples. Instead of applied monotonic loading, cyclic loading is applied to the sample to simulate fatigue. Given that it is observed that cyclic loading in Nitinol causes some function fatigue that reduces superelastic performance, it is imperative to understand the exact mechanism behind this effect to better the prediction of lifetime. By observing the changes to austenitic texture, the standard assumptions that the SIM phase transformation is nearly completely reversible can be verified. Furthermore, changes due to functional fatigue can be matched up against changes in the austenitic texture.

VII.i. Uniaxial tensile fatigue in superelastic Nitinol wires

Fatigue test performed *in situ* under X-ray microdiffraction similar to setup in Chapter V and VI. Initial texture scan shows a very similar texture as seen by Robertson [30, 80]. There is a dominate fiber of $\langle 111 \rangle \parallel DD$ (Drawing Direction, along the long axis of the wire) (Figure VII.1). For comparison, an idealized pole figure of only $\langle 111 \rangle \parallel DD$ is shown in the same figure. By using the Modified Taylor Factor (MTF) for predicting uniaxial tensile behaviors (Appendix C), it is known that the (111) orientation tends to be the "easy" direction with largest transformation strain as well as lowest transformation stress. The existence of $\langle 111 \rangle \parallel DD$ fiber is not a surprise, given that $\langle 111 \rangle$ direction in BCC-like structure tends to be the close-pack direction. The drawing process results in reorientation of austenite grain structures such that the close-pack direction accommodates the drawing deformation. Thus the “easiness” of transformation may be a reflection of geometric accommodation of Nitinol grains as a response to the drawing process.

The initial loading of the wire can be seen in Figure VII.2. The material actually has negative transformation plateau slope, there are two reasons for such behaviors. One is unintended transformation of Nitinol in the grip, which lowers the load carried by the wire. The second is actually due to some small amount of recovery from the need to pause the loading periodically for calibration checks (appears as small discontinuity on the plateau). Since space constraints prevented installation of actual extensometer, it is not possible to analyze and quantity the actual stress-strain curve. This is not a problem given that μXRD can be used to characterize degree of transformation by measuring volume of material that actually transformed into martensite. The experiment will attempt to load the gauge section to near 100% transformation which may result in slightly distorted force-displacement plots (such as not returning completely to zero extension upon removal of load).

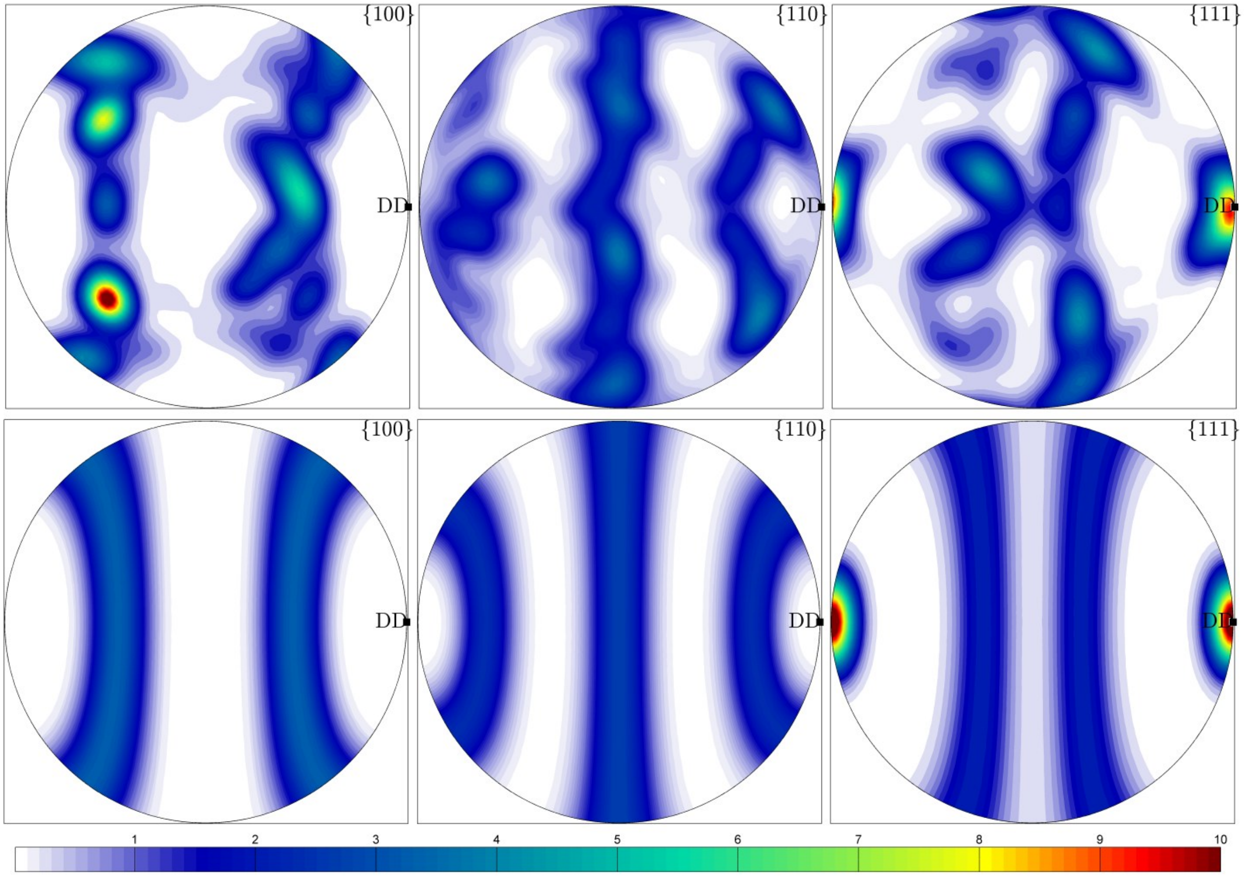

Figure VII.1: Initial texture of superelastic Nitinol wires (top), idealized $(111) \parallel DD$ pole figures as comparison (bottom), same scale used between the two plots.

The superelastic Nitinol wire is then cycled from fully austenitic (zero load) to near fully martensitic. Due to the slow motorspeed and restricted time, only 100 cycles were applied on the wire sample. However, even after 100 cycles, there are notable changes to the force-displacement curves between the initial cycle and the last (100th) cycle (Figure VII.2). The hysteresis loop area has significantly decreased. There is also an increase in the force needed to bring the wire back into the near fully transformed state. This could be due to accumulation of permanent transformed martensite as well as textural changes in austenite.

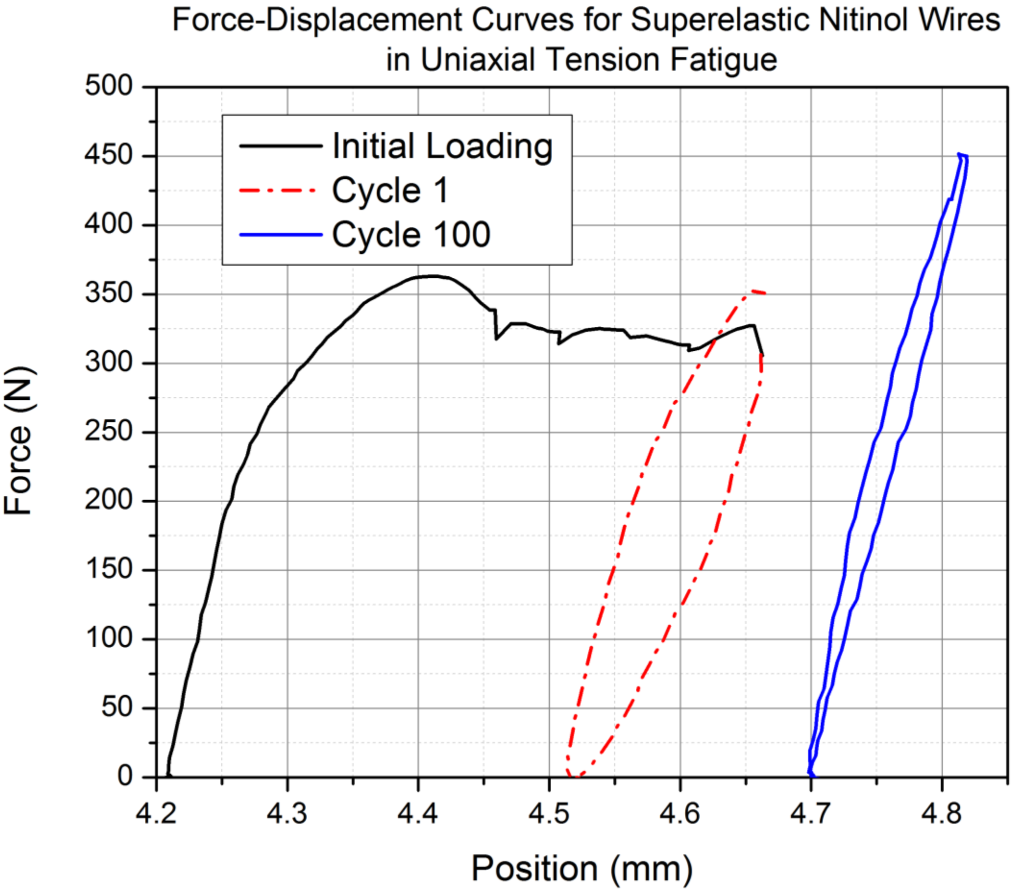

Figure VII.2: Force-displacement curves for initial loading of superelastic Nitinol wire (black), first cycle (red) and 100th cycle (blue). Note the decrease in the hysteresis loop areas as well as the increase in the force needed to bring the material back to fully transformed state.

After 100th cycle, the wire is then characterized completely in µXRD to determine its austenitic texture (Figure VII.3). By comparing against the initial texture, it can be seen that there is a rotation of the texture about the ND. This can be either slippage in the grips due to transformations or lattice rotations in the austenitic grains due to cyclic loading. The rotation is not large (< 5°), and due to the problematic slippage issues, a revised experiment will have to be devised to specifically address the possibility of lattice rotation separately.

The overall dominant texture appears to roughly be the same between the initial and final sate. In Table VII-1, the texture index suggests that the texture has become much sharper after the fatigue loading. To understand the influence of phase transformation on the texture, a separate unloaded (zero load, fully austenitic) and loaded (near fully martensitic) texture is obtained for the initial as well as the last (100th) cycle. The difference in texture index is mixed and the difference is much smaller in magnitude than difference between the fatigue loadings alone. Thus it can be concluded that fundamentally the texture change due to fatigue is not directly related to the monotonic SIM transformation.

Table VII-1: Texture index for the unloaded (zero load) and loaded (near fully transformed) condition at initial loading as well as 100th cycle.

Texture Index	Unloaded	Loaded
Cycle 0	7.3412	7.1354
Cycle 100	8.5877	8.8092

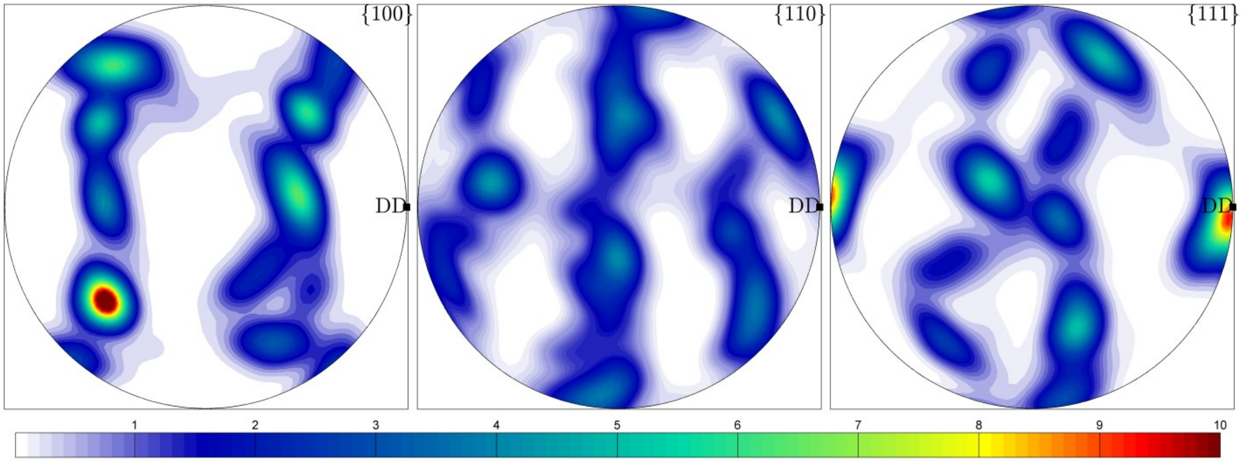

Figure VII.3: Austenitic texture of superelastic Nitinol wire after 100 cycles of loading from zero load to near fully transformed state.

From Chapter VI, it is found that grain-boundary misorientation angle distribution changes due to phase transformation may be a significant role in the texture evolution of superelastic Nitinol. Thus in Figure VII.4 the initial versus 100th cycle grain-boundary misorientation angle distribution is shown side-by-side. The most interesting result is the increase in amount of low-angle grain-boundaries, whereas the distribution of large-angle grain-boundaries do not appears to have significantly changed. Again, the blue line shows the idealized grain-boundary misorientation angle distribution for completely random cubic material.

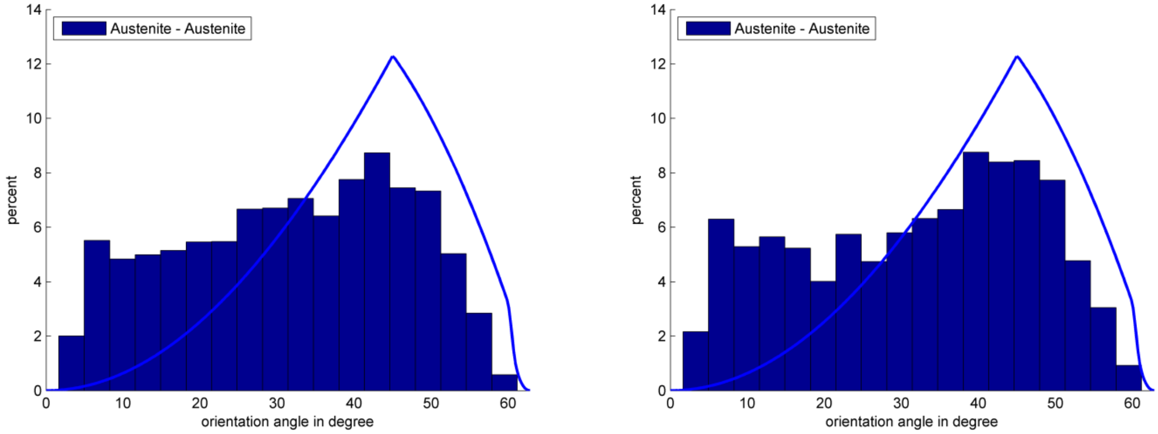

Figure VII.4: Correlated grain boundary misorientation angle distribution for initial texture (left), and after 100 cycles of uniaxial tensile loading (right) for superelastic Nitinol wire. Blue line shows idealized distribution of grain-boundary misorientation angle for cubic materials.

VII.ii. Fatigue of shear loaded Nitinol

In Chapter VI, the shearing loading of cruciform samples is discussed. The initial texture has been analyzed in Chapter VI and shown in Figure VI.4. However the texture is characterized again in this experiment to ensure consistency (Figure VII.5). Time constraints forced fatiguing to only 80 cycles of shear loadings. Even with such limited loading, the force-displacement curves still show significant reduction in the hysteresis loops (Figure VII.6).

The texture change between the initial and final states appears to be strengthened. Thus in Table VII-2, texture index is computed for the initial and final states. Again, the similar increase in texture strength is seen again. This can be best seen in Figure VII.5 on the bottom (80th cycle) $\{100\}$ pole figure, where the ring-like structure has degraded and sharpened (shaded in red) when compared to the top (initial) pole figure. Given the predominance of $(111) \parallel ND, \gamma$-fiber, it would appear that the texture sharpening is similar to the observations from Chapter VI, where γ-fiber is precluded from transformation due to grain-boundary interactions overwhelming the orientation effects on transformation.

To confirm the grain-boundary interactions, in Figure VII.7, the correlated grain-boundary misorientation angle distribution is shown for both the initial and final states. There does appear to be very slight increase in low-angle grain-boundary, however overall the distribution is similar. Shear fatigue appears to be less significantly impacting the high-angle grain-boundaries. This appears to show that fatigue texture sharpening acts differently than monotonic SIM transformation. It would appear that shear fatigue loading of superelastic Nitinol sample is not strongly influenced by grain-boundary misorientation angle. However the texture sharpening is still occurring, which implies that non-dominant texture is still being reduced. This can occur if the non-dominant texture failed to reverse transform and is permanently transformed into martensite. This is likely to happen if non-dominant texture were to bear more load than dominant texture, which is possible due to the “shielding” effect of grain-boundary misorientation effects.

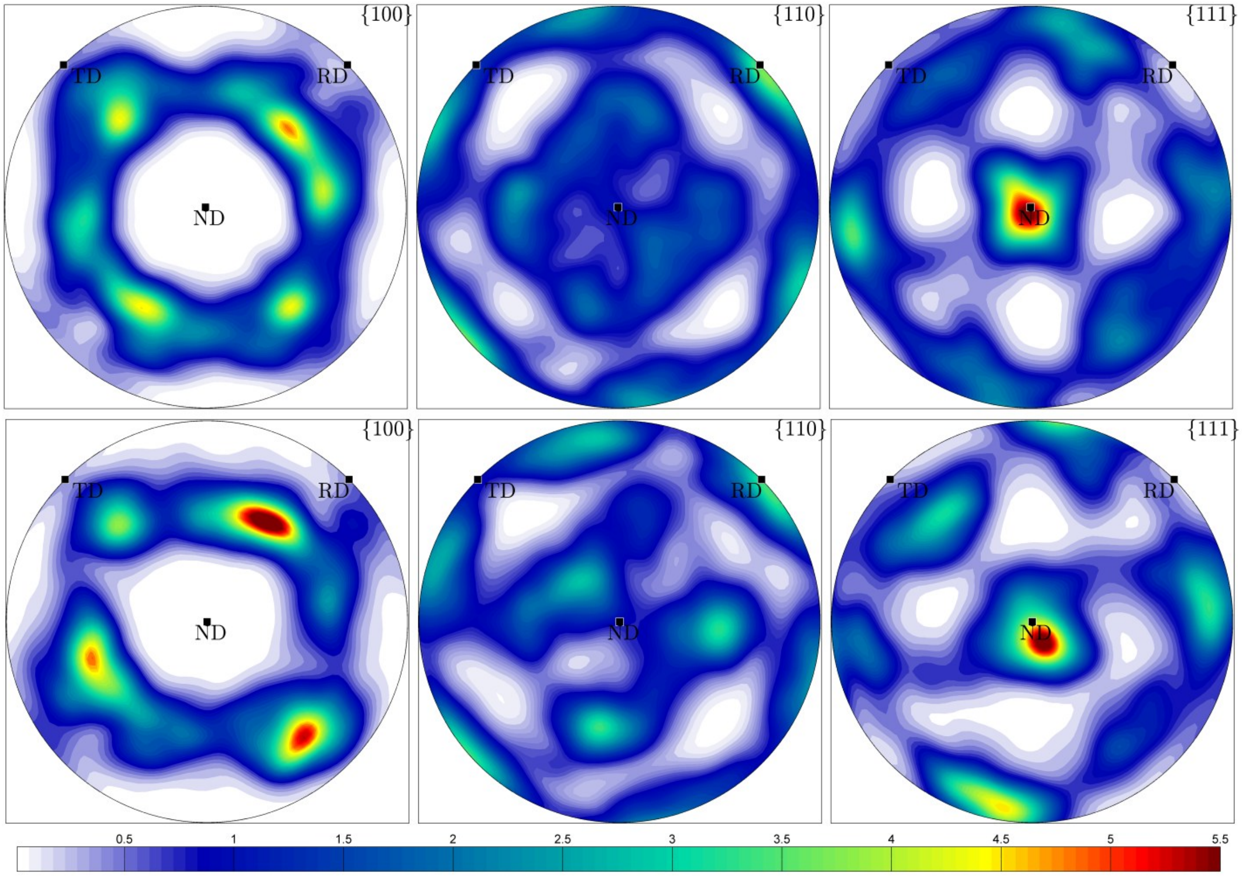

Figure VII.5: Texture changes for shear loaded superelastic cruciform Nitinol sample. Initial texture (top), 80th cycle (bottom). Three different pole figures are shown, as well special direction in sample space shown.

Table VII-2: Texture index for shear loaded superelastic cruciform Nitinol sample. Note the increase in texture index

State	Texture Index
Initial	3.9638
Cycle 80	4.7654

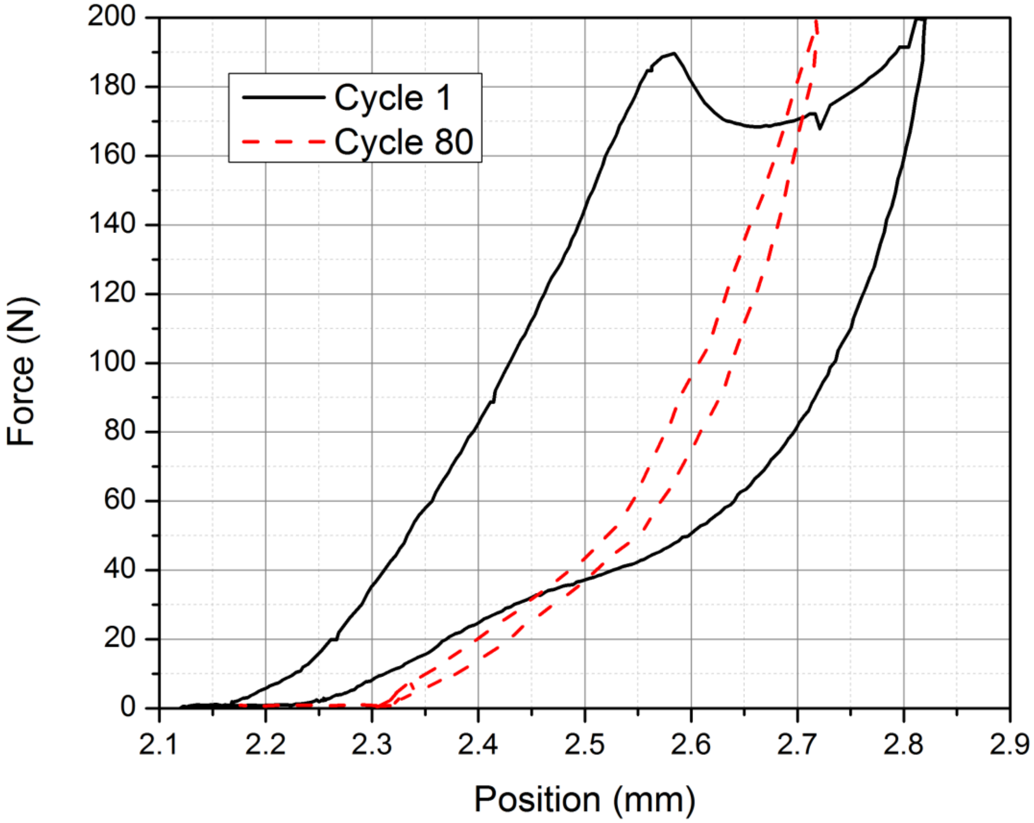

Figure VII.6: Initial versus 80th cycle force-displacement curve for shear loaded cruciform sample. Note the reduction in hysteresis loop as well as increase in the load to bring to the same near fully transformed state.

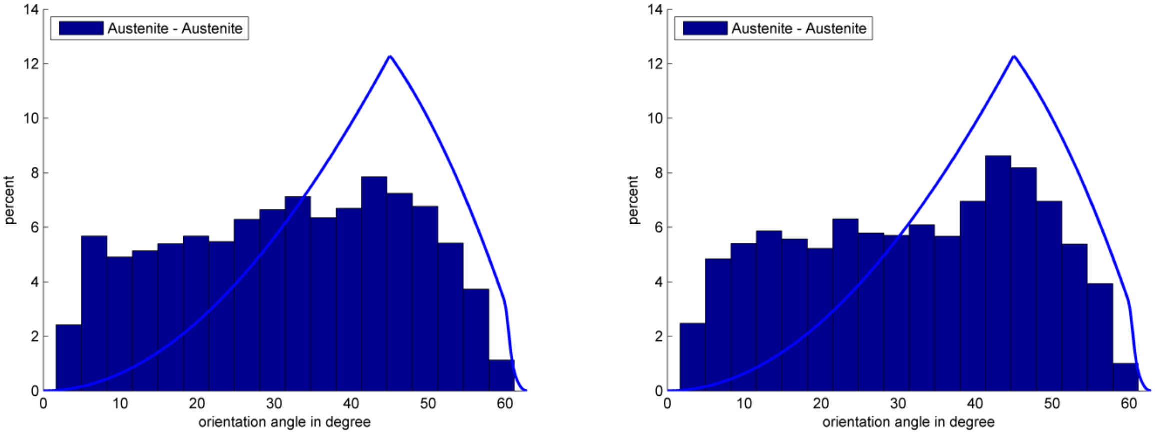

Figure VII.7: Grain boundary misorientation angle distribution for initial texture (left), after 80 cycles (right). Distribution difference is much more subtle, which suggest a different mechanism than monotonic SIM transformation.

VII.iii. Fatigue uniaxial tensile in superelastic dogbone Nitinol

For tensile loading, dogbone sample used in Chapter IV is ideal. Recall in Chapter IV, three types of samples were obtained from a flattened tube, 0°, 45° and 90°. However the flattened tube stock is not available, thus the same dogbone samples are made from the cross-rolled sheets used for cruciform samples used in Chapter V. Similarly, the same orientations are used, where the 0° is aligned parallel to the RD, and 90° parallel to TD. Due to time constraint, only one sample orientation can be fully tested in tensile fatigue. To make comparison with cruciform samples, it is decided to use the 45° dogbone, where the tensile axis is aligned parallel to the cruciform shear axis with respect to the texture. This can be seen in Figure VII.8, where the texture appears remarkably similar to Figure VII.5, albeit rotated about ND by 180° due to X-ray orientation to the sample.

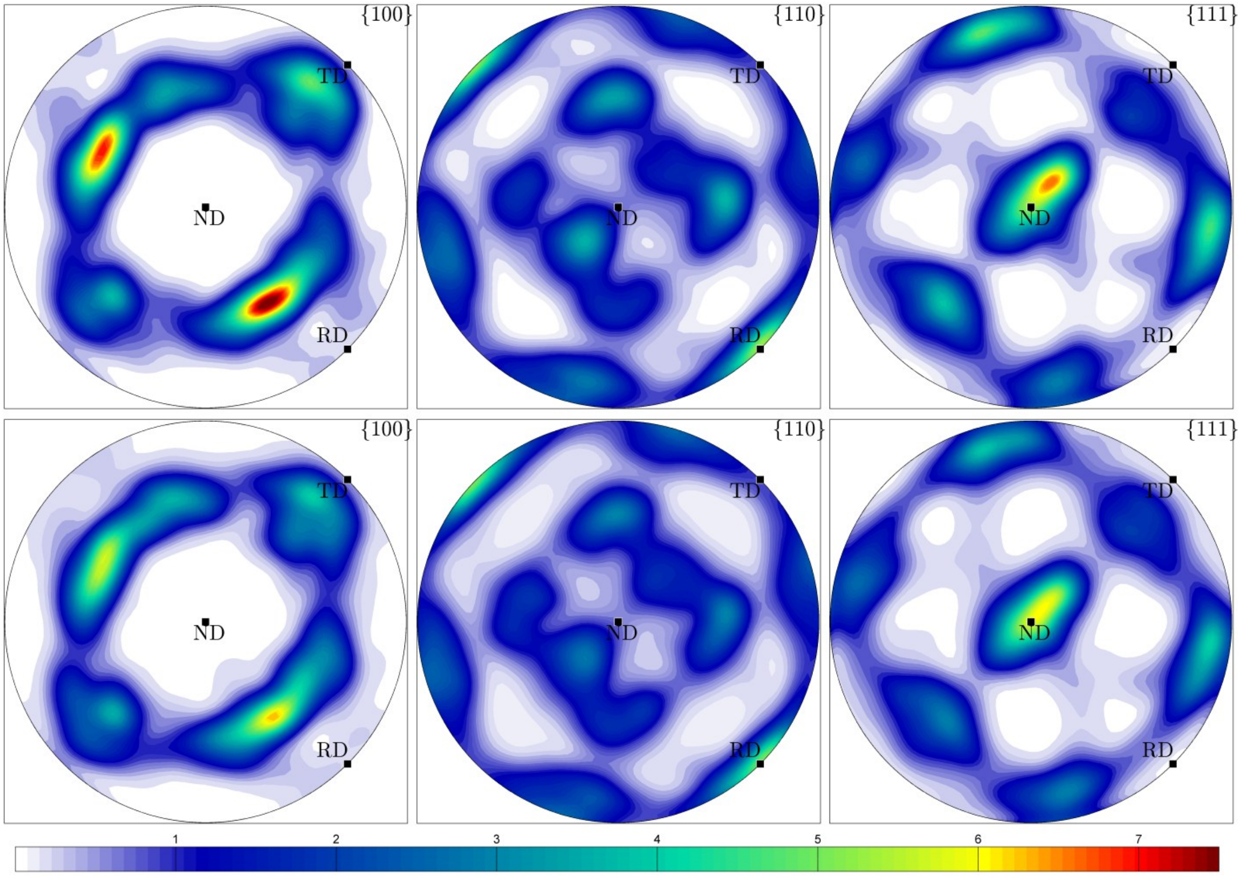

Figure VII.8: Initial texture versus 100th cycle texture for dogbone tensile fatigue.

The force-displacement curve is shown in Figure VII.9, note the flat transformation plateau, and compare this with Figure VII.6, where the transformation is sloped. This drastic difference in mechanical behavior even given the same material with same texture shows fundamentally texture alone cannot fully explain or predict the mechanical deformation behaviors. Similarly, after 100 cycles of loading from zero force to near fully transformed state results in much reduced hysteresis loop area. Increase in force needed to reach near fully transformed state is also increased, as seen in other sample forms.

Table VII-3: Texture index for shear loaded superelastic cruciform Nitinol sample. Note the increase in texture index

State	Texture Index
Initial	6.4763
Cycle 100	5.3474

From observing Figure VII.8, something different appears than previous samples, the texture actually appears to be weakened. This is confirmed through calculation of texture index in Table VII-3. This implies that under tensile fatigue, the dominant texture actually is consumed by the cyclic loading. This can be explained if the dominant texture transforms into martensite and failed to reverse transform. Thus if the dominant texture, $(111) \parallel ND$, or γ-fiber does indeed transform and fail to recover, then it would appear that grain-boundary misorientation is not a significant factor in the tensile loading. As such, in Figure VII.10, the grain boundary misorientation angle distribution is shown for both states, and not surprisingly, there is no significant difference in the distribution. This would suggest that for tensile fatigue, the orientation effects play a bigger role then shear, where misorientation angle is more important, in determining texture evolution.

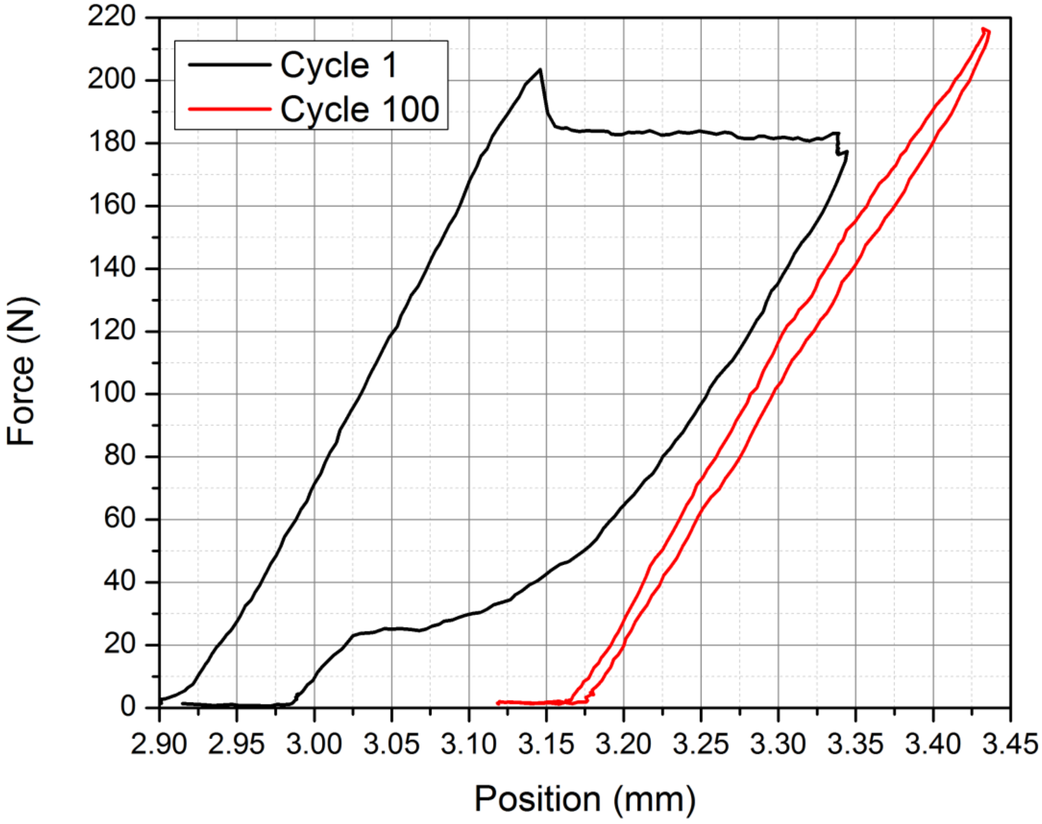

Figure VII.9: Force displacement curve for first cycle and the 100^{th} cycle.

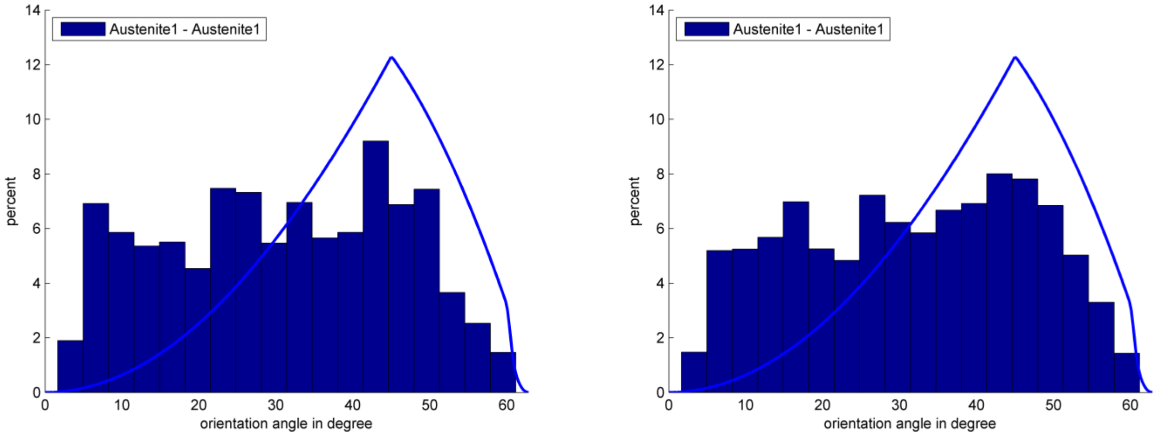

Figure VII.10: Grain boundary distribution for dogbone tensile fatigue, initial texture (left), after 100 cycles (right).

VII.iv. Small versus Large Grains Texture

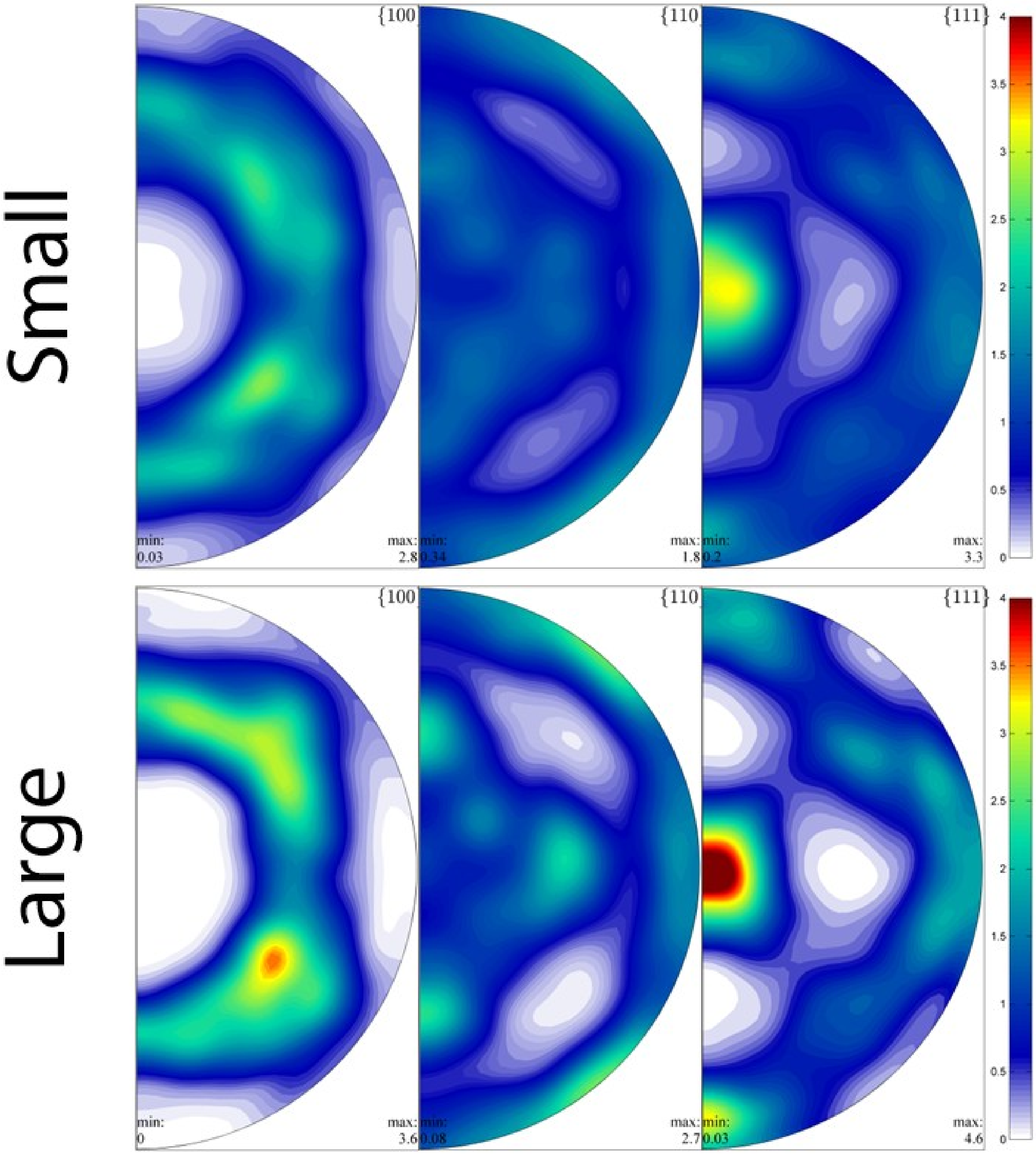

Figure VII.11: (Top) pole figures of small grains ($< 15\ \mu m$), (bottom) pole figures of larger grains ($\geq 15\ \mu m$). Note the much sharper texture observed in larger grains.

In addition to fatigue, the distribution of grain structure itself is investigated. This is conducted on the cross-rolled sheet used both for dogbone and cruciform samples. In Figure VII.11, the texture of smaller grains ($< 15\ \mu m$) is plotted against larger grains ($\geq 15\ \mu m$). It can be seen that the texture of larger grains is much stronger than smaller grains. The exact texture index is shown Table VII-4, where the difference is confirmed to be very large.

Table VII-4: Texture index measurement of small, large grains and whole sample for the cross-rolled superelastic Nitinol sheet.

Type	Small grains	Large grains	Entire Sample
Texture Index	2.7436	4.9400	4.0034

This observation has several consequences, since smaller grains generally are the precursor to the large grain during grain growth. Thus during annealing or recrystallization process, smaller grains are consumed by larger grains of a favorable orientation. This dominant orientation is probably chosen to accommodate residual strains from processing. This also means that texture cannot be fully removed from Nitinol due to its strong preference for grain growth towards strong texture. This is confirmed by Robertson and Pelton [47, 84].

Since grain growth strengthens texture, this implies the nanocrystalline material that is typical of actual biomedical implant material may actually have much weaker texture than samples studies in the experiments.

VII.v. Conclusions

The experiments performed in this chapter are mainly to observe the texture changes in different product forms of Nitinol as fatigue degrades the performance. It is found that fatigue degradation results in decreased hysteresis loop area, as well as increases the force needed to reach near 100% martensite phase. However the texture does not appear to be consistently changing to account for the decreased performance. The changes in texture in part may play a role in the functional fatigue of Nitinol, but the results are too conflicting to generalize. Going back to Chapter VI, where the competition between grain-boundary misorientation versus orientation effect on the transformation is discussed in context of shear deformation, it appears to play a similar role in fatigue degradation. The changes in texture due to fatigue of Nitinol as well as grain-boundary effects are summarized in the table below:

Sample & Loading	Texture Change with Fatigue	Grain Boundary Effects
Dogbone, Tensile	Weakens	Very small
Cruciform, Shear	Strengthens	Very small
Wire, Tensile	Strengthens	Large

VIII. Afterword

In this work, the fatigue behavior as well as texture influence of superelastic Nitinol has been explored extensively. It has been shown that when subjected to traditional mechanics treatments (Chapter III), the fatigue life prediction parameters can be the normalized (equivalent) strain. A slightly more accurate life prediction result can be gained by using the normalized transformation strain (Coffin-Manson). The S/N & modified Coffin-Manson approaches presented is a simple method that allows for rapid data collection and easy implementation in software simulation packages. While it is recognized that this is, at best, an empirical method that attempts to correlate lifetime versus various damage parameters (such as applied deformation), the method does reveal that the damage accumulation parameter is the transformation strain. This suggests that contrary to theoretical considerations, the phase transformation in superelastic Nitinol is not completely reversible. It implies that a certain amount of transformed grains never completely recover. The preclusion of reverse transformation appears to play a role in the function fatigue in superelastic Nitinol.

While the above macroscopic approaches to understanding and predicting fatigue in Nitinol is effective, it does not however elucidate the exact mechanism governing the performance degradation in Nitinol. A more fundamental understanding is needed, thus the rest of the text is devoted to understanding the microscopic transformation in fatigue with help of characterization power of synchrotron X-ray diffraction. The results from Chapter IV-VII provided much more insights into the phase transformation on a microscopic scale. In tension the transformation forms Lüders bands that is highly heterogeneous. Furthermore the end of transformation plateau does not signify the fully transformed martensitic state. The local orientation appears to influence tensile mechanical deformation behaviors such that it follows the Modified Taylor Factor (Appendix C). There are also observations that suggest the localized overstraining of austenite parent phase is possible. Monotonic tensile loading reveals that some localized austenite grains along non-preferential transformation orientations tend to sustain strains beyond the austenite transformation limit. This presents another way for the degradation of performance in superelastic Nitinol, where the plastically deformed austenite grains are precluded from transformation. When all the effects are combined, the complex deformation pathways distribute the loads inhomogeneously down to austenite phase, transformation strain, as well as the martensite phase. It stands to reason that that gross simplification such as continuum mechanics used by traditional FEA cannot simulate the mechanical behaviors of Nitinol completely. However, even a simple modification to continuum mechanics such as Modified Taylor Factor appears to correct some of the shortcomings by accounting for orientational effects (Appendix C). This method is successful in predicting the relative transformation stress, as well as shape of and total recoverable strain of the transformation plateau given an initial austenitic texture under tension.

While the tensile property of Nitinol is explored and analyzed, it is only a part of the possible mechanical deformation experienced by biomedical implant devices. Under torsional loading, Nitinol behaves very differently. However through S/N approaches, the differences in behavior can be effectively normalized for lifetime prediction purposes. To understand the difference from microscopic point of view, in Chapter VI, a novel form factor in the cruciform shape is used for characterization of *in situ* shearing effects. It is found that as opposed to tensile deformation, shear is not strongly influenced by orientation. The sloped transformation plateau appears to be a function of gauge cross-section area, or in other words, increase of the size of Lüders bands. This has the net effect of raising the load needed to transform the material due to increase in the volume of material ahead of Lüders bands needed to propagate the transformation forward. To confirm this behavior in tubular samples, some special experiment would need to be devised to test this hypothesis. Such experiment has been planned and hopefully will help pin down the exact mechanism behind the difference in mechanical behaviors between the loading modes. The suspicion currently is that the Lüders bands in tubes form a spiral that grows both length-wise as well as width-wise which acts as an increasing gauge cross-sectional area.

Lastly, the fatigue loading is observed under micro-XRD. It can be seen that fatigue texture evolution varies significantly depending upon initial texture as well as mode of loading. However it appears that transformation propagation is a competition of two processes, grain-boundary misorientation and orientation of the grains. Under shear deformation, it appears high-angle grain-boundary is favored for propagation instead of orientation effects. However under fatigue, the grain-boundary effects appear to disappear and but the texture is still sharpened. The difference in behavior between monotonic loading and cyclic loading suggests alternative mechanism behind fatigue degradation than monotonic transformation. Under tensile fatigue, the austenitic texture weakens, and the grain-boundary effect is not as pronounced. This suggests that orientation effects such as plasticity of austenite in hard orientation may contribute to the functional fatigue of Nitinol under cyclic tensile loading. Also investigated is wire fatigue, where the grain-boundary effect is significant. This may be a result of very strong initial texture in the wire form, where deformation factors such as geometric compatibility, transformation dilation and shielding effects tends to compete and form complex responses.

Given how important grain-boundary misorientation is for the transformation and fatigue behavior of Nitinol, it should be noted that that the samples made for micro-XRD have much larger grains than medical devices. In Chapter VII, it was found that smaller grains tend to have weaker texture than larger grains. This implies that Nitinol texture tends to sharpen through process of annealing. This also implies that biomedical implant devices tend to have much weaker texture than the XRD samples. This can be used to explain that while the grain-boundary density decreased in the synchrotron samples but a significant increase in functional fatigue is observed (after about 100 cycles), much more so than in testing of unannealed samples (after 10,000 cycles). In other words, these XRD samples have magnified the functional fatigue aspect of the

Nitinol. It remains to be seen in future experiments to determine if the testing results of XRD samples are representative of actual performance of biomedical implant devices.

After the investigations detailed in this text, several recommendation can be made for improving fatigue and mechanical performance of superelasticity of Nitinol. The key is to decrease the overall texture, while keeping the grain boundary density low. These are competing objectives, where decreasing grain boundary density implies annealing, which tends to sharpen the texture. This at least gives some ideas for ways to improve the processing of Nitinol.

VIII.i. Future studies

Due to time constraints, most of the "fatigue" samples at synchrotron were only cycled to 100 cycles. This is far from true fatigue (typically 10^6 cycles), thus future studies are planned for off-line fatigue up to 10^6 cycles for μXRD characterization for proper fatigue study. Furthermore, the observation of grain-boundary density effects calls for special characterization methods for studying actual biomedical device texture instead of annealed texture. It is not clear if recent changes to the beamline 12.3.2 have made improvements that can be used to collect diffraction patterns from sub-micron grains, but a few experiments using Electronic Beam Backscatter Diffraction (EBSD) are current underway for additional analysis and confirmation of finds at the Advanced Light Source.

Beyond the simple texture studies, several more advanced techniques could be used to gain much more information from the samples. One of the disadvantages of plain μXRD is that it is not clear where the diffraction occurred depth-wise in the sample. Because the samples are very thin ($0.3\,mm$), surface effects may dominate the results. A technique developed by Hrishikesh Bale [29] can collect and recover the grain structure in three dimensions. The technique works by varying the distance of the detector to the sample. Because the distance directly influences the angle of diffraction peaks, the variation in detector distance can be used to correlate the variation in peak angles. By triangulating the peaks, it is possible to pin-point the depth in the sample where the grain generated the peak in question. This technique has been successfully used for 3D grain reconstruction in cubic zirconia and can be easily adapted for usage in superelastic Nitinol.

Reference

1. Kauffman, G.B. and M. Isaac, *The Story of Nitinol: The Serendipitous Discovery of the Memory Metal and Its Applications.* The Chemical Educator, 1997. 2: p. 1.
2. Buehler, W.J., J.W. Gilfrich, and R.C. Wiley, *Effects of low-temperature phase changes on the mechanical properties of alloys near composition TiNi,.* Journal of Applied Physics 1963. 34: p. 475.
3. Wang, F.E., W.J. Buehler, and S.J. Pickart, *Crystal structure and a unique martensitic transition of TiNi.* Journal of Applied Physics, 1965. 36: p. 3232-3239.
4. Hall, P., *Method of Welding Titanium and Titanium Based Alloys to Ferrous Metals*, 2005.
5. Olander, A., Journal of American Chemical Society, 1932. 54: p. 3819.
6. Hornbogen, E., Z. Metallkunde, 1956. 47: p. 47.
7. Duerig, T.W., et al., *Engineering Aspects of Shape Memory Alloys*. 1990, London: Butterworth-Heinemann Ltd.
8. Ryhanen, J. *Biocompatibility of Nitinol*. in *SMST: The International Conference on Shape Memory and Superelastic Technologies*. 2000. Pacific Grove, CA, USA.
9. Yahia, L.H., *Shape Memory Implants*. 2000, Berlin: Springer.
10. Kujala, S., et al., *Biocompatibility and strength properties of nitinol shape memory alloy suture in rabbit tendon.* Biomaterials, 2004. 25(2): p. 353-358.
11. Duerig, T.W., A. Pelton, and D. Stockel, *An overview of nitinol medical applications.* Materials Science and Engineering A, 1999. 273-275: p. 149-160.
12. Duerig, T.W., D.E. Tolomeo, and M. Wholey, *An overview of superelastic stent design.* Minimally Invasive Therapy & Allied Technologies, 2000. 9(3/4): p. 235-246.
13. Duerig, T.W. *Applications of Shape Memory*. in *Materials Science Forum, in Martensitic Transformations II*. 1990.
14. Duerig, T.W. *Present and Future Applications of Shape Memory and Superelastic Materials*. in *Proceedings of the Materials Research Society Symposium*. 1995.
15. Duerig, T.W., et al., *Applications of Shape Memory in the USA.* New Materials and Processes for the Future, 1989: p. 195-200.
16. Pelton, A.R., D. Stoeckel, and T.W. Duerig, *Medical Uses of Nitinol.* Materials Science Forum, 2000. 327-328: p. 63-70.
17. Otsuka, K. and T. Kakeshita, *MRS Bulletin.* 2002. 27: p. 91.
18. Ono, N., A. Satoh, and H. Ohta, *A Discussion on the Mechanical Properties of Shape Memory Alloys Based on a Polycrystal Model* Trans Jpn Inst Metals, 1989. 30(10): p. 756-764.
19. Leary, M., F. Schiavone, and A. Subic, *Lagging for control of shape memory alloy actuator response time.* Materials & Design, 2010. 31(4): p. 2124–2128.

20. Michal, G.M. and R. Sinclair, *The structure of TiNi martensite.* Acta Crystallographica B 1981. 37: p. 1803-1806.
21. Tan, G. and Y. Liu, *Comparative study of deformation-induced martensite stabilisation via martensite reorientation and stress-induced martensitic transformation in NiTi.* Intermetallics, 2004. 4(12): p. 373-381.
22. Tan, L. and W.C. Crone, *In situ TEM observation of two-step martensitic transformation in aged NiTi shape memory alloy.* Scripta Materialia, 2004. 50(6): p. 819-823.
23. Uchil, J., K.K. Mahesh, and K.K. Ganesh, *Calorimetric study of the effect of linear strain on the shape memory properties of Nitinol.* Physica B: Condensed Matter, 2001. 305(1): p. 1-9.
24. Duerig, T.W., *Some unsolved aspects of Nitinol.* Materials Science and Engineering A. 2006(438-440): p. 69–74.
25. Duerig, T.W. and A.R. Pelton. *An Introduction to Nitinol Biomedical Devices*. in *Shape Memory and Superelastic Technologies Conference (SMST)*. 2003. Pacific Grove, CA, USA.
26. R.H., D., D. T.W., and R. R.O. *Effects of In Situ Phase Transformation on Fatigue-Crack Propagation in Titanium-Nickel Shape-Memory Alloys*. in *Proceedings of the MRS International Meeting on Advanced Materials Vol 9 Shape Memory Materials*. 1988. Tokyo, Japan.
27. Holtz, R.L., K. Sadananda, and M.A. Imam, *Fatigue thresholds of Ni-Ti alloy near the shape memory transition temperature.* International Journal of Fatigue, 1999. 21(137-145).
28. Mehta, A., et al., *On the electronic and mechanical instabilities in Ni50.9Ti49.1.* Materials Science and Engineering A, 2004. 378(1-2): p. 130-137.
29. Bale, H., *Measurement And Analysis Of Residual Stresses In Zirconia Dental Composites Using Micro X-Ray Diffraction*, in *School of Mechanical Engineering*2005, Oklahoma State University: Stillwater, Oklahoma.
30. Robertson, S.W., *On the Mechanical Properties and Microstructure of Nitinol for Biomedical Stent Applications*, in *Department of Materials Science and Engineering*2006, University of California, Berkeley: Berkeley, CA.
31. Miller, R.K. and W. Terri, *Survey on shape memory alloys.* 1989: p. 17.
32. Rocha-Singh, K.J., K. Scheer, and J. Rutherford, *Nitinol stent fractures in the superficial femoral artery: Incidence and clinical significance.* Journal of the American College of Cardiology, 2003. 41(6): p. 79-80.
33. Hayerizadeh, B.F., et al., *Long-term outcome of superficial femoral artery stenting using self-expandable nitinol stents compared to stainless steel stents: A retrospective multicenter study.* Journal of the American College of Cardiology, 2003. 41(6): p. 80.

34. Zarins, C.K., et al., *Explant analysis of AneuRx stent grafts: relationship between structural findings and clinical outcome.* Journal of Vascular Surgery 2004. 40(1): p. 1-11.
35. Riepe, G., et al., *What can we Learn from Explanted Endovascular Devices?* European Journal of Vascular and Endovascular Surgery, 2002. 8(24(2)): p. 117-122.
36. Chuter, T.A.M., *Stent-graft design: the good, the bad and the ugly.* Cardiovascular Surgery, 2002. 2(10(1)): p. 7-13.
37. Barras, C.D.J. and K.A. Myers, *Nitinol - Its Use in Vascular Surgery and Other Applications.* European Journal of Vascular and Endovascular Surgery, 2000. 19(6): p. 564-569.
38. Ginsberg, G.G., et al., *A new, self-expanding, nitinol, biliary stent: An in vivo evaluation.* Gastrointestinal Endoscopy, 1996. 4(43): p. 382.
39. Jacobs, T.S., et al., *Mechanical failure of prosthetic human implants: A 10-year experience with aortic stent graft devices.* Journal of Vascular Surgery, 2003. 37(1): p. 16-26.
40. Serruys, P. and M.J.B. Kutryk, *Handbook of Coronary Stents*. 2nd ed. 1998, London: Martin Dunitz Ltd.
41. Liermann, D.D., *STENTS: State of the Art and Future Developments*. 1995, Morin Heights, Canada: Polyscience Publications, Inc.
42. Leon, M.B. and G.S. Mintz, *Interventional Vascular Product Guide*. 1999, Washington DC, USA: Martin Dunitz, Ltd.
43. Marrey, R., X. D., and R.O. Ritchie, *Fatigue Life-Prediction Of Vascular Implants Subjected To Multiaxial Loads*, in *Computer Methods for Medical Devices: Validation of Computer with Nonclinical Models*2011: Silver Spring, MD.
44. Cheng, C.P., et al., *In vivo MR angiographic quantification of axial and twisting deformation of the superficial femoral artery resulting from maximum hip and knee flexion.* J Vasc Interv Radiol, 2006. 17(979-987).
45. Allie, D.E., C.J. Hebert, and C.M. Walker, *Nitinol stent fractures in the SFA.* Endovasc Today, 2006. 8: p. 22-34.
46. Nikanorov, A., et al., *Fracture of self-expanding Nitinol stents stressed in vitro under simulated intravascular conditions.* J Vasc Surg, 2008. 48: p. 435-440.
47. Robertson, S.W., A.R. Pelton, and R.O. Ritchie, *Mechanical fatigue and fracture of Nitinol.* International Materials Reviews, 2011. 57(1): p. 1-36.
48. Pelton, A.R., et al., *Fatigue and Durability of Nitinol Stents.* J mechanical behavior of biomedical materials, 2008. 1: p. 153–164.
49. Tamura, N., et al. *Submicron x-ray diffraction and its applications to problems in materials and environmental science*. 2002. AIP.

50. Robertson, S.W., et al., *Evolution of crack-tip transformation zones in superelastic Nitinol subjected to in situ fatigue: A fracture mechanics and synchrotron X-ray microdiffraction analysis.* Acta Materialia, 2007. 55(18): p. 6198-6207.
51. Cheng, C.P., et al., *The effect of aging on deformations of the superficial femoral artery resulting from hip and knee flexion: Potential clinical implications.* J Vasc Inter Radiol, 2010. 21(195-202).
52. Ganguly, A., et al., *In-vitro imaging of femoral artery Nitinol stents for deformation analysis.* J Vasc Interv Radiol, 2011. 22: p. 236-243.
53. Ganguly, A., et al., *In-vivo imaging of femoral artery Nitinol stents for deformation analysis.* J Vasc Interv Radiol, 2011. 22(244-249).
54. Jaff, M., et al., *Standardized evaluation and reporting of stent fractures in clinical trials of noncoronary devices.* Catheter Cardiovasc Interv, 2007. 70: p. 460-462.
55. Scheinert, D., et al., *Prevalence and clinical impact of stent fractures after femoropopliteal stenting.* J Am Coll Caridol, 2005. 45(312-315).
56. Kim, Y.S. and S. Miyazaki. *Fatigue properties of Ti-50.9at%Ni shape memory wires*. in *SMST-97: Proceedings of the Second International Conference on Shape Memory and Superelastic Technologies*. 1997. Pacific Grove, California: International Organization on SMST.
57. Reinhoehl, M., et al. *The influence of melt practice on final fatigue properties of superelastic NiTi wires*. in *SMST-2000: Proceedings of the International Conference on Shape Memory and Superelastic Technologies.* 2000. Pacific Grove, California: International Organization on SMST.
58. McNichols, J.L., P.C. Brookes, and J.S. Cory, *NiTi fatigue behavior.* J Appl Phys, 1981. 52: p. 7742-7744.
59. Melton, K.N. and O. Mercier, *Fatigue of NiTi thermoelastic martensites.* Acta Metall, 1979. 27: p. 137-144.
60. Pelton, A.R., X.Y. Gong, and T.W. Duerig. *Fatigue testing of diamond-shaped specimens*. in *SMST-2003: Proceedings of the International Con-ference on Shape Memory and Superelastic Technologies*. 2003. Pacific Grove, California: International Organization on SMST.
61. Pelton, A.R., et al., *Fatigue and durability of Nitinol stents.* J Mech Behav Biomed Mater, 2008. 1(153-164).
62. Tabanli, R.M., N.K. Simha, and B.T. Berg, *Mean stress effects on fatigue of NiTi.* Mater Sci and Eng A, 1999. 273-275: p. 644-648.
63. Tolomeo, D., S. Davidson, and M. Santinoranont. *Cyclic properties of superelastic Nitinol: Design implications*. in *SMST-2000: Proceedings of the International Conference on Shape Memory and Superelastic Technologies*. 2000. Pacific Grove, California: International Organization on SMST.

64. Kugler, C., D. Matson, and K. Perry, *Non-zero mean fatigue test protocol for NiTi*, in *SMST-2000: Proceedings of the International Conference on Shape Memory and Superelastic Technologies*, P.A. Russell MS, Editor 2000, International Organization on SMST: Pacific Grove, California. p. 409-417.
65. Harrison, W.J. and Z.C. Lin, *The study of Nitinol bending fatigue*, in *SMST-2000: Proceedings of the International Conference on Shape Memory and Superelastic Technologies*, P.A. Russell MS, Editor 2000, International Organization on SMST: Pacific Grove, California. p. 391-396.
66. McNaney, J.M., et al., *An experimental study of the superelastic effect in a shape-memory Nitinol alloy under biaxial loading.* Mechanics of Materials, 2003. 35(10): p. 969-86.
67. Adler, P.H., et al., *On the tensile and torsional properties of pseudoelastic NiTi.* Scr Metall et Mater, 1990. 24: p. 943-947.
68. Imbeni, V., et al. *On the mechanical behavior of Nitinol under multiaxial loading conditions and in situ synchro-tron X-rays*. in *SMST-2003: Proceedings of the Interna-tional Conference on Shape Memory and Superelastic Technologies*. 2003. Pacific Grove, California: International Organization on SMST.
69. McNaney, J.M., et al., *An experimental study of the superelastic effect in a shape-memory Nitinol alloy under biaxial loading.* Mech of Mater, 2003. 35: p. 969-986.
70. Olier, P., P. Matheron, and J. Sicre, *Experimental study of torsion behavior of NiTi alloy.* J De Phys IV, 2004. 115: p. 185-194.
71. Predki, W., M. Klonne, and A. Knopik, *Cyclic torsional loading of pseudoelastc NiTi shape memory alloys: Damping and fatigue failure.* Mater Sci and Eng A, 2006. 417: p. 182-189.
72. Shigley, J.E. and C.R. Mischke, *Mechanical Engineering Design*. 1 ed. 1989, New York: McGraw-Hill.
73. Manson, S.S. and K. Jung, *Progress in the development of a three-dimensional fatigue theory based on the multiaxiality factor*, in *ASME Pressure Vessel and Piping Vol. 290*. 1994, American Society for Mechanical Engineers: Warrendale, PA. p. 85-93.
74. Smith, R.N., P. Watson, and T.H. Topper, *A stress-strain function of the fatigue of metals.* J Mater JMLSA, 1970. 5: p. 767-778.
75. M.W., B. and M. K.J., *A theory of fatigue under multiaxial strain conditions.* Proc Inst Mech Eng, 1973. 187: p. 745-755.
76. Coffin, L.F., *A study of the effect of cyclic thermal stresses on a ductile metal.* Trans Am Soc Mech Eng, 1954. 76: p. 931-950.
77. Manson, S.S., *Behavior of materials under conditions of thermal stress*, in *National Advisory Commission on Aeronautics: Report 1170*1954, Lewis Flight Propulsion Laboratory;: Cleveland, OH.

78. Schillinger, M., et al., *Balloon angioplasty versus implantation of Nitinol stents in the superficial femoral artery.* New England Journal of Medicine, 2006. 354(18): p. 1879-1888.

79. Duerig, T.W., A.R. Pelton, and D. Stockel, *The utility of superelasticity in medicine.* Bio-Medical Materials and Engineering, 1996. 6: p. 255-266.

80. Robertson, S.W., X.Y. Gong, and R.O. Ritchie, *Effect of product form and heat treatment on the crystallographic texture of austenitic Nitinol.* Journal of Materials Science, 2006. 41(3): p. 621-30.

81. Cheng, C.P., et al., *In Vivo MR Angiographic Quantification of Axial and Twisting Deformations of the Superficial Femoral Artery Resulting from Maximum Hip and Knee Flexion.* Journal Vascular Interventional Radiology, 2006. 17: p. 979–987.

82. Cheng, C.P., et al., *The Effect of Aging on Deformations of the Superficial Femoral Artery Resulting from Hip and Knee Flexion: Potential Clinical Implications.* J Vasc Interv Radiol, 2010. 21(2): p. 195–202.

83. Rebelo, N. and M. Perry, *Finite element analysis for the design of nitinol medical devices.* Min. Invas. Ther. & Allied Technol, 2000. 9(2): p. 453-462.

84. Mehta, A., et al., *Understanding the Deformation and Fracture of Nitinol Endovascular Stents using In Situ Synchrotron X-Ray Micro-diffraction.* Advanced Materials, 2007. 19(May): p. 1183-1186.

85. Bhattacharya, K., *Microstructure of Martensite*. 2003, Oxford: Oxford University Press. 288.

86. Jung, Y., P. Papadopoulos, and R.O. Ritchie, *Constitutive modelling and numerical simulation of multivariant phase transformation in superelastic shape-memory alloys.* International Journal for Numerical Methods in Engineering, 2004. 60: p. 429-460.

87. Wick, A., O. Vöhringer, and A. Pelton, *The Bending Behavior of NiTi.* J. de Phys, 1995. 5(IV Coll. C8): p. 789-794.

88. Kröger, A., et al., *In situ transmission electron microscopy-investigations on the strain-induced B19'-phase in NiTi shape memory alloys structured by focused ion beam.* Materials Science and Engineering: A, 2006. 438-440: p. 513-516.

89. Brinson, L.C., I. Schmidt, and R. Lammering, *Stress-induced transformation behavior of a polycrystalline NiTi shape memory alloy: micro and macromechanical investigations via in situ optical microscopy.* J. Mech. Phys. Solid, 2004. 52: p. 1549.

90. Miyazaki, S., et al., *The habit plane and transformation strains associated with the martensitic transformation in Ti-Ni single crystals.* Scripta Metallurgica, 1984. 18(9): p. 883-888.

91. Ono, N. and A. Sato, *Plastic Deformation Governed by the Stress Induced Martensitic Transformation in Polycrystals.* Trans Jpn Inst Metals, 1988. 29: p. 267-273.

92. Shaw, J.A. and S. Kyriakides, *On the nucleation and propagation of phase transformation fronts in a NiTi alloy.* Acta Materialia, 1997. 45(2): p. 683-700.

93. Hasan, M., et al., *Hard X-ray studies of stress-induced phase transformations of superelastic NiTi shape memory alloys under uniaxial load.* Materials Science and Engineering: A, 2008. 481-482: p. 414-419.

94. Barney, M., et al., *Patterns of Martensite Transformation in Textured NiTi.* 2010.

95. Kennedy, J.M., T.R. Barnett, and G.L. Farley, *Experimental and Analytical Evaluation of A Biaxial Test for Determining In-Plane Shear Properties of Composites.* SAMPE quarterly, 1992. 24(1): p. 28-37.

96. Hielscher, R. and H. Schaeben, *A novel pole figure inversion method: specification of the MTEX algorithm.* Journal of Applied Crystallography, 2008. 41(6): p. 1024-1037.

97. Bachmann, F., R. Hielscher, and H. Schaeben, *Texture Analysis with MTEX--Free and Open Source Software Toolbox.* Solid State Phenomena, 2010. 160: p. 63-68.

98. Runciman, A., et al., *An equivalent strain/Coffin-Manson approach to multiaxial fatigue and life prediction in superelastic Nitinol medical devices.* 2010. 32(22): p. 4987-93.

99. Hosford, W.F., *The Mechanics of Crystals and Texture Polycrystals*. 1993, New York: Oxford Pressure.

100. Kocks, U.F., C.N. Tome, and H.R. Wenk, *Texture an Anisotropy*. 1999, New York: Cambridge Pressure.

101. Reid, C.N., *Deformation Geometries for Materials Scientists*. 1973, New York: Oxford Press.

102. Clausen, B., *Characterisation of Polycrystal Deformation*, 1997, Risø National Laboratory: Roskilde, Denmark.

103. O., N. and A. Sato, *Plastic Deformation Governed by the Stress Induced Martensitic Transformation in Polycrystals.* Transactions of the Japan Institute of Metals, 1988. 29(4): p. 267-273.

104. Noboru, O., A. Satoh, and H. Ohta, *A Discussion on the Mechanical Properties of Shape Memory Alloys Based on a Polycrystal Model.* Materials Transactions, JIM, 1989. 30(10): p. 756-764.

Appendix A: Normalized Strain in Tension and Torsion

Below is the mathematics used to normalize the strains in tension and torsion used in Chapter III. The normalization is through the Von Mises criterion, with special consideration for the “plastic” strain.

Traditional normalized strain is defined via incremental plastic strain, however since we are not concerned with strain history but rather the magnitude nor does plasticity play a major role, we can safety discard the incremental as well as plastic portion of the Von Mise Strain and arrive at:[99]

$$\varepsilon^2 = \frac{4}{9}\left\{\frac{1}{2}[(\varepsilon_{11}-\varepsilon_{22})^2+(\varepsilon_{22}-\varepsilon_{33})^2+(\varepsilon_{33}-\varepsilon_{11})^2]+3(\varepsilon_{12}^2+\varepsilon_{13}^2+\varepsilon_{23}^2)\right\}$$

In tension strain state is as follows (plastic $\nu = 0.5$, assumes constancy of volume), with loading axis as z:

$$\varepsilon = \begin{bmatrix} -\nu\varepsilon_{zz} & 0 & 0 \\ 0 & -\nu\varepsilon_{zz} & 0 \\ 0 & 0 & \varepsilon_{zz} \end{bmatrix} = \begin{bmatrix} \frac{-\varepsilon_{zz}}{2} & 0 & 0 \\ 0 & \frac{-\varepsilon_{zz}}{2} & 0 \\ 0 & 0 & \varepsilon_{zz} \end{bmatrix}$$

$$\varepsilon^2 = \frac{4}{9}\left\{\frac{1}{2}\left[\left(\frac{-\varepsilon_{zz}}{2}-\frac{-\varepsilon_{zz}}{2}\right)^2+\left(\frac{-\varepsilon_{zz}}{2}-\varepsilon_{zz}\right)^2+\left(\varepsilon_{zz}-\frac{-\varepsilon_{zz}}{2}\right)^2\right]+3(0^2+0^2+0^2)\right\}$$

$$\varepsilon^2 = \frac{4}{9}\left\{\frac{1}{2}\left[0^2+\left(\frac{-3\varepsilon_{zz}}{2}\right)^2+\left(\frac{3\varepsilon_{zz}}{2}\right)^2\right]\right\}$$

$$\varepsilon^2 = \frac{4}{9}\left\{\frac{1}{2}\left[\frac{9\varepsilon_{zz}^2}{4}+\frac{9\varepsilon_{zz}^2}{4}\right]\right\}$$

$$\varepsilon^2 = \frac{4}{9}\left\{\frac{1}{2}\left[\frac{18\varepsilon_{zz}^2}{4}\right]\right\} = \frac{4}{9}\left\{\frac{9\varepsilon_{zz}^2}{4}\right\} = \varepsilon_{zz}^2$$

$$\varepsilon = \varepsilon_{zz}$$

Above is not a surprise as Von Mises Strain is defined to be exactly same as uniaxial tension strain.

In torsion, the strain state is as follows (uses cylindrical coordinates, with torque applied on the x axis):

$$\varepsilon = \begin{bmatrix} 0 & 0 & 0 \\ 0 & 0 & \varepsilon_{\theta z} \\ 0 & \varepsilon_{\theta z} & 0 \end{bmatrix}$$

$$\varepsilon^2 = \frac{4}{9}\left\{\frac{1}{2}[0^2 + 0^2 + 0^2] + 3\left(0^2 + 0^2 + \varepsilon_{\theta z}^2\right)\right\}$$
$$\varepsilon^2 = \frac{4}{9}\{3\varepsilon_{\theta z}^2\} = \frac{4}{3}\varepsilon_{\theta z}^2$$
$$\varepsilon = \sqrt{\frac{4}{3}}\varepsilon_{\theta z}$$

To obtain the equivalence between the torsional strain and tension strain, we must set them equal and find the conversion factor:

$$\varepsilon_{zz} = \sqrt{\frac{4}{3}}\varepsilon_{\theta z}$$
$$\boxed{\varepsilon_{\theta z} = \frac{\varepsilon_{zz}\sqrt{3}}{2}}$$

Torsion of a rod from statics (where γ is the twist angle)

$$\gamma = \frac{\theta r_o}{l}$$

And

$$\frac{\gamma}{2} = \varepsilon_{\theta z}$$

Therefore

$$\boxed{\varepsilon_{\theta z} = \frac{\theta r_o}{2l}}$$
$$\boxed{\theta = \frac{2l\varepsilon_{\theta z}}{r_o}}$$
$$\frac{\varepsilon_{zz}\sqrt{3}}{2} = \frac{\theta r_o}{2l}$$
$$\boxed{\theta = \frac{\sqrt{3}l\varepsilon_{zz}}{r_0}}$$

Above results are used extensively in Chapter III. This appendix is provided to help establish convention that ε is used for shear strain, which is half of γ which is typically shear angle after deformation.

Similarly we can do the same for stress in tension:

$$\sigma = \begin{bmatrix} 0 & 0 & 0 \\ 0 & 0 & 0 \\ 0 & 0 & \sigma_{zz} \end{bmatrix}$$

$$\bar{\sigma} = \sqrt{\frac{1}{2}[(\sigma_{11} - \sigma_{22})^2 + (\sigma_{11} - \sigma_{33})^2 + (\sigma_{22} - \sigma_{33})^2] + 3(\sigma_{12}^2 + \sigma_{23}^2 + \sigma_{13}^2)}$$

$$= \sqrt{\frac{1}{2}[0^2 + \sigma_{zz}{}^2 + \sigma_{zz}{}^2] + 3(0^2 + 0^2 + 0^2)}$$

$$\bar{\sigma} = \sigma_{zz}$$

As well as in torsion:

$$\sigma = \begin{bmatrix} 0 & 0 & 0 \\ 0 & 0 & \sigma_{\theta z} \\ 0 & \sigma_{\theta z} & 0 \end{bmatrix}$$

$$\bar{\sigma} = \sqrt{\frac{1}{2}[(\sigma_{11} - \sigma_{22})^2 + (\sigma_{11} - \sigma_{33})^2 + (\sigma_{22} - \sigma_{33})^2] + 3(\sigma_{12}^2 + \sigma_{23}^2 + \sigma_{13}^2)}$$

$$= \sqrt{\frac{1}{2}[0^2 + 0^2 + 0^2] + 3\left(0^2 + 0^2 + \sigma_{\theta z}^2\right)}$$

$$\bar{\sigma} = \sqrt{3}\sigma_{\theta z}$$

$$\sqrt{3}\sigma_{\theta z} = \sigma_{zz}$$

Above contains everything needs to convert shear stress/strain into equivalent stress/strain.

Appendix B: Inverse Pole Figure and Miller Indices

Stereographic projection is a special method for visualizing three-dimensional geometry on a two-dimensional surface. It works by extending the normal vector of the planes to a sphere. Then a point on the sphere projects a line towards the intersection point of plane normal on sphere towards the projection plane [100]. The mathematics below shows how to convert crystallographic indices into stereographic projection coordinates. It is then followed by converting the stereographic projection in the inverse pole figure coordinate for cubic materials.

Miller indices (hkl) describes a plane with normal vector $[hkl]$.

Stereographic projection requires "poles" on a unit sphere to be projected from a reference point onto a plane.

$$x^2 + y^2 + z^2 = 1$$

A (hkl) plane with its normal vector will result in a pole on the unit sphere at the location:

$$(x, y, z) = \left(\frac{h}{\sqrt{h^2 + k^2 + l^2}}, \frac{k}{\sqrt{h^2 + k^2 + l^2}}, \frac{l}{\sqrt{h^2 + k^2 + l^2}}\right)$$

A projection from pole to plane result in equation:

$$(X, Y) = \left(\frac{Jx}{1 - z}, \frac{Jy}{1 - z}\right)$$

Where J is a scaling factor, depending on the location of plane and is completely arbitrary

Substituting and solve for (X, Y) projected location, and using inverse pole figure with $(00\bar{1})$ as the reference point and $(1kl)$ with $k > l$ planes

$$(X, Y) = \left(\frac{Jk}{1 + \sqrt{1 + k^2 + l^2}}, \frac{Jl}{1 + \sqrt{1 + k^2 + l^2}}\right)$$

J scaling factor:

1) If $(111) \equiv (1,1)$ then $J = 1 + \sqrt{3}$, but $(110) \equiv (1.132,0)$
2) If $(110) \equiv (1,0)$ then $J = 1 + \sqrt{2}$, but $(111) \equiv (0.884,0.884)$
3) If $J = 1$, then $(110) \equiv (0.414,0)$ and $(111) \equiv (0.366,0.366)$

Reverse transformation $(X, Y) \rightarrow (1kl)$

$$k = \frac{2JX}{J^2 - X^2 - Y^2}$$

$$l = \frac{2JY}{J^2 - X^2 - Y^2}$$

Using the above, one could convert the normalized miller indices and obtain the inverse pole figure coordinate in Cartesian form. This equation is used extensively to plot the IPF seen in the text.

Appendix C: Modified Taylor Factor for Nitinol

The bulk of this text is dedicated to analysis of micro-scale texture and deformation of Nitinol through the use of synchrotron X-ray characterization. However numerical methods where the overall stress state is determined through modeling of deformation of polycrystalline material can be used as well. However difficulty arises in classical mechanical deformation the main strain element is plasticity itself, whereas in Nitinol the strain is mostly from transformation. However through simplification and some basic assumptions, it is shown that a Modified Taylor Factor (MTF) can accurate predict some basic transformation plateau behavior of the material given a particular texture.

The basic Taylor model is rigid plastic models, and assumes that all polycrystalline grains are subjected to the same applied strain. This typically yields an upper bound estimate of the bulk behavior. Alternative models such as Sachs model where the grains are subjected to same applied stress tend to yield a lower bound estimate. However both sets of models are mostly independent of material characteristics due to assumptions of lack of grain-to-grain interactions. More sophisticated models based on Eschelby's inclusion theory where the self-consistent scheme takes care of granular interactions do account for more of the material characteristics. For this text, the MTF model will be used for the analysis and prediction of the textural influence on the bulk mechanical properties. Future developments using more capable model may be able to capture more details and predict much more of the Nitinol mechanical behaviors [101].

C.i Basic Taylor Model

Taylor in 1938 proposed a model for computing the uniaxial stress-strain behavior for a polycrystalline material, where the polycrystal is comprised of agglomeration of randomly oriented FCC single crystal grains. The main assumption in simplifying the computation is that these grains will be rigid plastic in mechanical property [102].

In uniaxial tension, the active slip system that accommodates the tensile deformation is the one with highest resolved shear stress (Schmidt's law). By assuming the sample area is A and applied load as P, the normal tensile stress is defined as $\sigma_{xx} = F/A$. If the angle from the active slip plane to the normal loading plane is α, then the force acting upon the slipping area is $F_{slip} = P\cos\alpha$. Furthermore, the active slip direction can be defined as having angle of β away from loading direction, then the slipping stress on the active slip system and slip direction is defined as: $\tau = \sigma\cos\alpha\cos\beta$ [102].

Above is the result of a single active slip as a result of applied loading. This is only reasonable for single crystalline material with a dominant slip system. However in polycrystalline materials, there will necessarily be more than a single active slip system, even by assuming a single active slip per grain. Thus the above slip stress can be rewritten to account for the multiple slip by defining the Taylor factor, m:

$$m = \frac{\sigma}{\tau} = \cos\alpha\cos\beta = \frac{\gamma}{\varepsilon}$$

Where m above is rewriting as the ratio between the applied tensile stress and the active slip stress for uniaxial loading (and similarly for strains). However if the system is an polycrystalline aggregate, the geometrical compatibility as well as physical constraints dictate which slip systems are to be active. Taylor made the assumption, through Merchant's theorem, that a minimum of five system slips are necessary to accommodate any generic loading and deformation. Each slip system will have its own unique planar angle, α_i and directional angle, β_i. Thus the active systems will be sum of all of the slip systems, and therefore we can define the Taylor factor for polycrystalline FCC material as [99, 101]:

$$m = \sum \cos\alpha_i \cos\beta_i = \frac{\sum\gamma}{\varepsilon}$$

To correctly predict the mechanical behavior, the key is to select the right slip systems. Taylor hypothesized that amongst all the combinations of five systems that are capable of accommodating the imposed strain, the active combination is the one with the minimum overall accumulated slip. In other words, select amongst all possible variations of five slip systems such that the m is the smallest.

Taylor's work further continues by assuming the basic slip systems for FCC system, where the slips systems all occur on the four close-packed $\{111\}$ and in the $\langle 110\rangle$ direction on the plane. By varying the combinations of the minimum slip, Taylor was able to compute the m factor for all orientations and predict the hard and easy texture in FCC materials [100, 102].

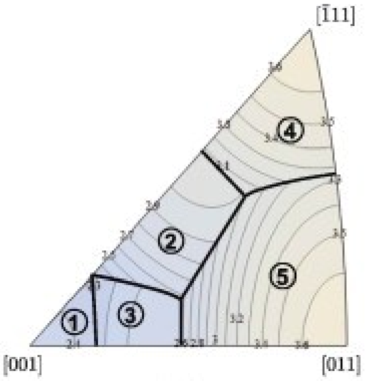

Figure C.1: Taylor Factor for FCC material as calculated by Taylor [102].

In Figure C.1, an inverse pole figure is plotted showing the values of m as a function of miller indices $\{1kl\}$, where the normalization and symmetry reduces all possible miller indices down to the above triangle. The circled number is the domain of active slip systems, and contours are the values of m. Therefore for generic FCC material, there are five regions of different slip systems depending on loading configuration and material texture. Thus, to utilize the Taylor factor, the loading in relations to the texture can be determined and plotted on the inverse pole figure above.

To convert the Taylor model for shape memory transformation strain effect, there are a couple modifications that are needed. The slip mechanism obviously does correlate to transformation. However if the slip plane and direction is replaced by martensitic habit planes and variation directions, it is possible to compute the now, modified Taylor factor. However, because there are different variations, the amount of slip on each orientation must be defined as well. In Ono and Sato's work, their methodology is as follows [103]:

$$\nu^s \geq 0, \min \sigma_i m_i^s \eta$$

Where ν^s is the volume fracture of the variant in variation s, σ_i is the ith component of stress, and m_i^s is the martensitic strain of sth variant and ith component, and η is the magnitude of the sth variant. By characterizing the actual martensitic habit planes and variant martensitic strains, Ono and Sato computed the modified Taylor factor for several shape memory alloys [104].

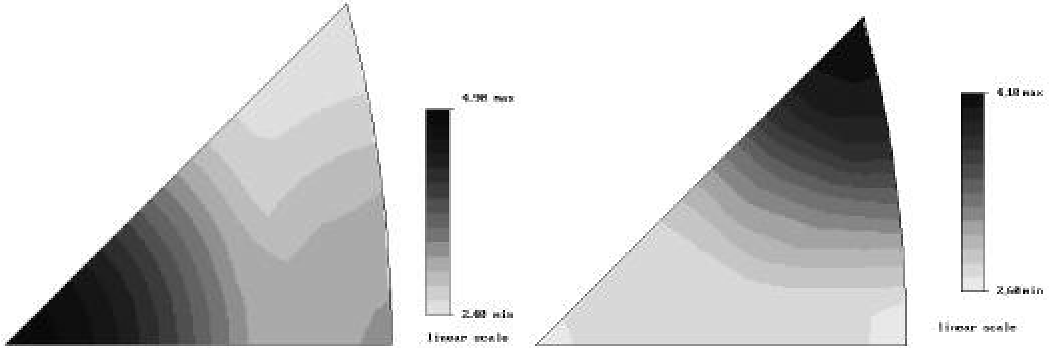

Figure C.2: Modified Taylor factor distribution showing the factor as a function of texture and uniaxial tensile loading direction (left), and uniaxial compressive loading direction (right) [30].

In Figure C.2, it can be seen that in tension, the easy direction (lighter shade of gray) corresponds to $\{111\}$ orientation, whereas in compression tends to be $\{100\}$ and $\{110\}$ orientations. This effect on tensile deformation is explored extensively in Chapter V.

Appendix D: Interpretations of Orientation Density Function

Texture is the preferred orientation of grains in a polycrystalline material. The challenge in studying texture is the representation of a three-dimensional object (the texture) on a two-dimension surface. Traditional projections such as pole figures, or inverse pole figures reduces the information and thus requires the complete texture to be represented by at least two 2D figures. However it is possible to construct, at least mathematically, a 3D representation of the texture, from which the various 2D projections are extracted. This single object (orientation density function, ODF) represents the complete texture and can be used for quantitate calculations [100].

In typical materials science, the coordinate basis for representation of atomic planes and directions are Cartesian based. Directions are indicated in arrow brackets:

$$\langle uvw \rangle = u\mathbf{i} + v\mathbf{j} + w\mathbf{k}$$

where $\mathbf{i}, \mathbf{j}, \mathbf{k}$ are the unit vectors in orthonormal Cartesian coordinate. Planes are designated in curly brackets (miller indices), $\{hkl\}$, where hkl denotes the normal vector that defines the plane.

Miller index alone is not enough to specify completely the orientation of a particular grain. This is because a plane is free to move about its normal vector, thus a $\{111\}$ plane is can be aligned with its $\langle \bar{1}10 \rangle$ axis in one particular direction. To completely define a unique orientation, two vectors are needed, a planar normal vector (miller indices), and a directional vector that is aligned to a direction in the sample coordinate. Thus the typical format for specifying an orientation in Cartesian coordinate is $\{hkl\}\langle uvw \rangle$, where $\langle uvw \rangle$ is the vector that is aligned, typically to rolling direction, of the sample, and $\{hkl\}$ is the plane that contains the vector.

However the above coordinate basis is not very suitable for ODF calculations. An alternative definition of orientation through the viewpoint of rotation can be used to arrive at a better basis. However rotation in three-dimensional space is not unique. Thus there are numerous alternatives and often conflicting definition of rotational coordinates for ODF. In this text, the original Bunge angles are to be used.

Euler angles defines three successive rotations, that when performed in the correct order, will transform from the sample coordinate into the grain orientation. The three angles are defined as follows [100]:

1. ϕ_1, rotation about the normal direction (typically Z-axis, or Normal direction if defined).
2. Φ, rotation about the new rolling direction
3. ϕ_2, rotation about the new normal direction

This defines a unique coordinate basis that completely specifies orientation.

If the Euler space from above is used for ODF basis, several properties emerge and is helpful for the computation. The key being that it is periodic (2π), which limits the space of possible orientations. Furthermore, coupling of the crystal symmetry will increase its periodicity, which further reduces the unique spaces. For cubic crystals, the periodicity is such that all three angles are limited to $[0, \pi/2)$. This allows for easy visualization and fast computation [100].

If all of the grains within a polycrystalline material are characterized and indexed, and their orientations plotted in the Euler space, an ODF can be computed. The ODF defines the probability of finding a particular orientation. ODF is important because pole figure and inverse pole figures are actually special projection of the ODF in Euler space. Thus one single ODF uniquely determines the particular texture. Because it is unique, quantitative calculations can be made on the ODF which represent the texture itself.

There are two main methods for obtaining ODF through the raw granular orientation. The main method used in the software package, MTEX, used in this text is the harmonic method. This method first discretizes the Euler space with the orientations. Then the density of orientations is computed and a converging Fourier series is used to approximate the density. This has the benefit of smooth ODF that is rapid to compute and relatively insensitive to noise in the sample. However it suffers from "ghosts" where the Fourier series overshoot can introduce false densities. The software package MTEX uses numerous specialized techniques to eliminate ghosts to prevent it from influencing the data.

Representation of ODF is difficult because it is a three-dimensional object. While it is possible to plot the ODF in projection, ODF typically contains holes and crevices that are difficult to make out on plots. A technique where two-dimensional slices of the ODF can be plotted involves choosing an axis of the Euler space to be fixed for the slice, and the 2D plots of the other coordinate can be made.

ODF when plotted in slices often times contains "fibers." These fibers are essentially a texture feature of the ODF that shows up on the ODF slices as straight lines. It is found experimentally that for FCC, the fibers tend to reveal itself best in ϕ_1 slices. However for BCC materials, and Nitinol, the ODF is best viewed through ϕ_2 slices. This is because most of the fibers for BCC material are found on the $\phi_2 = 45°$ slice.

Table D.1: The common fiber textures found on BCC type materials along with their corresponding orientation [100]

Fiber	Fiber Axis	Orientation
α	$\langle 011 \rangle \parallel RD$	$\{001\}\langle 110 \rangle - \{111\}\langle 1\bar{1}0 \rangle$
γ	$\langle 111 \rangle \parallel ND$	$\{111\}\langle 1\bar{1}0 \rangle - \{111\}\langle 112 \rangle$
η	$\langle 001 \rangle \parallel RD$	$\{001\}\langle 100 \rangle - \{011\}\langle 100 \rangle$
ε	$\langle 011 \rangle \parallel \mathrm{TD}$	$\{001\}\langle 110 \rangle - \{111\}\langle 112 \rangle$
β	-	$\{112\}\langle 1\bar{1}0 \rangle - \{\overline{11}\ 11\ \bar{8}\}\langle 4\ 4\ \overline{11} \rangle$

Thus by looking at the slices of ODF, in particular $\phi_2 = 45°$ slice, it is possible to infer the dominant texture of Nitinol.

In addition to qualitative observations, a few calculations can be made on ODFs. Texture index is the root mean square of the ODF. It essentially measures the sharpness of the texture, where the smaller the index is the more random and weak the texture is. Furthermore, ODF can used to compute misorientation if coupled with spatially indexed data. This can be used to analyze grain boundary angle and axis distribution.

All calculations are done on the MTEX[11] software package which automates most of the tedious symmetry operation and plotting package.

---

[11] http://code.google.com/p/mtex/

Appendix E: Colorcoding using crystallographic directions

To represent texture on a spatial mapping is difficult; however it can be remedied by applying color on spatial map. There are many methods for color coding according to the crystallographic orientations, however in cubic material and for this text, the following chart is used for color coding using the miller indices. The plot is inverse pole figure, which shows all the possible symmetric orientation found in a cubic material within a triangular shape. The color associated with each pole on the IPF is the color used by spatial mapping method. It is defined by taking the {111} as green, {111} as red, and {110} as blue.

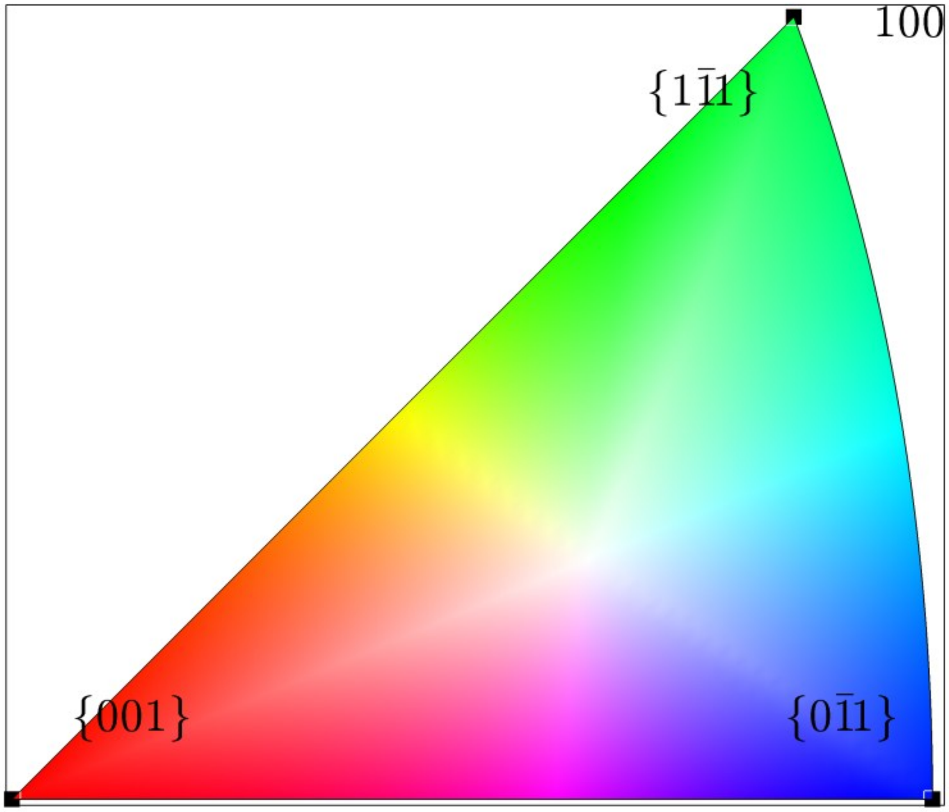

Figure E.1: Color coding using miller indices for cubic materials

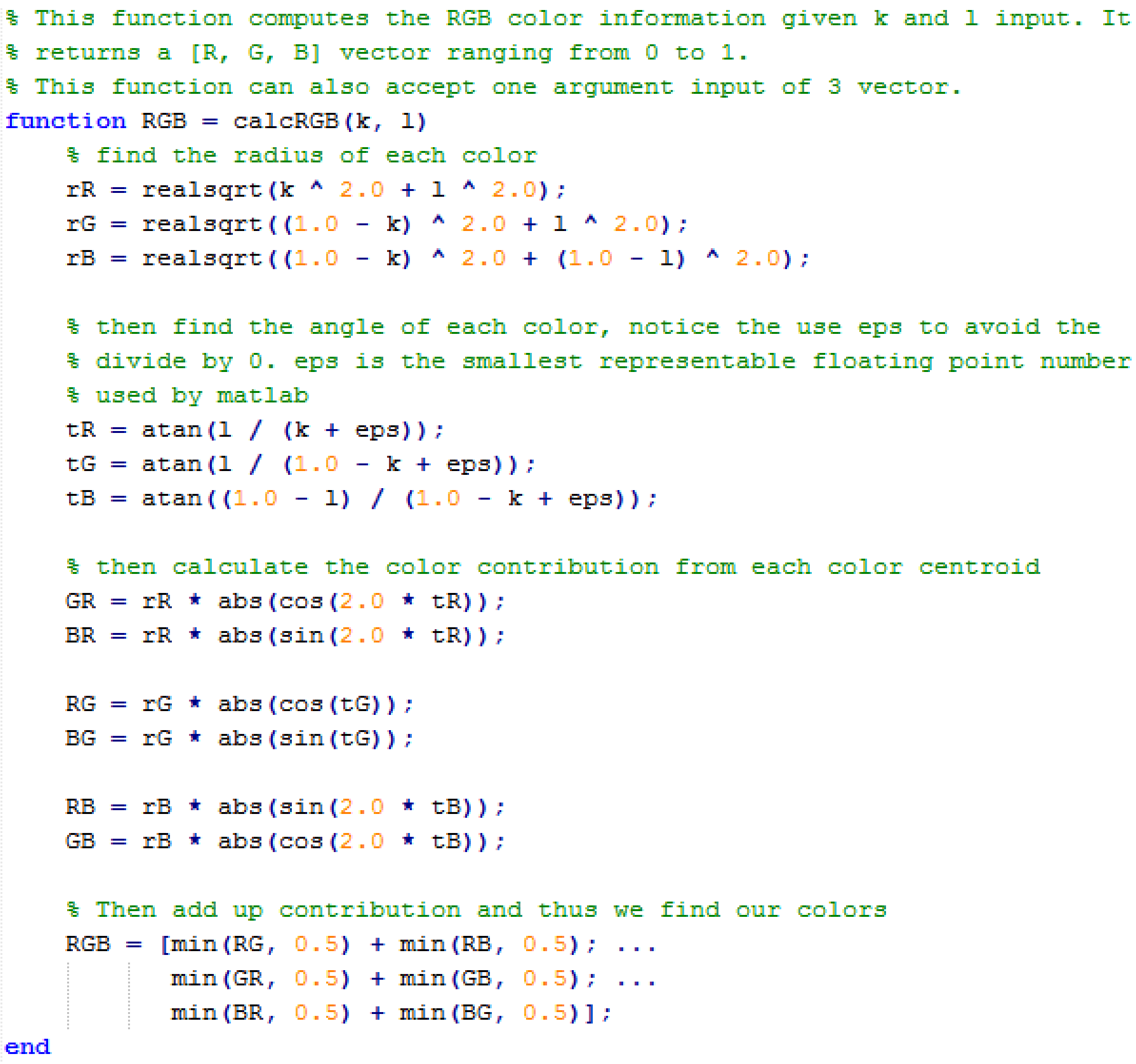

```matlab
% This function computes the RGB color information given k and l input. It
% returns a [R, G, B] vector ranging from 0 to 1.
% This function can also accept one argument input of 3 vector.
function RGB = calcRGB(k, l)
    % find the radius of each color
    rR = realsqrt(k ^ 2.0 + l ^ 2.0);
    rG = realsqrt((1.0 - k) ^ 2.0 + l ^ 2.0);
    rB = realsqrt((1.0 - k) ^ 2.0 + (1.0 - l) ^ 2.0);

    % then find the angle of each color, notice the use eps to avoid the
    % divide by 0. eps is the smallest representable floating point number
    % used by matlab
    tR = atan(l / (k + eps));
    tG = atan(l / (1.0 - k + eps));
    tB = atan((1.0 - l) / (1.0 - k + eps));

    % then calculate the color contribution from each color centroid
    GR = rR * abs(cos(2.0 * tR));
    BR = rR * abs(sin(2.0 * tR));

    RG = rG * abs(cos(tG));
    BG = rG * abs(sin(tG));

    RB = rB * abs(sin(2.0 * tB));
    GB = rB * abs(cos(2.0 * tB));

    % Then add up contribution and thus we find our colors
    RGB = [min(RG, 0.5) + min(RB, 0.5); ...
           min(GR, 0.5) + min(GB, 0.5); ...
           min(BR, 0.5) + min(BG, 0.5)];
end
```

MATLAB code for computing the color from the hkl input.